Mercury Dynamics within Natural and Experimental Sea Ice

By

Sarah Anne Beattie

A Thesis submitted to the Faculty of Graduate Studies of
The University of Manitoba

In partial fulfilment of the requirements of the degree of

MASTER OF SCIENCE

Department of Environment and Geography
University of Manitoba

Abstract

Mercury (Hg) is one of the primary contaminants of concern in the Arctic marine ecosystem. The biogeochemical cycling of Hg through the environment is governed by the changing physical and chemical characteristics of various environmental media. Arguably the medium under the most change in the Arctic system is the icescape, which is shifting from a multiyear to a first-year sea ice regime. This work presents the first comprehensive study of Hg dynamics within Arctic multiyear sea ice, followed by a mesocosm-scale mechanistic study of Hg behaviour in new and growing experimental sea ice. Multiyear sea ice taken from the eastern Beaufort Sea and McClure Strait showed total Hg concentrations ranging from 0.12 to 12.2 ng L^{-1}, with the highest concentration in the surface layer. Both the vertical distribution patterns and regional differences can be explained by the sources and dynamics of particulate matter in sea ice. For the first time, methylated mercury was measured in Arctic sea ice: ratios of methylated to total Hg reached as high as 0.4 within bottom ice, suggesting the potential occurrence of in situ methylation in multiyear sea ice. The dominant role of particulate dynamics in controlling Hg distribution in sea ice was further supported by a mesocosm-scale study at the Sea-ice Environmental Research Facility (SERF). Particulate dynamics were found to control both Hg uptake into sea ice upon ice initial formation and the vertical distribution of Hg within the ice column during growth. The deviation of Hg concentrations between SERF and natural frost flowers suggested that both particle incorporation processes and atmospheric scavenging of reactive gaseous Hg affect Hg concentrations in these ice crystals. This work suggests that melting multiyear sea ice represents a considerable loading of total and methylated Hg into the Arctic Ocean system, while the increasing

volume of first-year sea ice will affect the seasonal source of Hg, specifically in the particulate-bound form, into the Arctic Ocean.

Acknowledgements

First and foremost, I would like to extend my sincere gratitude to my supervisor, Dr. Feiyue Wang, for his guidance, encouragement, expertise, patience and most importantly his passion for environmental chemistry. I am extremely grateful I had the opportunity to conduct this unique and exciting research with Dr. Wang. I would also like to thank all of my committee members, Drs. CJ Mundy, Gary Stern and Norm Halden, for their guidance on this work. I truly believe I have been supported by everyone from CEOS (Centre for Earth Observation Science) at one point or another, whether it was dealing with administrative needs to learning how to use a new instrument, and I am very thankful to have such dedicated support system at this institute.

A special, hearty thank you to Debbie Armstrong, who from Day 1 has provided me with exceptional training, support and above all else friendship. The lessons I have learnt from you Debbie extend far beyond chemistry, and I am indebted to you for that. Thank you to my colleagues in environmental chemistry, including Amanda Chaulk, Alexis Burt, Alex Hare, Marcos Lemes, Odile Crabeck, Kang Wang, Dan Zhu, Wen Xu and Ashley Elliot for providing assistance and smiles. The fieldwork completed during this project would not have been possible without the help of Dustin Isleifson, Kerri Warner, Meredith Pind, Megan Shields, Heather Stark and Jean Sebastien Cote. A special thanks to the captains and crew of the CCGS Amundsen for providing logistical support during fieldwork.

Last but not least, I would like to thank Darrell Epp. You are someone I look up to (literally) and I can't wait to go on many a fine adventure with you.

This research was graciously funded by ArcticNet, the University of Manitoba, Canada Foundation for Innovation and the Northern Scientific Training Program (Indian and Northern Affairs, Canada).

Dedications

I would like to dedicate this work to my parents, David and Kathy Beattie. You both have taught me the importance of dedication, hard work, community and honesty. You have instilled in me a curiosity for the world around me (stemming from those countless camping adventures) and have given me all the opportunities in the world. Thank you and I love you dearly.

"And above all else, watch with glittering eyes the whole world around you, as the greatest secrets are always hidden in the most unlikely places. Those who don't believe in magic, will never find it." – Roald Dahl

Table of Contents

List of Tables

List of Figures

List of Acronyms

AMDE = Atmospheric Mercury Depletion Event
CRREL = Cold Regions Research and Engineering Laboratory
CVAFS = Cold Vapour Atomic Fluorescence Spectroscopy
DOC = Dissolved Organic Carbon
DGM = Dissolved Gaseous Mercury
FY = First-Year
GEM = Gaseous Elemental Mercury
GRAHM = Global/Regional Atmospheric Heavy Metal model
GC-CVAFS = Gas Chromatography Cold Vapour Atomic Fluorescence Spectroscopy
MDL = Method Detection Limit
MY = Multiyear
PILMS = Portable In-Situ Laboratory for Mercury Speciation

FeRB = Iron-Reducing Bacteria
RGM = Reactive Gaseous Mercury
SD = Standard Deviation
SRB = Sulfate-Reducing Bacteria
SERF = Sea-ice Environmental Research Facility
UNEP = United Nations Environmental Programme
WHO = World Health Organization

List of Mercury Species

Hg = Mercury
Hg^0 = Elemental Mercury
Hg^{2+} = Divalent Mercury Cation
Hg_T = Total Mercury
Hg_D = Dissolved Mercury
Hg_P = Particulate Mercury
Hg_R = Reactive Mercury
$MeHg_T$ = Total Methylmercury
MMHg = Monomethylmercury
DMHg = Dimethylmercury
$HgCl_2$ = Mercuric Chloride
BioHg = Bioavailable mercury
CH_3HgCl = Methylmercury chloride

Chapter 1: Introduction to Mercury Cycling Within the Arctic Ocean System

1.1 Mercury

Found under Group 12 (IIb) of the Periodic Table, mercury (Hg; atomic number 80, atomic mass 200.59 g mol^{-1}) has a variety of unusual physicochemical properties for a transition metal, most notably its liquid state at standard temperature and pressure (Saha and McKinlay, 1973). The average Hg content of the Earth's continental crust has been estimated to be ~ 40 μg/kg (Hans Wedepohl, 1995), and Hg commonly occurs as red, hexagonal crystals of the mineral ore cinnabar (HgS). This mercuric sulphide ore has considerable commercial value, and its shallow deposits have been mined for millennia (Saha and McKinlay, 1973). Through outgassing and various weathering processes, Hg is released into the surface environment; Alongside evasion from surface soils, waterbodies (fresh and saltwater), vegetation, volcanoes, and geothermal sources all represent major natural Hg emission sources.

Although naturally occurring, additional concentration and redistribution of Hg by anthropogenic emission sources has severely increased the bioavailability of most Hg species. The Industrial Revolution (circa 1850) created a spike in anthropogenic mercury emissions, which mainly originated from chlor-alkali plants until regulatory control measures were implemented in the 1970s. Currently, coal combustion, waste incineration, smelting, refining and manufacturing are the major global anthropogenic Hg sources and account for 30% of annual Hg emissions, while re-emitted Hg from sinks such as the ocean accounts for 60% (Hylander and Meili, 2003; Pirrone et al., 2010; UNEP, 2013a). Common items containing Hg, including lamps, thermostats, batteries and dental

amalgam fillings, are still being produced in both developing and developed countries (Caravati et al., 2008; US Environmental Protection Agency, 2012; Zhang and Wong, 2007), though much of these are being phased out as part of the recently signed Minamata Convention on Mercury.

In the natural environment, Hg exists mainly in two oxidation states; elemental (Hg^0) and divalent (Hg (II)), as the third oxidation state, Hg (I), is not very stable under most environmentally relevant conditions, and undergoes complicated speciation (Liu et al., 2012; Ullrich et al., 2001). Mainly Hg is released from natural sources as Hg^0 vapour (the most volatile form of Hg); however, some sources may also emit Hg bound to particulate matter or aerosols (Schroeder and Munthe, 1998). Due to its high vapour pressure of 0.180 Pa at 20˚C, Hg^0 is mainly found within the troposphere in the gaseous phase and relatively inert to chemical reactions, thus it has a calculated residence time of 0.5-1.7 years (Holmes et al., 2006). As a result of its atmospheric stability, Hg^0 can travel thousands of kilometers from its source through long-range atmospheric transport mechanisms, and deposit in appreciable quantities in remote ecosystems such as the Arctic (Jackson, 1997). Inorganic Hg (II) species are dominant in water, soil and sediments due to their high aqueous solubility (e.g., $HgCl_2$; 66 g/L at 20°C), and sorption characteristics whereas organic Hg (II) species with high log octanol-water partition coefficients (e.g., CH_3HgCl; 1.7 at Cl^- concentrations above 0.08 M) will preferentially partition into and bioaccumulate in biota (Major et al., 1991; Schroeder and Munthe, 1998; Ullrich et al., 2001). Of the organic species, methylmercury (MeHg; representing both monomethyl- (MMHg) and dimethylmercury (DMHg)) is the most prevalent in biota, and unfortunately the most toxic owing to its ability to pass the blood - brain and

placental barriers (Clarkson and Magos, 2006). In anoxic sediment environments, dissimilatory sulfate-reducing bacteria (SRB) from the subclass Deltaproteobacteria have been found to methylate inorganic Hg (Compeau and Bartha, 1985; Widdel et al., 1992). Recent research suggests that some dissimilatory iron-reducing bacteria (FeRB), again belonging to Deltaproteobacteria, can also methylate Hg in sediments (Fleming et al., 2006; Kerin et al., 2006). Although organic matter, such as dissolved organic carbon (DOC), can stimulate microbial activity and thus enhance $MeHg_T$ production, DOC degradation has been found to reduce Hg bioavailability through the formation of thiol-containing molecules that complex with Hg (Barkay et al., 1997; Lin et al., 2012; St. Louis et al., 1994). The role of DOC in microbial methylation is heavily dependent on its composition and structure, and remains an active area of research (Lin et al., 2012). Mercury is also found adsorbed or chemically bound to both organic and inorganic particulate matter (Hg_P) in atmospheric and aquatic media; however its exact chemical and physical structure remains unknown (Keeler et al., 1995; Munthe et al., 2001). These heterogeneous particulates may act as sites of catalyzed Hg reactions, yet the surface chemistry of these reactions remains unclear (Subir et al., 2012).

Mercury is acknowledged as a global pollutant due to its persistence, toxicity, bioaccumulative nature and ability to undergo long-range atmospheric transport mechanisms (Liu et al., 2012). Recent legislations, such as the "Minamata Convention on Mercury", have established a global legally binding treaty that enforces controls and reductions across a range of products, processes and industries in which Hg is used, released or emitted (UNEP, 2013b). In the midst of this concerted international action,

Hg contamination (particularly from re-emission sources) still poses a serious threat to ecological and human health within fragile environmental systems.

1.2 Mercury in the Arctic System

Due to its geographic isolation and small human population, the Arctic system was previously assumed to be unaffected by distant industrial developments and human activity. Concern began to arise when high Hg levels (largely exceeding the Canadian Federal Guidelines for consumable fish; 0.5 μg g^{-1} wet weight) were reported in the liver of ringed seals and other Arctic marine mammals throughout the 1980s and 1990s (Lockhart et al., 2005; Muir et al., 1992; Wagemann et al., 1995; Wagemann and Muir, 1984). A recent study found levels of Hg in the brain tissue of fish-eating mammals such as the beluga whale are higher than the Hg-associated neurochemical effect threshold range of 3-5 μg g^{-1} dry weight, which is based on previous toxicological studies on fish-eating mammals (Basu et al., 2007; Dietz et al., 2013; Lemes et al., 2011; Ostertag et al., 2009). This information has exposed several vulnerabilities of the Arctic system to contaminants: 1) The highly lipophilic nature of Arctic biota allows for MeHg to bioaccumulate in top predators (e.g. Whales, seals, polar bears); and 2) These top predators constitute the bulk of traditional country food diets for the Inuit populations of the North (Barrie et al., 1992). Hg intake has been found to be strongly significantly correlated with the percentage of local food in the diet for both Canadian and Greenlandic Inuit populations (Deutch et al., 2006; Tian et al., 2011). A recent study reported that nearly 25% of Nunavut children tested had hair Hg concentrations equal to or exceeding the World Health Organization (WHO) minimum reference value of 2 μg g^{-1} (Tian et al.,

2011). This raises major concerns over ecological and human health in the Arctic system, and heightens the urgency in understanding the cycling of Hg within this system.

The Arctic Ocean is commonly referred to as a semi-enclosed sea due to encircling landmasses. This setting restricts seawater exchange with both the Pacific and Atlantic Oceans, allowing for the development of thorough regional mass balance budgets (Douglas, 2011). Outridge *et al.* (2008) presented the first mass balance study of Hg in the Arctic Ocean, which incorporated the best available data at the time for the inputs, outputs and total masses in the biotic and abiotic compartments. The largest single source of Hg to the Arctic Ocean system was estimated to be net atmospheric deposition (calculated using a modified version of the Global/Regional Atmospheric Heavy Metal model; GRAHM) at 48% of the total Hg input (Dastoor and Larocque, 2004; Outridge et al., 2008). Inflows from the Pacific and Atlantic Oceans combined and coastal erosion were found to be the other major sources, each contributing 23%, while river contributions were found to be negligible (Outridge et al., 2008). Once in the Arctic marine system, Hg will undergo transport and transformation within different abiotic and biotic environmental compartments (Figure 1.1), as summarized in the sections below.

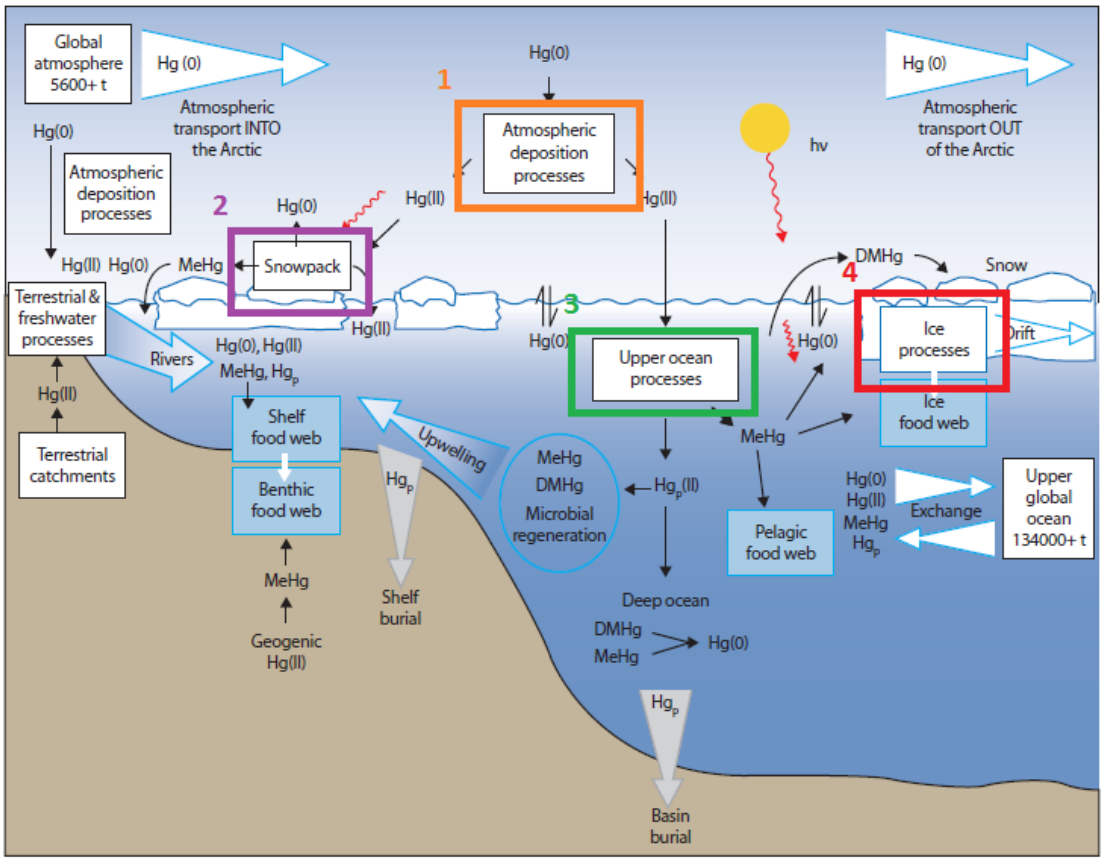

Figure 1.1: Schematic of the processes involved in mercury cycling within the Arctic marine system (Adapted from Douglas et al., 2011).

1.2.1 Atmospheric Deposition Processes

As previously stated, Hg^0 is the dominant form of Hg in the troposphere (represents 98% of tropospheric Hg) and is commonly referred to as Gaseous Elemental Mercury (GEM) (Outridge et al., 2008). Another volatile compound, DMHg, is present in much lower concentrations in the Arctic atmosphere (2-3 pg m^{-3}) and is thought to be evaded from the ocean (Pongratz and Heumann, 1999). The less volatile MMHg has been reported in low concentrations in the Northern European atmosphere (2 pg m^{-3} in Aspvreten, Sweden) and is produced via the degradation of DMHg by OH^- and Cl^-, yet has not been reported in the Arctic atmosphere to date (Munthe et al., 2003; Sommar et al., 2001). The deposition of atmospheric Hg onto the Arctic surface environment is

greatly enhanced when GEM is oxidized to Hg^{2+}. The chemical mechanisms for atmospheric Hg oxidation remained largely unknown until a unique atmospheric phenomenon was discovered in Canada's Arctic. In 1995, continuous monitoring of surface-level GEM and ozone concentrations in the air at Alert, Canada began. During the spring months after polar sunrise (April-June depending on location), major episodic depletions of GEM to below 1 ng m^{-3} (six-hour averaged) were observed and found to be strongly correlated (R = 0.8) to depletions in ozone levels (Schroeder et al., 1998). This phenomenon, which contrasts the behaviour assumed for contaminants with long atmospheric residence times, became known as atmospheric mercury depletion events (AMDEs), and has been found to occur annually across the Arctic, sub-Arctic, and Antarctic coasts (Berg et al., 2003; Ebinghaus et al., 2002; Poissant and Pilote, 2003). Since these events are concurrent with the springtime spike in primary production, the chemical mechanisms driving AMDEs were elucidated over the next decade through intensive international research efforts (Schroeder and Munthe, 1998). In 1998, an anti-correlation was observed between GEM and atmospheric Hg_P concentrations during AMDEs, which led to the hypothesis that GEM was being converted to reactive gaseous mercury (RGM) and Hg_P (Lu et al., 2001). The production of RGM during AMDEs was measured directly in 2000 at Barrow, Alaska, which confirmed the previous hypothesis and prompted continuous monitoring of atmospheric GEM, RGM, and Hg_P concentrations simultaneously as demonstrated in Figure 1.2 (Lindberg et al., 2001; Steffen et al., 2008).

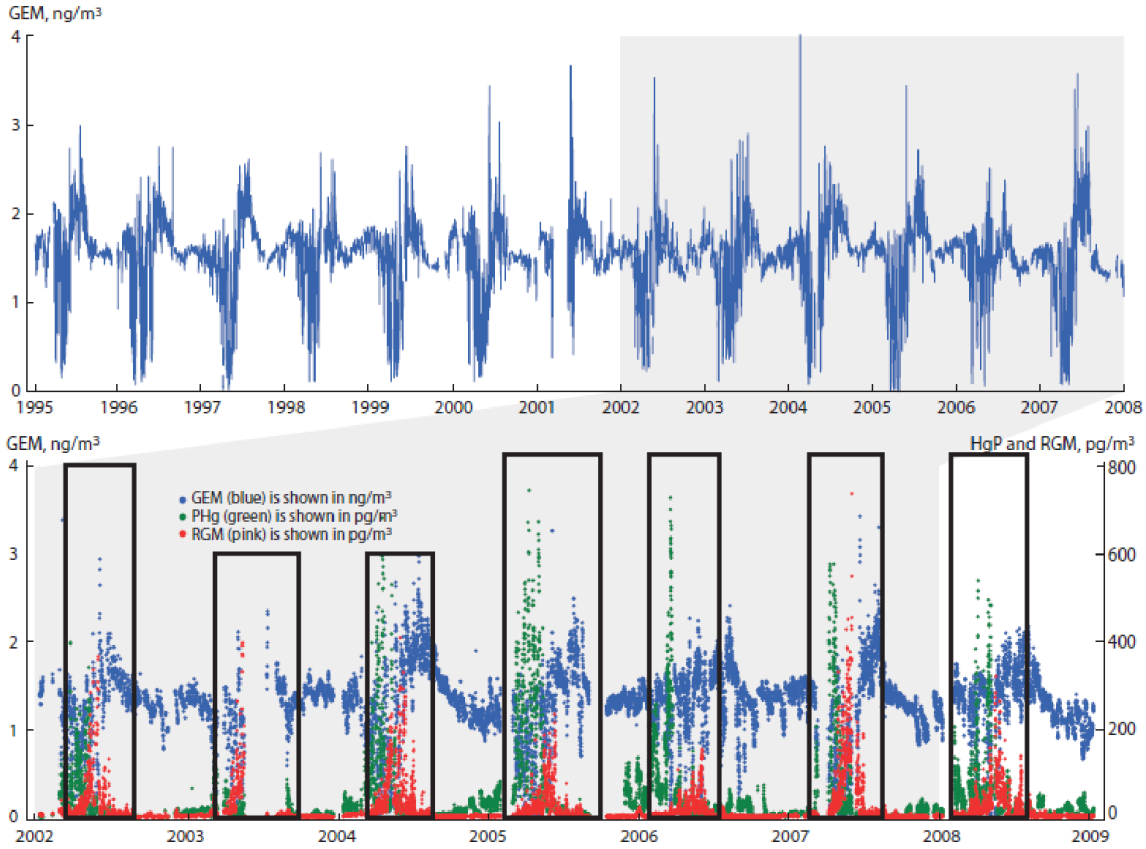

Figure 1.2: Time series of surface level GEM concentrations (six-hour averages) at Alert, Nunavut, Canada from 1995-2008 (top) and time series of GEM, RGM, and Hg_P concentrations (three-hour averages) at Alert from 2002-2008 (bottom), with episodic AMDEs outlined (Adapted from Munthe et al., 2011).

According to general scientific consensus, the depletion of GEM in the troposphere is caused by the oxidation of GEM to RGM by reactive halogens species in the presence of ozone (O_3) (Lindberg et al., 2002). These reactive halogen species were originally thought to be mainly atomic Br or BrO radicals; however, recently high levels of Cl radicals were recorded in the Arctic marine boundary layer, and thus Cl may also act as a strong atmospheric oxidant (Liao et al., 2014). These oxidants originate from areas of open water, such as leads or polynas, where refreezing sea ice and incoming solar radiation release these radicals into the troposphere (Simpson et al., 2007). Leads also initiate shallow convection in the stable Arctic boundary layer, which restocks areas

of depleted Hg^0 through mixing events (Moore et al., 2014). Models and kinetic calculations suggest that RGM is predominately composed of divalent Hg compounds such as $HgCl_2$, HgO and $HgBr_2$, yet its exact chemical identity remains unknown, and thus it is operationally defined as the fraction of atmospheric Hg that can be collected onto a KCl denuder (Ariya et al., 2004; Calvert and Lindberg, 2003; Skov et al., 2004; Swartzendruber et al., 2006). The schematic shown in Figure 1.3 introduces the general autocatalytic reaction pathway (boxed off) for the oxidation of GEM to RGM in the Arctic.

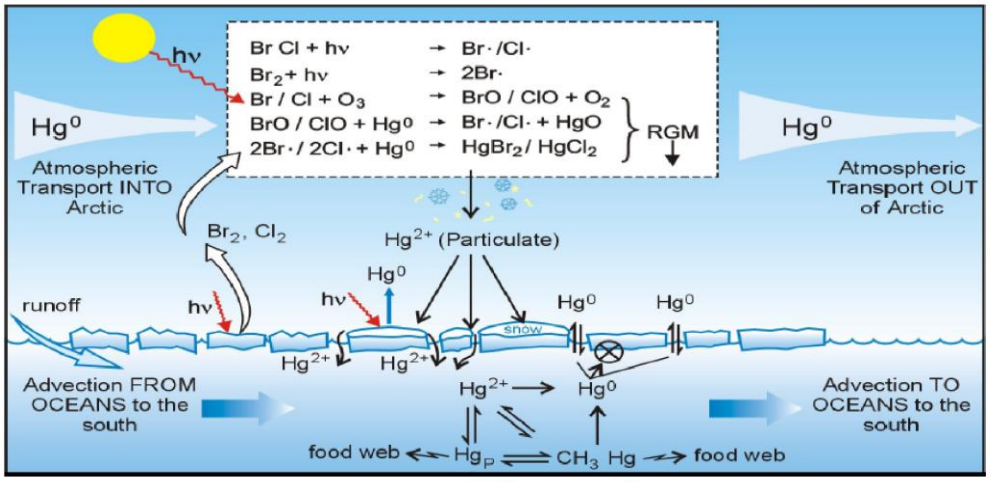

Figure 1.3: Schematic of Hg cycling in the Arctic Ocean System highlighting the general reaction pathway for the oxidation of GEM to RGM. Reprinted with permission from Steffan et al. (2008). Interactive Open Access Journal of the European Geosciences Union.

Once formed, RGM can adsorb onto aerosols and particulate matter, becoming Hg_P (Amos et al., 2012). The predominance of either RGM or Hg_P is dependent on the age of the air mass, local versus transported atmospheric events, and/or the presence of solar radiation (Lindberg et al., 2002; Steffen et al., 2008). Both RGM and Hg_P species will readily deposit out of the atmosphere and transfer to Arctic surfaces (snow, ice, Arctic Ocean surface) via wet or dry deposition processes during AMDEs, which

represent > 90% of total annual Hg deposition with estimated deposition fluxes ranging from 200-2160 ng m^{-2} (Dommergue et al., 2009; Lu et al., 2001; Outridge et al., 2008). Another surprising feature of Arctic atmospheric Hg dynamics is the summer peak in GEM concentrations (Steffen et al., 2005), which has been estimated to be due to significant seasonal circumpolar riverine inputs into the Arctic Ocean system, yet this requires further validation. Since the rate of global anthropogenic Hg emissions has declined, it is assumed that less Hg is being deposited onto Arctic surfaces, yet multi-decadal trends show that Hg concentrations in biota, particularly in the western Arctic, are still rising and thus attention is now being drawn to post-depositional processes (Dietz et al., 2013; Macdonald and Loseto, 2010; UNEP, 2013a; Wang et al., 2010b). Current knowledge on Hg cycling within the Arctic snowpack, ocean water and sea ice will be discussed below.

1.2.2 Snowpack Processes

Mercury has been detected in the surface snowpack (top 5 cm) across all of the Arctic at concentrations ranging from less than one to several hundred ng L^{-1} (Berg et al., 2003; Chaulk, 2011; Dommergue et al., 2009; Lahoutifard et al., 2005; Lindberg et al., 2002; Lu et al., 2001). Nearly 99% of the Hg in the snow is present as either inorganic Hg^{2+} (~94-97%) or $MeHg_T$ (~5%) while only 1% is located in the interstitial air of the snowpack as Hg^0 (Ferrari et al., 2004). Surface snow concentrations can increase dramatically during AMDEs and, during one reported case near Barrow, Alaska, concentrations rose from background levels of 4.1-15.5 ng L^{-1} to elevated levels of 147-237 ng L^{-1} (Johnson et al., 2008; Lindberg et al., 2002). These increases vary spatially and temporally, as surface snow concentrations up to 820 ng L^{-1} have been reported along

sea ice leads, supporting the hypothesis that halogens from sea ice play a fundamental role in AMDEs (Douglas et al., 2005; Lu et al., 2001). Also, not all AMDEs will lead to increases in Hg surface snowpack concentrations, which could be due to the quick transformation or transfer of deposited Hg (Chaulk, 2011; Ferrari et al., 2005). Numerous field studies have noted that surface snow Hg concentrations decrease by over 50% within the first 24 hours after deposition events (Lahoutifard et al., 2005; Lalonde et al., 2002; Poulain et al., 2004). Further lab incubation studies indicated this decrease could result from photoreduction of Hg^{2+} to volatile Hg^0, which then is re-emitted back into the atmosphere (Lalonde et al., 2002; Poulain et al., 2004). This is further supported by a large negative mass-independent fractionation of mercury isotopes in the Arctic snowpack (Sherman et al., 2010). The photoinduced oxidation of Hg^0 to Hg^{2+} during AMDEs and subsequent re-emission of Hg^0 following photoreduction from snowpack surfaces in the summer has led to the classification of the Arctic as being a sink of atmospheric Hg^0 in the springtime and source in the summer (Hirdman et al., 2009). The fraction of Hg stored in the snow can percolate into the underlying sea ice (Chaulk et al., 2011) or be released in meltwaters during the spring. Field studies that incorporated flux chamber measurements of volatilization and snowmelt calculated a combined release of 10-35 ng m^{-2} day^{-1} of Hg^0 into the Arctic system (Dommergue et al., 2003). A study investigating ice crystals (grown kinetically from the vapour phase onto surfaces), including surface hoar, diamond dust, and frost flowers, found that their Hg concentrations are typically 2-10 times higher (41-1370 ng L^{-1}) than reported for snow during AMDEs (~80 ng L^{-1}) (Douglas et al., 2008).

Concentrations of $MeHg_T$ in the Arctic snowpack range from 0.010-0.280 ng L^{-1}, and the source has been hypothesized to be either deposition of MMHg after atmospheric oxidation of DMHg to MMHg, aqueous phase methylation in wet deposition, or abiotic methylation via a substrate involved in the dimethylsulfoniopropionate (DMSP) cycle (Gårdfeldt et al., 2003; Hammerschmidt et al., 2007; Lahoutifard et al., 2005; Larose et al., 2010; St Louis et al., 2007; St. Louis et al., 2005).

1.2.3 Ocean Processes

Once deposited directly into the Arctic Ocean, Hg^{2+} can be transformed, complexed with available DOC, or exported out of the system. Concentrations of Hg_T and $MeHg_T$ in the Arctic marine water column range from 0.04-0.58 ng L^{-1} and 8.62-127 pg L^{-1} respectively, and demonstrate contrasting vertical profiles (Kirk et al., 2008; St Louis et al., 2007; Wang et al., 2012). In open water conditions, Hg_T is enhanced in the surface water layer, yet is less enhanced or absent in ice-covered conditions, signifying that sea ice attenuates atmospheric deposition into the seawater (Kirk et al., 2008; Wang et al., 2012). Similar to the Southern Ocean (Cossa et al., 2011), a subsurface MeHg peak occurs in the Arctic Ocean at the same depth as the nutrient maxima and dissolved oxygen minima (Wang et al., 2012), suggesting the occurrence of mercury methylation in the water column. Laboratory incubation experiments performed on Arctic seawater demonstrated that MMHg formed from isotopically-labelled inorganic Hg, thus water column methylation may occur in polar waters (Lehnherr et al., 2011). Elevated concentrations of DGM (dissolved gaseous mercury) and GEM have been reported in ice-covered surface waters and the atmospheric marine boundary layer above open water, suggesting either photo- or microbial reduction of Hg^{2+} to Hg^0 occurs in surface seawater

and that the sea ice cover impedes the evasion of Hg^0 to the atmosphere (Andersson et al., 2008; Douglas, 2011; Sommar et al., 2010). A large portion of Hg^{2+} will readily complex with Cl^- or DOC in the upper ocean, and can be exported to the deep ocean via vertical flux of the polar mixed layer or to the Atlantic Ocean with bulk water mass movements (Douglas, 2011; Hammerschmidt et al., 2007).

1.3 Sea Ice

1.3.1 Arctic Sea Ice Trends

Although the occurrence, severity, and effects of climate change continue to be debated on regional and global scales, the substantial decline in the thickness and summer aerial coverage of Arctic sea ice over the past 40 years has been undisputedly documented by the scientific community. Advances in remote sensing techniques have allowed for continuous monitoring of sea ice extent and, beginning as early as 1953, declines in the summer Arctic sea ice extent and seasonal durations have been reported (Parkinson and Cavalieri, 2008; Stroeve et al., 2007). Any sea ice mass that survives over an entire melt season will be defined throughout this work as multiyear (MY) or perennial sea ice, whereas sea ice that succumbs fully to the melt season and lasts for less than a year is defined as first-year (FY) or seasonal ice. Multiyear sea ice is able to survive the summer melt due to the relatively less dynamic and strongly stratified Arctic Ocean, where reduced convection results in less physical loss of sea ice over the melt period (Comiso, 2002). In order for this type of coverage to remain consistent from year to year, a certain amount of FY ice must survive through the intervening melt season to replenish the MY ice lost annually due to melt and export. Record minima in Arctic sea

ice extent, which occurred in September of 2002, 2004, 2007 and most recently in 2012, likely result from persistent low pressures and high temperatures over the Arctic Ocean in the summer (NSIDC;, 2012; Serreze et al., 2003; Stroeve et al., 2008; Stroeve et al., 2005). These conditions impede FY ice from surviving through the melt season, effectively lowering the amount of FY ice that evolves into MY ice. From 2005-2008, a 42% decline in MY ice coverage across the Arctic Ocean was observed, and a drastic average thinning of ~0.6 m occurred across MY ice floes. Specifically in the Beaufort Sea, where MY ice floes become incorporated into the anticyclonic gyre causing areal ice coverage to be highly variable from year to year, an increase in negative ice concentration anomalies from 1979-2000 was observed (Barber and Hanesiak, 2004b). Presently, FY ice has surpassed MY ice in winter coverage and volume across the Arctic, and has become the dominant ice type (Kwok et al., 2009). The Arctic icescape has thus shifted from a MY to a FY ice regime, and undergone associated physical and biogeochemical changes due to the contrasting properties of these two ice types. These properties will be highlighted below with a brief introduction of sea ice formation, growth, and melt evolution processes.

1.3.2 Sea Ice Formation

Once atmospheric temperatures drop to below the freezing point of seawater (which is depressed relative to freshwater due to the high salinity) at the onset of winter, particulate matter present within cooled surface waters act as sites of nucleation, allowing for solid crystals to form within the liquid seawater phase (Tucker III et al., 1992). These solid individual crystals skim the ocean surface, taking on the shape of small discs less than 2-3 mm wide. Each disc begins as a tetrahedral arrangement of water molecules

with the crystallographic axis (c-axis) normal to the basal plane. Lateral growth of each disc follows until the shape becomes unstable, causing the crystals to then take on a hexagonal, stellar form with dendritic arms stretching out across the surface. The unique lattice structure defined as ice Ih forms for each individual crystal, as demonstrated by the schematic in Figure 1.4.

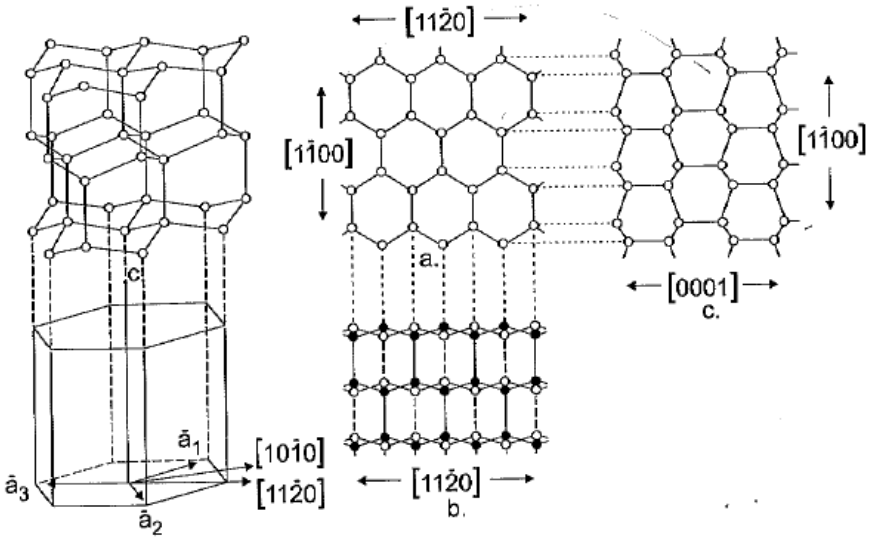

Figure 1.4: Crystal structure of ice Ih. The c-axis is indicated at the left and right of the 2D projections, which display the view along (top) and normal (bottom) to the c-axis. Reprinted with permission from (Weeks and Ackley, 1986). Copyright (2010) Blackwell Publishing Ltd.

1.3.3 Sea Ice Growth

Once a continuous surface sheet of ice composed of ice platelets with random c-axis orientations (termed frazil ice) has formed, subsequent thermodynamic growth downwards at the ice-seawater interface occurs due to the freezing of water molecules onto the advancing ice surface (Petrich and Eicken, 2010; Pfirman et al., 1990). A process entitled geometric selection favours crystal growth oriented in the advancing growth direction, causing the formation of a transition layer that is more organized than the surface layer. Long, vertical, columnar crystals with horizontal c-axes form yet a third

layer within the ice which encompasses the bulk of the ice morphology depth profile (Tucker III et al., 1992). At the bottom of the advancing ice sheet, a nonplanar surface composed of thin lamellar bulges forms and constitutes the bottom skeletal layer of the ice sheet. General FY sea ice stratigraphy, along with textural and genetic classifications, is demonstrated in Figure 1.5.

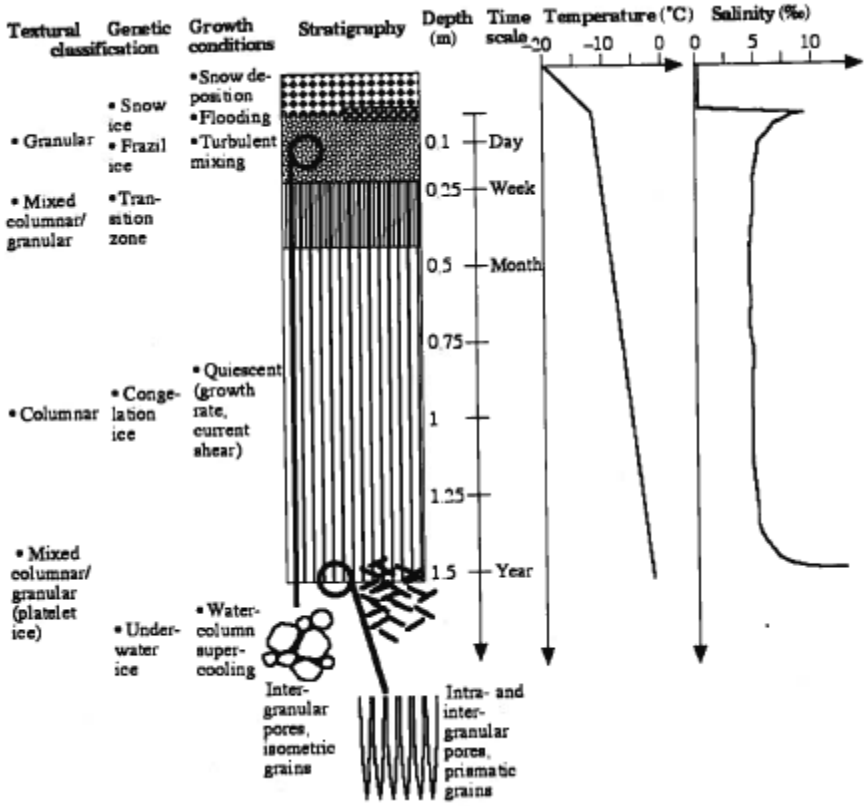

Figure 1.5: Schematic summarizing the textural and genetic classifications of sea ice stratigraphy, the growth conditions and timescale, and generalized salinity and temperature profiles for FYI. Reprinted with permission from (Petrich and Eicken, 2010). Copyright (2010) Blackwell Publishing Ltd.

Overall ice types and pack features largely result from the state of the ocean surface upon initial ice formation. These ice types are listed in Table 1.1 alongside their growth conditions and thicknesses.

Table 1.1: Sea Ice types with associated formation conditions and physical characteristics (Petrich and Eicken, 2010)

Sea Ice Type	Formation and Growth Conditions	Average Thickness* (cm)	Physical Characteristics
Grease Ice	Agitated	0-2	Aggregation of frazil ice into thin surface layer
Pancake Ice	Agitated	0-10	Consolidation of frazil ice into larger units
Frost Flowers	Cold, Calm	0.1-0.3 for single flower	Delicate ice crystals that form on new thin ice, highly saline
Nilas Ice	Calm	0-10	Dark Nilas: <5 cm (thin enough to see underlying ocean) Light Nilas: >5cm
Young Ice	Calm	10-30	Grey Young: 10-15 cm Grey-white Young: 15-30 cm
First-year Ice (FY ice)	Calm	30-200	Surface can be level and covered in snow (white), melt ponds during melt period
Multiyear Ice (MY ice)	Calm	200-1000	Surface covered in hummocks and pressure ridges, melt ponds during melt period

*Thickness is dependent on the conditions affecting thermal growth and mechanical consolidation, and thus varies widely within some ice types, such as MY ice (Petrich and Eicken, 2010).

1.3.4 Brine Inclusions

Most major ions present in seawater are unable to be incorporated into the ice Ih crystal lattice structure due to physical and electrical constraints (Petrich and Eicken, 2010). As ice grows and the ice-seawater interface continues to extend downwards into the water column, a small fraction of these salts are retained in liquid inclusions within the solid ice matrix, forming brine pockets/layers, while the bulk salt mass is rejected into the underlying waters (Petrich and Eicken, 2010). The local volumes of the brine inclusions (described as brine volume) are mainly determined by the growth rate of the ice, which is temperature dependent. Changes in ice temperature will in turn change the

size of the brine inclusions due to the freezing or melting along the walls of the inclusions (Light et al., 2003; Weeks and Ackley, 1986).

Brine inclusions are removed from the bulk ice sheet in two ways: brine expulsion or gravity drainage. During the initial stages of ice growth, brine expulsion, which is completely independent of initial ice permeability, occurs. Brine expulsion caused by increased pressure on the brine inclusions due to the freezing of their outer edges and a subsequent internal volume decrease (Cox and Weeks, 1974). Most of the brine will be expelled downwards; however, thinner ice allows for brine to be expelled upwards onto the ice surface through microfissures along the crystallographic basal plane (Niedrauer and Martin, 1979). This process is enhanced by capillary effects induced through the formation of frost flowers and by surface snow cover (Drinkwater and Crocker, 1988).

The main form of brine removal is, however, through gravity drainage, which occurs almost immediately after its entrapment. Gravity drainage can occur through two mechanisms. Firstly, since sea ice is less dense than seawater, some ice can be raised above the waterline as ice grows, and the resulting hydrostatic pressure head can force brine down and out of that upper surface ice (Eide and Martin, 1975). Secondly, during ice growth and an increasing temperature gradient between surface ice (cold) and interior/bottom ice (warmer), brine inclusions in surface ice sections have higher salinities (> 24.7) and densities, which cause vertical drainage of the brine phase (Petrich and Eicken, 2010).This form of brine drainage does depend on ice permeability, which again is dependent on the temperature gradient in the ice (Cox and Weeks, 1974). Gas entrapped in the ice upon formation leaves empty cavities, allowing for brine channels to

connect together to form vast networks that drastically increase the porosity within the ice column over time (Eide and Martin, 1975).

Due to brine expulsion upwards to the surface of the ice and gravity drainage towards the bottom, FY bulk ice salinity profiles generally take on a characteristic c-shape, demonstrating increased salinities at the top and bottom surfaces of the ice sheet as shown in Figures 1.5 and 1.6 (below). These c-shaped profiles become less pronounced with increasing ice thickness, yet still exhibit high salinity at the ice surface (Cox and Weeks, 1974). Saline areas contain a large brine volume, small solid ice phase, and a high density (Petrich and Eicken, 2010; Timco and Weeks, 2010; Tucker III et al., 1992).

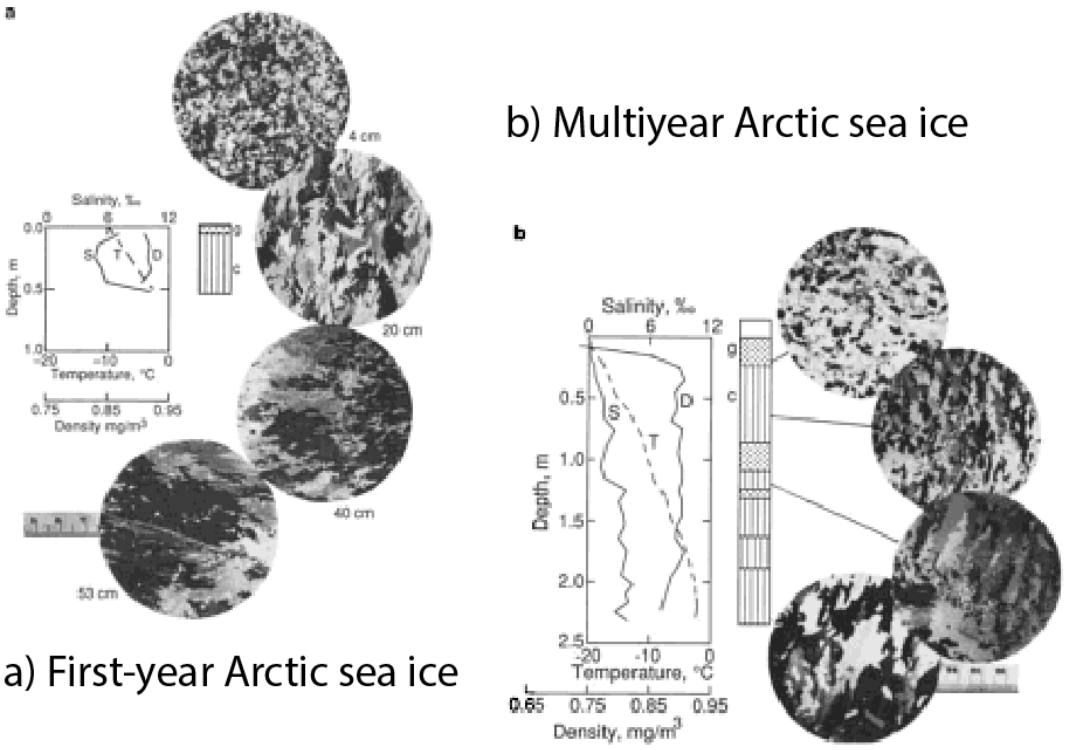

Figure 1.6: Physical properties (salinity (S), temperature (T), and density (D)) and cross sectional crystal structure profiles for (a) Arctic FY ice, 53 days after freeze (after Gow et al., 1990) and (b) Arctic MY ice (Adapted from Tucker et al., 1992).

1.3.5 First Year Ice Growth

The thickness of FY ice is controlled by the ambient air temperature, freezing time (length of cold season), snow type and thickness, wind speed, ocean heat flux, and the surface radiation balance. Level (surface void of ridges, hummocks, melt ponds, or any other topographical features) FY ice in the Beaufort Sea can reach thicknesses of ~200 cm at the end of winter (Melling et al., 2005). During the melt season, ice of all ages will exhibit melt ponds, yet FYI will quickly fall victim to these surface waters and melt completely (Fetterer and Untersteiner, 1998).

1.3.6 Evolution of Multiyear Sea Ice

Since MY ice has survived the melt season, it generally bares signs of physical deterioration and only a small portion of the ice mass remains at the end of the melt season. The evolution of MY ice is driven by two distinct processes: desalination and crystal retexturing (Tucker III et al., 1992). Combined, these two processes produce an ice matrix with physical and chemical properties that resemble freshwater ice more than that of FY sea ice.

Desalination

Desalination primarily occurs due to temperature changes within the sea ice. There is a distinct difference between these brine removal mechanisms and brine expulsion. Rising temperatures cause the bulk ice mass to melt, which can cause two different effects that both contribute to overall desalination. Firstly, the brine inclusions between the ice crystals increase in size as the surrounding ice edges melt into the brine solution. Thus the brine volume increases while local salinity decreases, and brine pockets begin to amalgamate to form interconnected brine channel networks. A miniature positive feedback loop results, as these networks facilitate gravity drainage of brine,

which in turn enhances desalination (Niedrauer and Martin, 1979). Secondly, the increased melting of the pure crystal ice phase and any overlaying snow produces surface meltwaters upon the ice that eventually pool into large melt ponds. This near-freshwater can acts as a hydraulic head if above freeboard level, percolating through the ice, flushing out most of the brine inclusions, and causes strong desalination of the upper ice column (Eicken et al., 2004; Tucker III et al., 1992).

Overall MY ice is less saline than FY ice, and the salinity distribution in MY ice is heavily dependent on topography and thus misinterpreted by single average profiles, as suggested by the wide range of compiled mean salinities of Arctic MY ice floes (1.5-5 for thickness from 200-400 cm (Timco and Weeks, 2010)). A decrease in salinity signifies brine drainage from inclusions, which causes brine channels to form and decreases the solid ice phase in the lower portions of the ice sheet. The flushing of surface meltwaters in the upper portions of the ice column causes crystal retexturing and consolidation in this area, thus decreasing porosity within the upper section of MY ice sheets. The compact nature of MY ice enhances the strength of the bulk ice (Sinha, 1984). Complimentary to these processes, the density of MY ice is found to decrease as it is proportional to salinities and inversely proportional to porosity (Tucker III et al., 1992).

Crystal Retexturing

Due to increased surface flushing of sea ice during the melt season, the crystalline morphology of ice is modified. The pointed, dendritic arms of crystals become rounded and the platelet structure of the ice deforms until its eventual elimination. This process has been found to occur to depths up to ~100 cm in the ice column (Gow et al., 1987). Closer inspection of the modified crystal microstructure using light scanning microscopy

revealed that crystals still appear to have columnar plates, yet lack any variations in outer surface shape and texture, and thus barely resemble their original forms (Gow et al., 1987).

As previously discussed, long columnar crystals with well-defined plated substructure form a noticeable third layer in sea ice stratigraphy upon formation. This substructure is extremely characteristic of FY ice, as this third layer becomes compressed and ill-defined in MY ice. The transition layer also becomes unrecognizable in MY ice, normally due to its physical loss during the melt season (Pfirman et al., 1990; Tucker III et al., 1992). These contrasting microstructure characteristics are shown in Figure 1.6. The FY ice was found to be composed of granular crystals for the upper 5-15 cm of the ice sheet, then transitioned into mostly columnar ice for the remaining depth (Gow et al., 1990). However MY ice demonstrated a larger granular surface layer, followed by columnar ice interrupted by various sections of granular ice throughout its depth corresponding to annual melt periods (Tucker III et al., 1992). In the absence of crystal texture data, $\delta^{18}O$ (ratio of stable isotopes ^{18}O:^{16}O in sample relative to standard), which reveals the origin of water masses within the ice, can act as a proxy for crystal texture and be used to date the ice. Heavily depleted $\delta^{18}O$ values indicate the ice contains water that is meteoric in origin and is normally associated with snowfall, and thus may represent annual layers (Lange and Hubberten, 1992; Tang et al., 2007).

Multiyear sea ice thickness is a function of thermal growth, physical ice decay and mechanical dynamics (Timco and Weeks, 2010). An early version of a one-dimensional thermodynamic growth model of sea ice estimated the equilibrium thickness of un-deformed Arctic MY ice is 300-400 cm (Maykut and Untersteiner, 1971).

Compiled direct-measurement data from 65 relatively level MY ice floes in the Canadian Arctic reported a mean thickness of 560 cm ± 220 cm (Timco and Weeks, 2010). Sea ice dynamics involves the motion of sea ice cover within a system, and is influenced by inertial forces, atmospheric and oceanic traction across the top and bottom ice surfaces, the Coriolis force and the sea surface (Feltham, 2008). Individual floes can converge/collide into one another with considerable force (described as rafting events), causing small block fragments to break off and become lodged between the floe edges to form long piles of rubble above and beneath the ice cover, overall creating a pressure ridge (Haas, 2010). Due to differential melt and decay over time, MY ice is rich in topographical features ranging from hummocks to curved, weathered ridges, and exhibits an undulating surface even on un-deformed floes (Petrich and Eicken, 2010; Tucker III et al., 1992). Thus MYI thickness distribution is a strong function of the growth, decay and convergence history of the individual floe, and is highly variable between floes and even across a single floe.

The contrasting physical characteristics of FY and MY ice are summarized in Table 1.2. These characteristics, specifically salinity, define the dielectric/optical properties of the ice surface and thus the propagation, attenuation and scattering of electromagnetic waves through the ice will give off different signatures for FY and MY ice, allowing for remote sensing to act as identification tools for ice age (Kwok et al., 1992).

Table 1.2: Summary of contrasting physical properties of FY ice and MY ice (Petrich and Eicken, 2010; Tucker III et al., 1992).

Property	First-Year (FY) Sea Ice	Multiyear (MY) Sea Ice
Salinity (Porosity, Density, Brine Volume)	- Profiles generally demonstrate characteristic c-shape - ↑ Brine volume, ↑ Density, ↓ Porosity in upper section of FY ice	- Low salinity in upper 50-100 cm of ice column - ↓ Brine Volume, ↓ Density, ↑ Porosity in upper section of MYI - ↓ Solid ice phase in lower section of MYI due to brine drainage channels
Crystal Texture	- Generally exhibits granular layer in top 30 cm, followed by small transitional layer - Well-defined columnar layer	- Large granular layer in top 50-70 cm, no transitional layer - Poorly-defined columnar layer interspersed with granular layers
Thickness	- If level, can reach a thickness up to ~200 cm at end of winter - If unlevel, can be variable across a floe	- Reaches ~550 cm at end of winter - Extremely variable across even individual floes
Surface Appearance and Topography	- Few topographical features - Generally flat surface - Large melt ponds present during early summer	- Many topographical features including hummocks and ridge - Deformed, undulating surface - Small yet numerous melt ponds present throughout summer
Strength	- Consolidated frazil FYI is stronger than columnar FYI	- Columnar MYI is stronger than all FYI due to compaction over time

1.3.7 Sea Ice Biota

Sea ice represents an important habitat for viruses, psychrophilic archaea and bacteria, autotrophs (algae), heterotrophs (protists) as well as meio- and macrofauna. Each of these organism assemblages require certain conditions to survive, and thus are often found in local microhabitats of the ice matrix. Bacteria and their associated viruses mainly inhabit the brine phase of sea ice and are extremely ubiquitous, having been reported in every ice sample (FY and MY ice included) examined for that purpose (Deming, 2010). However, the abundance of bacteria in lower sections of melting FY ice is nearly 4 orders of magnitude higher than surface winter MY ice due to the cold

temperatures and desalination of MY ice over the melt period (Collins et al., 2008; Krembs and Engel, 2001). Sea ice algal communities require light and access to nutrients, thus they mainly occur in the bottom 10 cm of the skeletal ice layer. The algal spring bloom occurs in late March in low light conditions, and most cells slough off during the summer melt or die off mid-June. Unless MY ice is thick enough to impede light penetration through the ice, it is assumed that algal biomass across the bottom surfaces of both MY and FY ice will be similar during the spring bloom (Deming, 2010). In certain cases, "relics" of algal bottom communities from previous years can be detected within the middle interval of MY ice (Thomas et al., 1995).

1.4 Mercury Cycling In Sea Ice

1.4.1 Mercury Cycling in Arctic Sea Ice

Sea ice was once thought to act as a barrier over the ocean surface, restricting atmospheric-oceanic transport of Hg, and was assumed to be an inactive matrix, thus acting overall as a winter or perennial sink for Hg (Ariya et al., 2004). Once sea ice was found to be permeable to the transport of gases and other chemicals (Golden et al., 2007; Gosink et al., 1976), exploring its role in the cycling of Hg within the Arctic Ocean system became crucial. The first comprehensive study of Hg cycling within Arctic sea ice was conducted by Chaulk et al. (2011) in the southern Beaufort Sea. Many sea ice types were sampled for Hg over the course of this study, and concurrent sampling of atmospheric and oceanic Hg concentrations allowed for transport mechanisms to be estimated. In nilas and young ice, Hg_T concentrations ranged from 0.22-0.53 ng L^{-1}, which was ~2-fold the Hg_T concentration of the underlying seawater (0.11-0.28 ng L^{-1}). Profiles of FY ice allowed for the distribution of Hg_T within the ice column to be

reviewed, and in nearly all FY ice cores studied a surface enrichment in Hg_T was seen (ranged from 0.5-4 ng L^{-1}) followed by a sharp decrease in concentration to ~0.2 ng L^{-1} throughout the remaining ice depth, as shown in Figure 1.7 below (Chaulk et al., 2011).

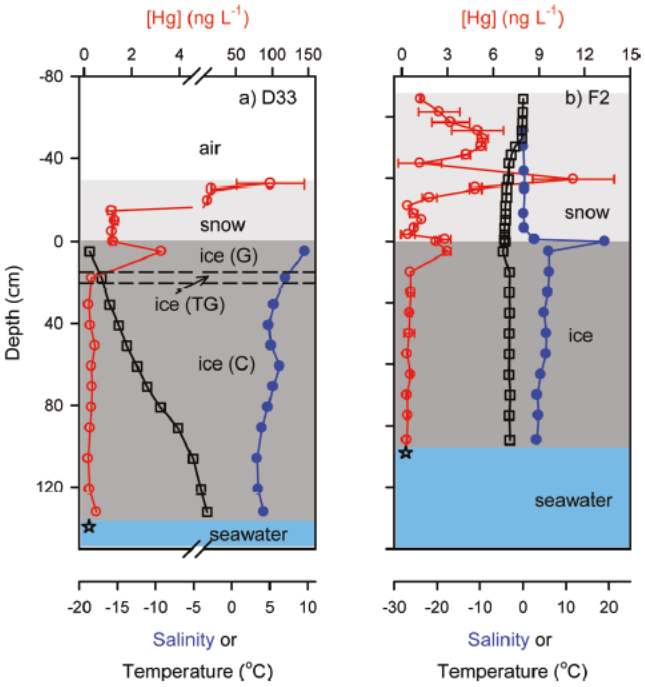

Figure 1.7: Profiles of Hg (○), salinity (●) and temperature (□) in overlying snow, FYI and underlying seawater from (a) a drift ice station (D33, sampled on March 25, 2008) and (b) a landfast ice station (F2, sampled on May 14, 2008). Dashed lines represent the boundaries between various ice crystal textures: Granular (G), transitional granular (TG) and columnar (C). Reprinted with permission from (Chaulk et al., 2011). Copyright (2011) American Chemical Society.

Brine was sampled via the sack-hole method on a 12-hr cycle, and Hg_T concentrations ranged from 2.6 – 71.2 ng L^{-1}, which was much higher than the underlying seawater (Chaulk et al., 2011).

Ancillary variables of the sea ice, including temperature, salinity and crystal texture, were measured for nearly all cores, allowing for the relationships between Hg_T distribution and physical ice characteristics to be examined as well as the origins of Hg in sea ice to be predicted. The Hg_T concentration in brine was found to demonstrate a

strong, statistically significant relationship with brine salinity ($r^2 = 0.80$, $p < 0.001$). However, FY ice Hg_T concentrations (normalized to brine volume) at the sack-hole site only demonstrated a weak logarithmic relationship with salinity ($r^2 = 0.39$, $p < 0.001$). Freeze rejection, the process by which major salt ions are expelled from the bulk sea ice matrix and accumulate in brine pockets, was deemed to be only partially responsible for Hg_T concentrations within sea ice.

Since surface enrichment was seen for all cores regardless of season or ice type, it was suggested that this ubiquitous phenomenon may be related to the formation and growth of sea ice. In particular, surface enrichment was consistently found to occur within the granular layer, which forms through the consolidation of frazil ice. This ice layer is rich in particulate matter, both atmospheric and aquatic in origin, as well as brine pockets and therefore, the high Hg_T concentrations in this layer was suggested to be a function of both of these features (Chaulk et al., 2011). Since newly-forming, nilas ice sampled during active AMDEs had Hg_T levels on the same order of magnitude as the underlying seawater, it was suggested that the surface of new ice is not an effective scavenger of Hg^0 or Hg^{2+} from the troposphere (Chaulk et al., 2011; Douglas et al., 2005).

By sampling overlying snow cover at several sites, the authors were able to comment on the leaching of Hg from snow cover to the sea ice surface. At one station, Hg_T concentrations within the basal snow layer agreed very well with the underlying enriched surface sea ice concentration (see Figure 1.7b), yet this was not witnessed at the other station sampled (Figure 1.7a). These cores were taken during different seasons, which suggested that snow melt increases ice surface Hg_T concentrations and thus

highlighted the strong seasonal influence on Hg distribution in sea ice (Chaulk et al., 2011).

A single 380-cm MYI core was also reported by Chaulk et al. (2011) (see Figure 1.8 below), and Hg_T concentrations were again found to be elevated at the surface (> 4 ng L^{-1}) then decreased to levels similar to the underlying seawater. A unique feature was noted in the core, whereby Hg_T concentrations peaked to ~1.5 ng L^{-1} in a cyclical fashion. These peaks may correspond to periods of melt and refreezing characterized by granular ice layers, and thus represent perennial variations, yet this has not been confirmed due to a lack of data. Thus, further measurement of Hg concentrations within multiyear sea ice is warranted.

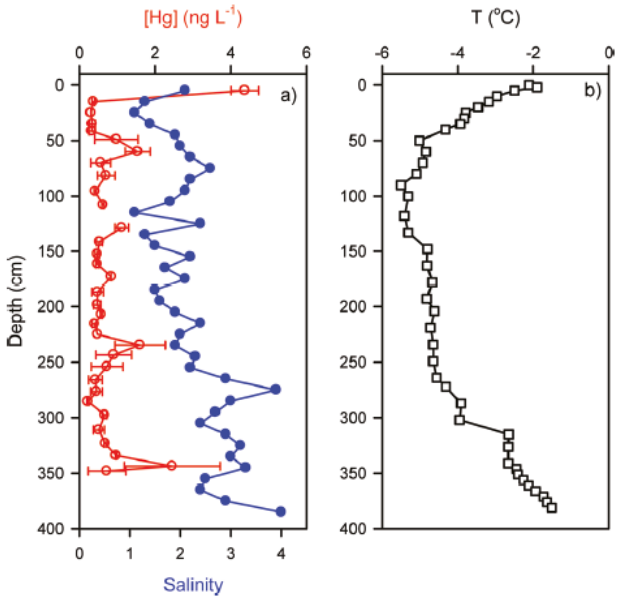

Figure 1.8: Profiles of (a) Hg (○), salinity (●) and (b) temperature (□) in snow-covered MYI (MY1, sampled on May 25, 2010). The overlaying snowpack was not analyzed for Hg. Reprinted with permission from (Chaulk et al., 2011). Copyright (2014) American Chemical Society.

1.4.2 Mercury Cycling in Antarctic Sea Ice

An extensive investigation of Hg in the Southern Ocean was conducted by Cossa et al. (2011) from 2008-2009, and a fast FYI study undertaken 12 km northeast of the Casey Station in the Australian East Antarctic sector in November (during ice growth) was included in this work. This work investigated Hg speciation within sea ice by analyzing for Hg_T, Hg_R (easily reducible, labile mercury) and $MeHg_T$ within the overlying snow, sea ice, underlying seawater and brine sack-holes. The profiles of Hg_T, $MeHg_T$, salinity, particulate organic carbon (POC), and Chl *a* within snow, bulk sea ice and seawater are shown in Figure 1.9.

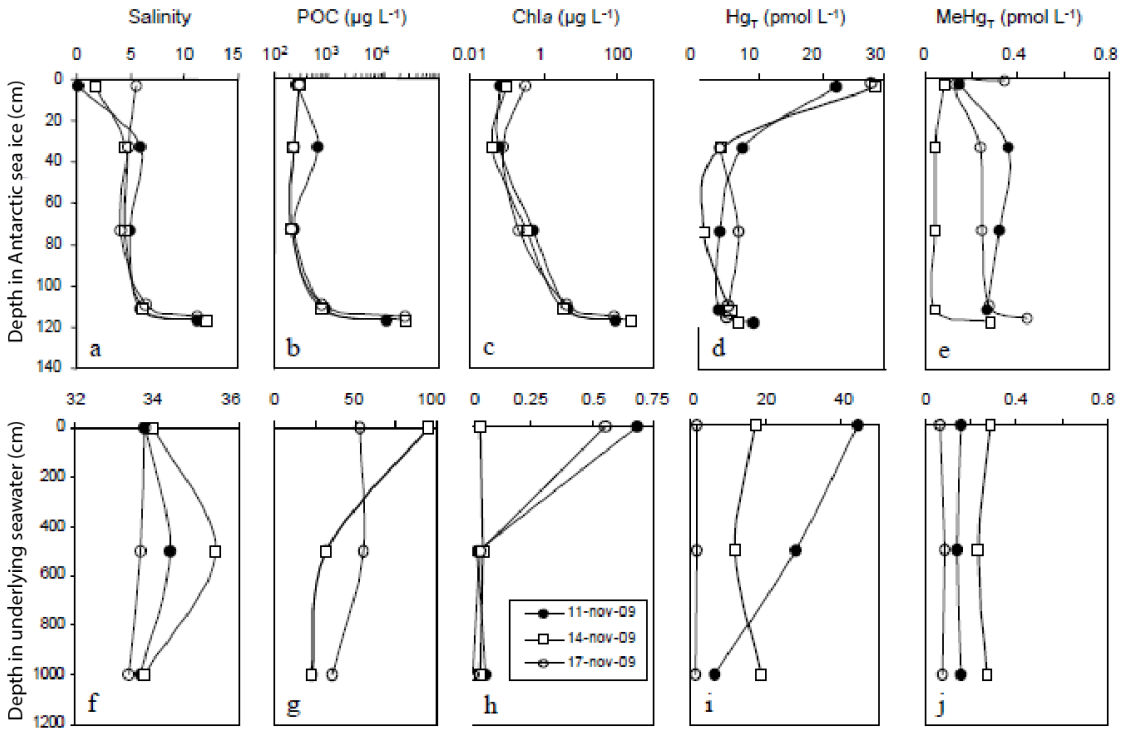

Figure 1.9: Profiles of Hg species and ancillary variables in snow, bulk sea ice and seawater in the coastal sea ice environment 12 km northeast of the Casey station, Antarctic. Profiles (a-e) are from sea ice and profiles (f-j) are from the underlying seawater. Reprinted with permission from (Cossa et al., 2011). Copyright (2011) Elsevier.

Within sea ice (n=14), the concentrations for Hg_T, Hg_R and $MeHg_T$ were found to range from 0.18-4.48 ng L^{-1}, 0.05-3.59 ng L^{-1} and 0.01-0.1 ng L^{-1} respectively. Sack-hole brine (n=4) showed concentrations similar to sea ice for all species with averages at 2.80, 1.83 and 0.02 ng L^{-1} for Hg_T, Hg_R and $MeHg_T$ respectively. The Hg_T and Hg_R levels in sea ice were considerably higher than those of the underlying seawater, whereas $MeHg_T$ levels were similar to open water concentrations (below 0.1 ng L^{-1}). The distributions of both Hg_T and Hg_R within the ice column were generally c-shaped, demonstrating higher concentrations at both the surface and bottom, which further supports the surface enrichment phenomenon described in Chaulk et al.(Chaulk et al., 2011; Cossa et al., 2011). The percentage of Hg_R/Hg_T ranged from 10-100%, and was lowest at the bottom of the ice, where the $MeHg_T/Hg_T$ percentage increased 20-fold to nearly 10%. Thus the $MeHg_T$ concentration peaked at the bottom of the ice where high POC and autotrophic biomass (Chl *a*) was observed. Results from a Principal Component Analysis revealed that Hg_T and Hg_R covaried with salinity, whereas $MeHg_T$ covaried with POC and Chla. Thus, the authors suggested that inorganic Hg distribution within the sea ice environment was governed by brine dynamics, whereas organic Hg distribution was governed by biological processes.

1.4.3 The Effects of a Changing Sea Ice Regime on Hg Cycling within the Arctic Ocean

The changing sea ice regime in the Arctic, characterized by a declining seasonal sea ice cover and shift from MY to FY ice, will undoubtedly have effects on Hg cycling within the Arctic Ocean, and a few large-scale predictions on the indirect effects have been made based on current data. A decrease in overall sea ice coverage will result in the direct deposit of RGM and Hg_P onto the ocean surface rather than onto ice or snowpack

surfaces, which will decrease Hg re-emission from these surfaces and thus may increase the amount of BioHg within the ocean water column (Stern et al., 2012a). However, to which extent a decrease in overall sea ice coverage will affect the oxidation of atmospheric mercury (e.g., AMDEs) remains unknown. Declining ice cover will also increase the evasion of GEM from the ocean surface to the atmosphere, which may balance out increased deposition and leave Arctic Ocean surface Hg_T concentrations unchanged (Andersson et al., 2008; Stern et al., 2012a). Enhanced photodecomposition of $MeHg_T$ in exposed surface waters will occur, yet may not greatly affect the overall $MeHg_T$ stored in the Arctic Ocean. While there is a considerable amount of data to construct these predictions for a declining ice cover scenario, large-scale predictions on the effects of a changing sea ice type (direct effects) are difficult to construct due to many critical knowledge gaps on Hg cycling within the sea ice itself.

1.5 Research Objectives

In order to address the over-arching question on how a shift from a MY to a FY sea ice regime will affect Hg cycling within the Arctic Ocean system, further insight into the distribution and speciation of Hg in both ice types is required. Since Arctic MY ice is nearing extinction, the characterization of Hg behaviour within MYI requires immediate attention. Recent reviews, concept articles and reports, including the recent AMAP assessment (2011) have called for emphasised research on methylation processes within the Arctic Ocean system, and have highlighted processes at the sea ice-ocean interface as a focus area (Douglas et al., 2012; Sonke et al., 2013; Stern et al., 2012a). The processes responsible for incorporation of Hg into the sea ice matrix have been speculated on;

however, process driven time series observations of Hg_T concentrations in new and growing sea ice is required to further our understanding on these mechanisms.

Building directly on a recent study on Hg in Arctic FY ice (Chaulk et al., 2011), the objective of this research is to enhance and expand previous datasets, as well as elaborate on the origin and behaviour of Hg in sea ice. In specific, the two questions addressed through this research are as follows:

1. What are the mechanisms behind Hg incorporation and vertical distribution within FY and MY ice?
2. What is the speciation of Hg within MY and FY ice?

To achieve these objectives, both field and mesocosm-scale studies were carried out. At the center of the research is the hypothesis that particulate-bound Hg dominates the speciation within sea ice and thus controls the vertical distribution of Hg.

1.6 Organization of Thesis

This thesis is organized into 4 complementary chapters. Chapter 1 (this chapter) presents a thorough literature review on the current knowledge of Hg cycling within the Arctic Ocean system, with an emphasis on the sea ice environment. Chapter 2 presents a field-based study on the vertical distribution and speciation of Hg in MY ice from the Eastern Beaufort Sea and McClure Strait, Canada. It represents the first comprehensive study on mercury in MY ice, and provides the first evidence of potential occurrence of mercury methylation in MY ice. This chapter has been submitted in full to the Environmental Science and Technology (February 16th, 2014) and is in review. Chapter 3 presents a mesocosm study conducted at the Sea-ice Environmental Research Facility

(SERF) in Winnipeg, Manitoba, Canada that investigated the mechanisms of Hg incorporation and distribution during artificial sea ice formation and growth, as well as the speciation of Hg in newly formed ice. A manuscript is being prepared based on this chapter as well. Lastly, Chapter 4 presents the overall conclusions, discusses limitations of the presented work, and provides perspectives for future direction on this research area. Appendices are separated into sections based on the chapters presented, and are found at the end of the document.

1.7 References

Amos H, Jacob D, Holmes C, Fisher J, Wang Q, Yantosca R, et al. Gas-particle partitioning of atmospheric Hg (II) and its effect on global mercury deposition. Atmospheric Chemistry and Physics 2012; 12: 591-603.

Andersson M, Sommar J, Gårdfeldt K, Lindqvist O. Enhanced concentrations of dissolved gaseous mercury in the surface waters of the Arctic Ocean. Marine Chemistry 2008; 110: 190-194.

Ariya PA, Dastoor AP, Amyot M, Schroeder WH, Barrie L, Anlauf K, et al. The Arctic: a sink for mercury. Tellus B 2004; 56: 397-403.

Barber DG, Hanesiak JM. Meteorological forcing of sea ice concentrations in the southern Beaufort Sea over the period 1979 to 2000. Journal of Geophysical Research 2004; 109: C06014.

Barkay T, Gillman M, Turner RR. Effects of dissolved organic carbon and salinity on bioavailability of mercury. Applied and Environmental Microbiology 1997; 63: 4267-4271.

Barrie L, Gregor D, Hargrave B, Lake R, Muir D, Shearer R, et al. Arctic contaminants: sources, occurrence and pathways. Science of the Total Environment 1992; 122: 1-74.

Basu N, Scheuhammer AM, Rouvinen-Watt K, Grochowina N, Evans RD, O'Brien M, et al. Decreased *N*-methyl-d-aspartic acid (NMDA) receptor levels are associated with mercury exposure in wild and captive mink. Neurotoxicology 2007; 28: 587-593.

Berg T, Sekkesæter S, Steinnes E, Valdal A-K, Wibetoe G. Springtime depletion of mercury in the European Arctic as observed at Svalbard. Science of the Total Environment 2003; 304: 43-51.

Calvert JG, Lindberg SE. A modeling study of the mechanism of the halogen–ozone–mercury homogeneous reactions in the troposphere during the polar spring. Atmospheric Environment 2003; 37: 4467-4481.

Caravati EM, Erdman AR, Christianson G, Nelson LS, Woolf AD, Booze LL, et al. Elemental mercury exposure: an evidence-based consensus guideline for out-of-hospital management. Clinical Toxicology 2008; 46: 1-21.
Chaulk A. Chapter 3: Mercury behaviour in the snow pack: from spring-time deposition to melt. Department of Environment and Geography. University of Manitoba, Winnipeg, 2011.
Chaulk A, Stern GA, Armstrong D, Barber DG, Wang F. Mercury distribution and transport across the ocean− sea-ice− atmosphere interface in the Arctic Ocean. Environmental Science & Technology 2011; 45: 1866-1872.
Clarkson TW, Magos L. The toxicology of mercury and its chemical compounds. CRC Critical Reviews in Toxicology 2006; 36: 609-662.
Collins RE, Carpenter SD, Deming JW. Spatial heterogeneity and temporal dynamics of particles, bacteria, and pEPS in Arctic winter sea ice. Journal of Marine Systems 2008; 74: 902-917.
Comiso JC. A rapidly declining perennial sea ice cover in the Arctic. Geophysical Research Letters 2002; 29: 1956.
Compeau G, Bartha R. Sulfate-reducing bacteria: principal methylators of mercury in anoxic estuarine sediment. Applied and Environmental Microbiology 1985; 50: 498-502.
Cossa D, Heimbürger L-E, Lannuzel D, Rintoul SR, Butler EC, Bowie AR, et al. Mercury in the Southern Ocean. Geochimica et Cosmochimica Acta 2011; 75: 4037-4052.
Cox G, Weeks W. Salinity variations in sea ice. J. Glaciol 1974; 13: 109-120.
Dastoor AP, Larocque Y. Global circulation of atmospheric mercury: a modelling study. Atmospheric Environment 2004; 38: 147-161.
Deming JW. Sea ice bacteria and viruses. In: Thomas DN, Dieckmann GS, editors. Sea Ice. 2, 2010, pp. 247-282.
Deutch B, Dyerberg J, Pedersen HS, Asmund G, Møller P, Hansen JC. Dietary composition and contaminants in north Greenland, in the 1970s and 2004. Science of the Total Environment 2006; 370: 372-381.
Dietz R, Sonne C, Basu N, Braune B, O'Hara T, Letcher RJ, et al. What are the toxicological effects of mercury in Arctic biota? Science of the Total Environment 2013; 443: 775-790.
Dommergue A, Ferrari CP, Gauchard P-A, Boutron CF, Poissant L, Pilote M, et al. The fate of mercury species in a sub-arctic snowpack during snowmelt. Geophysical Research Letters 2003; 30: 1621.
Dommergue Al, Larose C, Faïn X, Clarisse O, Foucher D, Hintelmann H, et al. Deposition of mercury species in the Ny-Ålesund area (79 N) and their transfer during snowmelt. Environmental Science & Technology 2009; 44: 901-907.
Douglas T, Sturm M, Simpson W, Brooks S, Lindberg S, Perovich D. Elevated mercury measured in snow and frost flowers near Arctic sea ice leads. Geophysical Research Letters 2005; 32: L04502.
Douglas TA. What is the Fate of Mercury Entering the Arctic Environment?: Arctic Monitoring and Assessment Programme (AMAP), 2011.

Douglas TA, Loseto LL, Macdonald RW, Outridge P, Dommergue A, Poulain A, et al. The fate of mercury in Arctic terrestrial and aquatic ecosystems, a review. Environmental Chemistry 2012; 9: 321-355.
Douglas TA, Sturm M, Simpson WR, Blum JD, Alvarez-Aviles L, Keeler GJ, et al. Influence of snow and ice crystal formation and accumulation on mercury deposition to the Arctic. Environmental Science & Technology 2008; 42: 1542-1551.
Drinkwater MR, Crocker G. Modelling changes in the dielectric and scattering properties of young snow-covered sea ice at GHz frequencies. Journal of Glaciology 1988; 34: 274-282.
Ebinghaus R, Kock HH, Temme C, Einax JW, Löwe AG, Richter A, et al. Antarctic springtime depletion of atmospheric mercury. Environmental Science & Technology 2002; 36: 1238-1244.
Eide L, Martin S. The formation of brine drainage features in young sea ice. Journal of Glaciology 1975; 14: 137-154.
Feltham DL. Sea ice rheology. Annual Review Fluid Mechanics 2008; 40: 91-112.
Ferrari CP, Dommergue A, Boutron CF, Jitaru P, Adams FC. Profiles of mercury in the snow pack at Station Nord, Greenland shortly after polar sunrise. Geophysical Research Letters 2004; 31: L03401.
Ferrari CP, Gauchard P-A, Aspmo K, Dommergue A, Magand O, Bahlmann E, et al. Snow-to-air exchanges of mercury in an Arctic seasonal snow pack in Ny-Ålesund, Svalbard. Atmospheric Environment 2005; 39: 7633-7645.
Fetterer F, Untersteiner N. Observations of melt ponds on Arctic sea ice. Journal of Geophysical Research 1998; 103: 24821-24,835.
Fleming EJ, Mack EE, Green PG, Nelson DC. Mercury methylation from unexpected sources: molybdate-inhibited freshwater sediments and an iron-reducing bacterium. Applied and Environmental Microbiology 2006; 72: 457-464.
Gårdfeldt K, Munthe J, Strömberg D, Lindqvist O. A kinetic study on the abiotic methylation of divalent mercury in the aqueous phase. Science of the Total Environment 2003; 304: 127-136.
Golden K, Eicken H, Heaton A, Miner J, Pringle D, Zhu J. Thermal evolution of permeability and microstructure in sea ice. Geophysical Research Letters 2007; 34.
Gosink TA, Pearson JG, Kelley JJ. Gas movement through sea ice. Nature 1976; 263: 41-42.
Gow AJ, Ackley SF, Buck KR, Golden KM. Physical and structural characteristics of Weddell Sea pack ice. DTIC Document, 1987.
Gow AJ, Meese DA, Perovich DK, Tucker WB. The anatomy of a freezing lead. Journal of Geophysical Research: Oceans (1978–2012) 1990; 95: 18221-18232.
Haas C. Dynamics versus thermodynamics: The sea ice thickness distribution. In: Thomas DN, Dieckmann GS, editors. Sea Ice. 2nd Ed. Wiley-Blackwell, Chichester, UK, 2010: 82
Hammerschmidt CR, Lamborg CH, Fitzgerald WF. Aqueous phase methylation as a potential source of methylmercury in wet deposition. Atmospheric Environment 2007; 41: 1663-1668.

Hans Wedepohl K. The composition of the continental crust. Geochimica et Cosmochimica Acta 1995; 59: 1217-1232.
Hirdman D, Aspmo K, Burkhart J, Eckhardt S, Sodemann H, Stohl A. Transport of mercury in the Arctic atmosphere: Evidence for a spring-time net sink and summer-time source. Geophysical Research Letters 2009; 36.
Holmes CD, Jacob DJ, Yang X. Global lifetime of elemental mercury against oxidation by atomic bromine in the free troposphere. Geophysical Research Letters 2006; 33: L20808.
Hylander LD, Meili M. 500 years of mercury production: global annual inventory by region until 2000 and associated emissions. Science of the Total Environment 2003; 304: 13-27.
Jackson T. Long-range atmospheric transport of mercury to ecosystems, and the importance of anthropogenic emissions A critical review and evaluation of the published evidence. Environmental Reviews 1997; 5: 99-120.
Johnson KP, Blum JD, Keeler GJ, Douglas TA. Investigation of the deposition and emission of mercury in arctic snow during an atmospheric mercury depletion event. Journal of Geophysical Research: Atmospheres (1984–2012) 2008; 113.
Keeler G, Glinsorn G, Pirrone N. Particulate mercury in the atmosphere: its significance, transport, transformation and sources. Mercury as a Global Pollutant. Springer, 1995, pp. 159-168.
Kerin EJ, Gilmour CC, Roden E, Suzuki M, Coates J, Mason R. Mercury methylation by dissimilatory iron-reducing bacteria. Applied and Environmental Microbiology 2006; 72: 7919-7921.
Kirk JL, St. Louis VL, Hintelmann H, Lehnherr I, Else B, Poissant L. Methylated mercury species in marine waters of the Canadian high and sub Arctic. Environmental Science & Technology 2008; 42: 8367-8373.
Krembs C, Engel A. Abundance and variability of microorganisms and transparent exopolymer particles across the ice–water interface of melting first-year sea ice in the Laptev Sea (Arctic). Marine Biology 2001; 138: 173-185.
Kwok R, Cunningham G, Wensnahan M, Rigor I, Zwally H, Yi D. Thinning and volume loss of the Arctic Ocean sea ice cover: 2003–2008. Journal of Geophysical Research: Oceans (1978–2012) 2009; 114.
Kwok R, Rignot E, Holt B, Onstott R. Identification of sea ice types in spaceborne synthetic aperture radar data. Journal of Geophysical Research: Oceans (1978–2012) 1992; 97: 2391-2402.
Lahoutifard N, Sparling M, Lean D. Total and methyl mercury patterns in Arctic snow during springtime at Resolute, Nunavut, Canada. Atmospheric Environment 2005; 39: 7597-7606.
Lalonde JD, Poulain AJ, Amyot M. The role of mercury redox reactions in snow on snow-to-air mercury transfer. Environmental Science & Technology 2002; 36: 174-178.
Lange M, Hubberten H-W. Isotopic composition of sea ice as a tool for understanding sea ice processes in the polar regions. Physics and chemistry of ice (N Maeno, T Hondoh, eds) Hokkaido Univ Pr, Sapporo 1992: 399-405.
Larose C, Dommergue A, De Angelis M, Cossa D, Averty B, Marusczak N, et al. Springtime changes in snow chemistry lead to new insights into mercury

methylation in the Arctic. Geochimica et Cosmochimica Acta 2010; 74: 6263-6275.
Lehnherr I, Louis VLS, Hintelmann H, Kirk JL. Methylation of inorganic mercury in polar marine waters. Nature Geoscience 2011; 4: 298-302.
Lemes M, Wang F, Stern GA, Ostertag SK, Chan HM. Methylmercury and selenium speciation in different tissues of beluga whales (Delphinapterus leucas) from the western Canadian Arctic. Environmental Toxicology and Chemistry 2011; 30: 2732-2738.
Liao J, Huey LG, Liu Z, Tanner DJ, Cantrell CA, Orlando JJ, et al. High levels of molecular chlorine in the Arctic atmosphere. Nature Geoscience 2014.
Light B, Maykut G, Grenfell T. Effects of temperature on the microstructure of first-year Arctic sea ice. Journal of Geophysical Research: Oceans (1978–2012) 2003; 108.
Lin CC, Yee N, Barkay T. Microbial transformations in the mercury cycle. In: Liu G, Cai Y, O'Driscoll N, editors. Environmental Chemistry and Toxicology of Mercury. John Wiley and Sons, Inc, Hoboken, New Jersey 2012: 155-191.
Lindberg S, Brooks S, Lin C, Scott K, Meyers T, Chambers L, et al. Formation of reactive gaseous mercury in the Arctic: evidence of oxidation of Hg to gas-phase Hg-II compounds after Arctic sunrise. Water, Air and Soil Pollution: Focus 2001; 1: 295-302.
Lindberg SE, Brooks S, Lin CJ, Scott KJ, Landis MS, Stevens RK, et al. Dynamic oxidation of gaseous mercury in the Arctic troposphere at polar sunrise. Environmental Science & Technology 2002; 36: 1245-1256.
Liu G, Cai Y, O'Driscoll N, Feng X, Jiang G. Overview of Mercury in the Environment. In: Liu G, Cai Y, O'Driscoll N, editors. Environmental Chemistry and Toxicology of Mercury. John Wiley and Sons, Inc, Hoboken, New Jersey 2012: 1-12.
Lockhart W, Stern G, Wagemann R, Hunt R, Metner D, DeLaronde J, et al. Concentrations of mercury in tissues of beluga whales (*Delphinapterus leucas*) from several communities in the Canadian Arctic from 1981 to 2002. Science of the Total Environment 2005; 351: 391-412.
Lu JY, Schroeder WH, Barrie LA, Steffen A, Welch HE, Martin K, et al. Magnification of atmospheric mercury deposition to polar regions in springtime: the link to tropospheric ozone depletion chemistry. Geophysical Research Letters 2001; 28: 3219-3222.
Macdonald R, Loseto L. Are Arctic Ocean ecosystems exceptionally vulnerable to global emissions of mercury? A call for emphasised research on methylation and the consequences of climate change. Environmental Chemistry 2010; 7: 133-138.
Major MA, Rosenblatt DH, Bostian KA. The octanol/water partition coefficient of methylmercuric chloride and methylmercuric hydroxide in pure water and salt solutions. Environmental Toxicology and Chemistry 1991; 10: 5-8.
Maykut GA, Untersteiner N. Some results from a time-dependent thermodynamic model of sea ice. Journal of Geophysical Research 1971; 76: 1550-1575.
Melling H, Riedel DA, Gedalof Ze. Trends in the draft and extent of seasonal pack ice, Canadian Beaufort Sea. Geophysical Research Letters 2005; 32.
Moore CW, Obrist D, Steffen A, Staebler RM, Douglas TA, Richter A, et al. Convective forcing of mercury and ozone in the Arctic boundary layer induced by leads in sea ice. Nature 2014.

Muir D, Wagemann R, Hargrave B, Thomas D, Peakall D, Norstrom R. Arctic marine ecosystem contamination. Science of the Total Environment 1992; 122: 75-134.
Munthe J, Wängberg I, Iverfeldt Å, Lindqvist O, Strömberg D, Sommar J, et al. Distribution of atmospheric mercury species in Northern Europe: final results from the MOE project. Atmospheric Environment 2003; 37: 9-20.
Munthe J, Wängberg I, Pirrone N, Iverfeldt Å, Ferrara R, Ebinghaus R, et al. Intercomparison of methods for sampling and analysis of atmospheric mercury species. Atmospheric Environment 2001; 35: 3007-3017.
Niedrauer TM, Martin S. An experimental study of brine drainage and convection in young sea ice. Journal of Geophysical Research 1979; 84: 1176-1186.
NSIDC;. Arctic sea ice extent settles at record seasonal minimum. Arctic Sea Ice News & Analysis, 2012.
Ostertag SK, Stern GA, Chan HM. Mercury concentration and distribution in brains from belugas (*Delphinapterus leucas*) harvested in the western Canadian Arctic. Oral Presentation. Presented at the International Conference on Mercury as a Global Pollutant, Guiyang, China, 2009.
Outridge P, Macdonald R, Wang F, Stern G, Dastoor A. A mass balance inventory of mercury in the Arctic Ocean. Environmental Chemistry 2008; 5: 89-111.
Parkinson CL, Cavalieri DJ. Arctic sea ice variability and trends, 1979–2006. Journal of Geophysical Research: Oceans (1978–2012) 2008; 113.
Petrich C, Eicken H. Growth, structure and properties of sea ice. In: Thomas DN, Dieckmann GS, editors. Sea Ice. 2nd Ed. Wiley-Blackwell, Chichester, UK, 2010, pp. 23-77.
Pfirman S, Lange M, Wollenburg I, Schlosser P. Sea ice characteristics and the role of sediment inclusions in deep-sea deposition: Arctic—Antarctic comparisons. Geological history of the polar oceans: Arctic versus Antarctic. Springer, 1990, pp. 187-211.
Pirrone N, Cinnirella S, Feng X, Finkelman R, Friedli H, Leaner J, et al. Global mercury emissions to the atmosphere from anthropogenic and natural sources. Atmospheric Chemistry and Physics 2010; 10: 5951-5964.
Poissant L, Pilote M. Time series analysis of atmospheric mercury in Kuujjuarapik/Whapmagoostui (Quebec). Journal de Physique IV (Proceedings). 107, 2003, pp. 1079-1082.
Pongratz R, Heumann KG. Production of methylated mercury, lead, and cadmium by marine bacteria as a significant natural source for atmospheric heavy metals in polar regions. Chemosphere 1999; 39: 89-102.
Poulain AJ, Lalonde JD, Amyot M, Shead JA, Raofie F, Ariya PA. Redox transformations of mercury in an Arctic snowpack at springtime. Atmospheric Environment 2004; 38: 6763-6774.
Saha J, McKinlay K. Use of mercury in agriculture and its relationship to environmental pollution. Toxicological & Environmental Chemistry 1973; 1: 271-290.
Schroeder W, Anlauf K, Barrie L, Lu J, Steffen A, Schneeberger D, et al. Arctic springtime depletion of mercury. Nature 1998; 394: 331-332.
Schroeder WH, Munthe J. Atmospheric mercury—an overview. Atmospheric Environment 1998; 32: 809-822.

Serreze M, Maslanik J, Scambos T, Fetterer F, Stroeve J, Knowles K, et al. A record minimum arctic sea ice extent and area in 2002. Geophysical Research Letters 2003; 30: 1110.

Sherman LS, Blum JD, Johnson KP, Keeler GJ, Barres JA, Douglas TA. Mass-independent fractionation of mercury isotopes in Arctic snow driven by sunlight. Nature Geoscience 2010; 3: 173-177.

Simpson W, Carlson D, Hönninger G, Douglas T, Sturm M, Perovich D, et al. First-year sea-ice contact predicts bromine monoxide (BrO) levels at Barrow, Alaska better than potential frost flower contact. Atmospheric Chemistry and Physics 2007; 7: 621-627.

Sinha N. Uniaxial compressive strength of first-year and multi-year sea ice. Canadian Journal of Civil Engineering 1984; 11: 82-91.

Skov H, Christensen JH, Goodsite ME, Heidam NZ, Jensen B, Wåhlin P, et al. Fate of elemental mercury in the Arctic during atmospheric mercury depletion episodes and the load of atmospheric mercury to the Arctic. Environmental Science & Technology 2004; 38: 2373-2382.

Sommar J, Andersson M, Jacobi H-W. Circumpolar measurements of speciated mercury, ozone and carbon monoxide in the boundary layer of the Arctic Ocean. Atmospheric Chemistry and Physics 2010; 10: 5031-5045.

Sommar J, Gårdfeldt K, Strömberg D, Feng X. A kinetic study of the gas-phase reaction between the hydroxyl radical and atomic mercury. Atmospheric Environment 2001; 35: 3049-3054.

Sonke JE, Heimbürger L-E, Dommergue A. Mercury biogeochemistry: Paradigm shifts, outstanding issues and research needs. Comptes Rendus Geoscience 2013; 345: 213-224.

St Louis VL, Hintelmann H, Graydon JA, Kirk JL, Barker J, Dimock B, et al. Methylated mercury species in Canadian high arctic marine surface waters and snowpacks. Environmental Science & Technology 2007; 41: 6433-6441.

St. Louis VL, Rudd JW, Kelly CA, Beaty KG, Bloom NS, Flett RJ. Importance of wetlands as sources of methyl mercury to boreal forest ecosystems. Canadian Journal of Fisheries and Aquatic Sciences 1994; 51: 1065-1076.

St. Louis VL, Sharp MJ, Steffen A, May A, Barker J, Kirk JL, et al. Some sources and sinks of monomethyl and inorganic mercury on Ellesmere Island in the Canadian High Arctic. Environmental Science & Technology 2005; 39: 2686-2701.

Steffen A, Douglas T, Amyot M, Ariya P, Aspmo K, Berg T, et al. A synthesis of atmospheric mercury depletion event chemistry in the atmosphere and snow. Atmospheric Chemistry and Physics 2008; 8: 1445-1482.

Steffen A, Schroeder W, Macdonald R, Poissant L, Konoplev A. Mercury in the Arctic atmosphere: An analysis of eight years of measurements of GEM at Alert (Canada) and a comparison with observations at Amderma (Russia) and Kuujjuarapik (Canada). Science of the Total Environment 2005; 342: 185-198.

Stern GA, Macdonald RW, Outridge PM, Wilson S, Chételat J, Cole A, et al. How does climate change influence arctic mercury? Science of the Total Environment 2012; 414: 22-42.

Stroeve J, Holland MM, Meier W, Scambos T, Serreze M. Arctic sea ice decline: Faster than forecast. Geophysical Research Letters 2007; 34.

Stroeve J, Serreze M, Drobot S, Gearheard S, Holland M, Maslanik J, et al. Arctic sea ice extent plummets in 2007. Eos, Transactions American Geophysical Union 2008; 89: 13-14.
Stroeve J, Serreze M, Fetterer F, Arbetter T, Meier W, Maslanik J, et al. Tracking the Arctic's shrinking ice cover: Another extreme September minimum in 2004. Geophysical Research Letters 2005; 32.
Subir M, Ariya PA, Dastoor AP. A review of the sources of uncertainties in atmospheric mercury modeling II. Mercury surface and heterogeneous chemistry–A missing link. Atmospheric Environment 2012; 46: 1-10.
Swartzendruber PC, Jaffe DA, Prestbo E, Weiss-Penzias P, Selin NE, Park R, et al. Observations of reactive gaseous mercury in the free troposphere at the Mount Bachelor Observatory. Journal of Geophysical Research: Atmospheres (1984–2012) 2006; 111.
Tang S, Qin D, Ren J, Kang J, Li Z. Structure, salinity and isotopic composition of multi-year landfast sea ice in Nella Fjord, Antarctica. Cold Regions Science and Technology 2007; 49: 170-177.
Thomas DN, Lara RJ, Eicken H, Kattner G, Skoog A. Dissolved organic matter in Arctic multi-year sea ice during winter: major components and relationship to ice characteristics. Polar Biology 1995; 15: 477-483.
Tian W, Egeland GM, Sobol I, Chan HM. Mercury hair concentrations and dietary exposure among Inuit preschool children in Nunavut, Canada. Environment International 2011; 37: 42-48.
Timco G, Weeks W. A review of the engineering properties of sea ice. Cold Regions Science and Technology 2010; 60: 107-129.
Tucker III W, Perovich DK, Gow AJ, Weeks WF, Drinkwater MR. Physical properties of sea ice relevant to remote sensing. Geophysical Monograph Series. 68, 1992, pp. 9-28.
Ullrich SM, Tanton TW, Abdrashitova SA. Mercury in the aquatic environment: a review of factors affecting methylation. Critical Reviews in Environmental Science and Technology 2001; 31: 241-293.
UNEP. Global Mercury Assessment 2013: Sources, Emissions, Releases and Environmental Transport. UNEP Chemicals Branch, Geneva, Switzerland, 2013a.
UNEP. Minamata Convention Agreed by Nations UNEP News Centre, 2013b.
US Environmental Protection Agency. Mercury: Consumer and Commercial Products. 2013, 2012.
Wagemann R, Lockhart W, Welch H, Innes S. Arctic marine mammals as integrators and indicators of mercury in the Arctic. Mercury as a Global Pollutant. Springer, 1995, pp. 683-693.
Wagemann R, Muir DCG. Concentrations of heavy metals and organochlorines in marine mammals of northern waters: overview and evaluation: Western Region, Department of Fisheries and Oceans Canada, 1984.
Wang F, Macdonald RW, Armstrong DA, Stern GA. Total and Methylated Mercury in the Beaufort Sea: The Role of Local and Recent Organic Remineralization. Environmental Science & Technology 2012; 46: 11821-11828.

Wang F, Macdonald RW, Stern GA, Outridge PM. When noise becomes the signal: Chemical contamination of aquatic ecosystems under a changing climate. Marine Pollution Bulletin 2010; 60: 1633-1635.

Weeks WF, Ackley SF. The growth, structure and properties of sea ice. The Geophysics of Sea Ice. 146, 1986: 9-164.

Widdel F, Hansen T, Balows A, Truper H, Dworkin M, Harder W, et al. The dissimilatory sulfate-and sulfur-reducing bacteria. The prokaryotes: a handbook on the biology of bacteria: ecophysiology, isolation, identification, applications, vol. I. 1992: 582-624.

Zhang L, Wong M. Environmental mercury contamination in China: sources and impacts. Environment International 2007; 33: 108-121.

Chapter 2: Total and Methylated Mercury in Arctic Multiyear Sea Ice

This chapter has recently been submitted to Environmental Science and Technology:

Beattie S.A., Armstrong D., Chaulk A., Comte J., Gosselin M., and Wang F.
Total and methylated mercury in Arctic multiyear sea ice.
Environmental Science and Technology. In review.

I led the fieldwork, collected the multiyear ice cores, performed the analysis for total and methylated mercury, and wrote the first version of the manuscript. My supervisor (Wang) initiated and directed the project, helped with interpretation of the results, and revised the manuscript. Co-authors Armstrong and Chaulk assisted with field sampling and laboratory analysis. Co-author Comte performed the bacterial enumeration analysis for one of the multiyear sea ice cores, and Gosselin directed the organic carbon analysis of the other ice core.

2.0 Abstract

Mercury is one of the primary contaminants of concern in the Arctic marine ecosystem. While considerable efforts have been directed toward understanding mercury cycling in the Arctic, little is known about mercury dynamics within Arctic multiyear sea ice which is being rapidly replaced with first-year ice. Here we report the first study on the distribution, transport and transformation of mercury in Arctic multiyear sea ice. Based on three multiyear ice cores taken from the eastern Beaufort Sea and McClure Strait, total mercury concentrations ranged from 0.13 to 12.20 ng L^{-1} in bulk ice, with the highest values occurring in the topmost layer (~30 cm) which can be attributed to particulate dynamics. Methylated mercury concentrations ranged from below the method detection limit (<0.02 ng L^{-1}) to as high as 0.53 ng L^{-1}. The ratio of methylated to total mercury peaked, up to ~40%, in the mid- to bottom-sections of the ice, suggesting the potential occurrence of in situ mercury methylation. The annual fluxes of total and methylated mercury into the Arctic Ocean via melt of multiyear ice are estimated to be 420 and 42 kg yr^{-1}, respectively, representing an important seasonal source of mercury into the Arctic Ocean marine ecosystem.

2.1 Introduction

High concentrations of mercury (Hg) have been reported within tissues of Arctic marine mammals (AMAP, 2011), raising health concerns for the animals as well as the Northern People who rely on the animal tissues as part of their traditional diet (AMAP, 2009). The extensive research efforts that ensued found high spatial and temporal variability of Hg in upper trophic-level marine biota, which cannot be fully explained by atmospheric loading histories alone (Outridge et al., 2008; Wang et al., 2010a). It has been suggested that changes within the Arctic system have altered post-depositional biogeochemical processes that dictate the transport, transformation and biological uptake of Hg in the Arctic Ocean (Macdonald et al., 2005; Stern et al., 2012b; Wang et al., 2010a). Processes that require immediate attention are those which produce or release monomethylmercury (including CH_3Hg^+ and its complexes, hereafter MMHg collectively), the primary Hg species that causes biological concerns due to its neurotoxicity and bioaccumulative nature (Wang et al., 2012). Arguably the most dramatic change the Arctic Ocean has undergone recently has been the shift in composition of the icescape. Record low summer sea ice extent events, as observed in 2007 and 2012, demonstrate the extensive loss of multiyear (MY) ice and continue to compromise the resilience of the permanent icepack (Comiso, 2012; Maslanik et al., 2007a; Maslanik et al., 2011; Nghiem et al., 2007). The effects of this shift from a multiyear (MY) to a first-year (FY) ice regime on the biogeochemical cycling of Hg within the Arctic Ocean system remain unknown.

Recognized as a fundamental component of the Arctic system, sea ice is a heterogeneous, multi-phase matrix comprised of ice, brine, gases, minerals, particulate

matter, and biota (e.g., viruses, archaea, bacteria, algae, and meiofauna) (Deming, 2009; Petrich and Eicken, 2010). After initial nucleation and formation, ice growth and evolution is driven by various physical, chemical and biological processes which govern the micro- and macro-properties of sea ice (Petrich and Eicken, 2010; Thomas et al., 2010). Brine pockets and drainage channels increase the permeability of sea ice to the transport of gases, solutes and particulate matter, with vertical fluid permeability being a function of porosity and brine volume fraction, which are in turn a function of temperature and salinity of the bulk ice (Petrich and Eicken, 2010; Thomas et al., 2010). Recent studies on FY ice have found Hg to heavily concentrate in the brine phase, and therefore the fluid dynamics of the brine strongly influences Hg distribution and transport within the ice column (Chaulk et al., 2011; Cossa et al., 2011). This characteristic has strong implications when considering the brine dynamics of FY and MY ice. The evolution of MY ice through the melt season is driven by two distinct processes: desalination and crystal retexturing (Tucker III et al., 1992). The enhanced brine dynamics of MY ice will likely influence Hg distribution within the ice column and transport across the ocean – sea-ice – atmosphere (OSA) interface. Although the distribution of Hg in young and FY ice has been studied in some detail (Chaulk et al., 2011; Cossa et al., 2011), so far the Hg distribution profile in MY ice has only been reported for a single core collected in 2008 (Chaulk et al., 2011).

Of particular pertinence is the recent discovery of local anaerobic conditions within sea ice (Rysgaard and Glud, 2004; Rysgaard et al., 2008). It is well established that the production of MMHg is favored in redox transition zones where some dissimilatory sulphate-reducing bacteria (Compeau and Bartha, 1985) and iron-reducing

bacteria thrive (Fleming et al., 2006; Kerin et al., 2006). Laboratory studies have identified pure cultures of psychrotrophic bacteria which inhabit polar surface seawater and can methylate Hg under cold conditions;(Pongratz and Heumann, 1999) however, it is not yet known whether Hg methylation occurs in sea ice. Sea ice does support higher bacterial activity than underlying seawater, and bacterial carbon biomass ranging from 0.09-0.87 μM has been reported in the bottom 5 cm of FY ice in the Amundsen Gulf (Nguyen and Maranger, 2011). Measurement of MMHg and full characterization of Hg speciation within the sea ice matrix is thus warranted.

Furthermore, sea ice may act as an environmental reservoir for Hg, and due to differences in volume and rates of advective brine efflux the residence times of Hg within MY ice and FY ice are likely unequal. The complete melt of MY ice may lead to substantial seasonal loading of Hg into the Arctic Ocean if the efflux is larger in magnitude than the influx of oceanic Hg into FY sea ice (Chaulk et al., 2011).

This paper aims to better define the role of MY ice in the biogeochemical cycling of Hg in the Arctic Ocean by investigating its potential as a transformation medium for methylmercury production, and as a source of Hg and methylmercury into the aquatic ecosystem. The processes governing Hg distribution within MY ice is also assessed. To our knowledge this work represents the first measurement of methylmercury in MY ice.

2.2 Materials and Procedures

2.2.1 Sampling and Sample Preparation

The sea ice cores were retrieved from MY ice floes in the eastern Beaufort Sea and McClure Strait of the Arctic Ocean (Figure 2.1), where the median September old ice (essentially all MY ice) concentration, expressed as aerial coverage, ranged from 7-10/10 and 4-6/10, respectively, for the period 1981-2010 (Canadian Ice Service; http://ec.gc.ca/glaces-ice). Details of the study area can be found in the Appendices (Appendix A2.1).

The first MY ice site, MY1 (ice thickness: 350 cm), was cored on May 25, 2008 in the eastern Beaufort Sea, for which total Hg data have been reported in (Chaulk et al., 2011); however, this core was not analyzed for methylated Hg. Two new MY sites were cored in our study. Site MY2 (ice thickness: 370 cm) was collected on August 16, 2011 in the northeastern Beaufort Sea and site MY3 (ice thickness: 270 cm) on September 9, 2013 in McClure Strait. All the coring was carried out during ArcticNet cruises of the Canadian Research Icebreaker CCGS Amundsen. At the time of sampling, the MY floe at site MY2 showed deformed surfaces and melt ponds; in contrast, melt ponds were not visible within the immediate vicinity of sites MY1 and MY3, though the ice surfaces possessed undulating features.

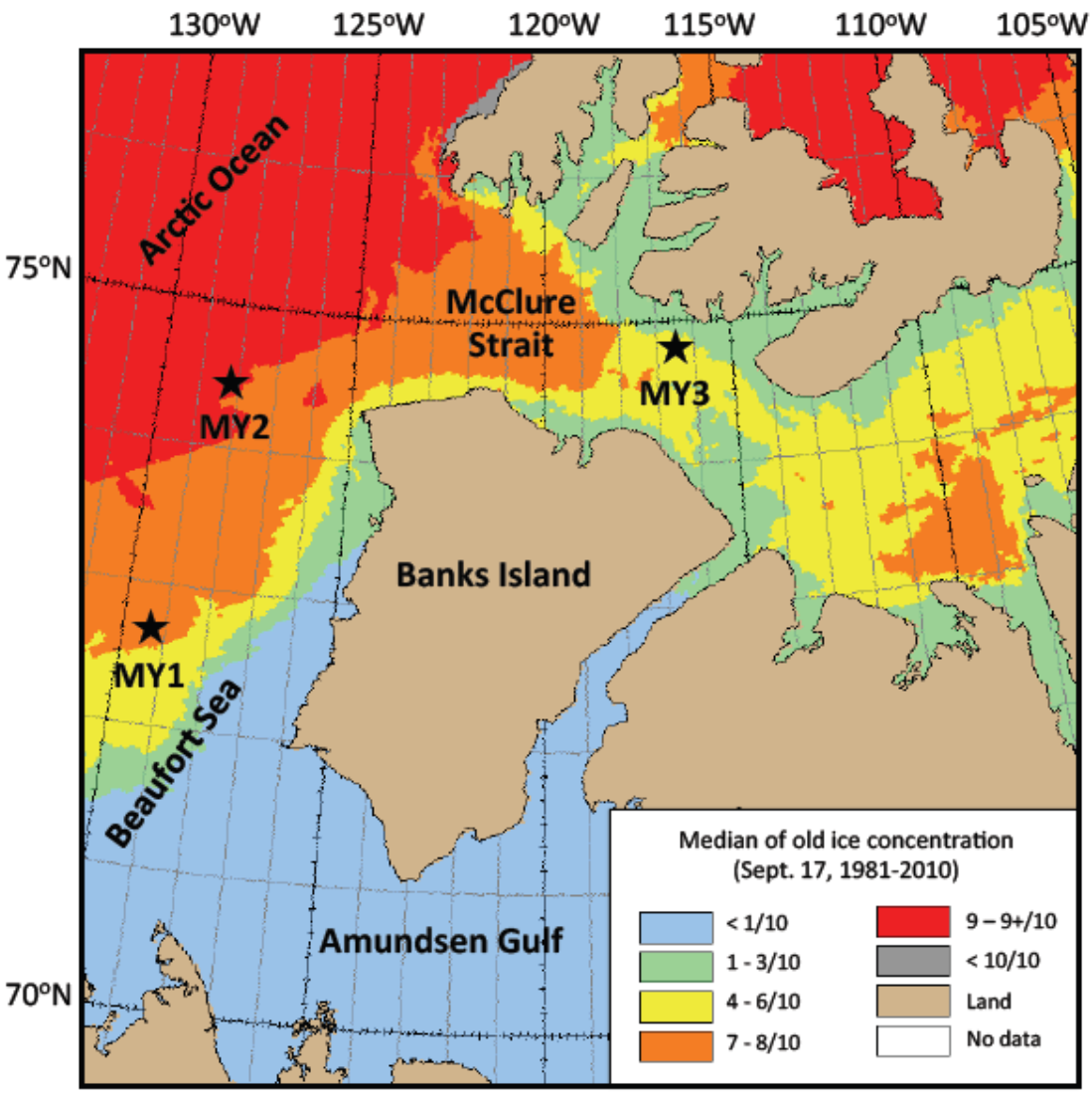

Figure 2.1: Locations of multiyear sea ice sampling sites MY2 (August 16, 2011) and MY3 (September 9, 2013), overlaid onto a 30-yr sea ice climatic atlas of median old ice concentration for September 17 (1981-2010) generated by Canadian Ice Service of Environment Canada (http://ec.gc.ca/glaces-ice). Also shown is the location of MY1 from an earlier study (May 25, 2008) (Chaulk et al., 2011).

All cores were collected using a Mark II Kovacs core barrel (i.d. = 9 cm) in 1 m sections. At each site, four replicate ice cores spanning the entire ice thickness were taken from areas where the overlying snowpack had been removed to bare ice surface. One of the replicate cores was for the measurement of total Hg (Hg_T), one for total methylated Hg ($MeHg_T$), one for in-situ temperature, and the fourth for salinity and other ancillary

parameters. An additional ice core was taken at Site MY3 for bacterial enumeration. Sea ice temperature (T) was measured in situ immediately after core retrieval. Holes (~4.5 cm deep) were drilled at 10 cm intervals down the length of the core, and a Model 400 thermometer (Traceable Control Company) was inserted into each hole for measurement. All other cores were placed into plastic bags and stored inside the cold lab (-20°C) onboard the icebreaker.

Once inside the cold lab, the ice cores were cut into 5 to 10 cm sections. The cores for Hg_T and $MeHg_T$ analysis were halved to produce pseudo-replicates. The outer 1 cm layer of the cores was scraped off using pre-cleaned ceramic blade knives (Kyocera) as described elsewhere (Chaulk et al., 2011). Sampling and sample preparation strictly followed the clean hands-dirty hands protocol (Fitzgerald, 1999b) at the Portable In-situ Laboratory for Mercury Speciation (PILMS), a Class 100 cleanroom laboratory onboard the icebreaker. All sampling tools were pre-cleaned and tested for acceptable background Hg levels (<0.5 pM) prior to use, and doubly bagged separately in new Ziploc® bags. Ultrapure Milli-Q Element water (Millipore) produced in PILMS was used as laboratory water. After being melted in PILMS, samples for Hg_T analysis were transferred into new 50 mL polypropylene Falcon tubes (BD) which had been shown to contain extremely low levels of background Hg (Chaulk et al., 2011); nevertheless, random tests were carried out for every batch of new tubes. Samples were spiked with 250 µL of concentrated ultrapure HCl (JT Baker) and 250 µL of BrCl (prepared from KBr and $KBrO_3$, JT Baker, in ultrapure HCl) prior to analysis at PILMS onboard the ship. Samples for $MeHg_T$ analysis were transferred into 150 mL pre-cleaned and pre-tested Teflon sample

containers, packed into a large cooler (-10°C) and shipped to the University of Manitoba for analysis.

The ice samples from the other replicate cores were melted under low light conditions for the analysis of salinity, $\delta^{18}O$, dissolved organic carbon (DOC), chlorophyll *a* (Chl *a*), and bacterial enumeration. Subsamples for $\delta^{18}O$ analysis were decanted into 20 mL clear glass scintillation vials and stored at 4°C in the dark until analysis. Subsample for DOC was filtered through pre-combusted (450°C for 5 h) Whatman GF/F filters (0.7 µm nominal pore size). The filtrate was collected in 9 mL glass storage vials with Teflon-lined caps previously cleaned following the protocol of (Burdige and Homstead, 1994) and acidified to ~pH 2 with 100 µL of 2N HCl. The DOC samples were kept at 4°C in the dark until analysis. Subsamples for Chl *a* were also filtered onto Whatman GF/F filters.

2.2.2 Analyses

Hg_T analysis was carried out in PILMS, within 24-36 h of core processing, by cold vapor atomic fluorescence spectroscopy (CVAFS) on a Tekran 2600 Hg analyzer in accordance with U.S. EPA Method 1631 (USEPA, 2002). Certified reference material (CRM) BCR®-579 coastal seawater ($[Hg_T]$ = 1.85 ± 0.50 ng L^{-1}; (Institute for Reference Materials and Measurements, Belgium) was employed as a quality control measure, and the recovery varied from 96 - 112 %. The method detection limit (MDL) was 0.01 ng L^{-1} and Hg_T levels in field blanks were below <0.07 ng L^{-1} (field blank corrections were not applied to the data). Note that the Hg_T data reported is unfiltered, and represents all Hg species (dissolved and particulate; inorganic and organic).

$MeHg_T$ analysis was performed at the Class 100, metal-free Ultraclean Trace Elements Laboratory (UCTEL) at the University of Manitoba. Samples were stored in a dedicated chest freezer (-18°C) and analyzed within 8 months of sampling. Two different analytical procedures were used. Analysis of $MeHg_T$ in MY2 samples followed U.S. EPA Method 1630 (USEPA, 2001) as described elsewhere (Wang et al., 2012). Briefly, after being melted under low light conditions, 50 mL aliquots were decanted into pre-cleaned Teflon distillation vials and spiked with 100 µL of 9 M H_2SO_4 (OmniTrace Ultra™, EMD) and 250 µL of a 20% KCl / 0.2% $_L$-cysteine (Sigma) solution which acted as a matrix modifier, before being distilled with the Brooks Rand Distillation System for 2.5 h under ultrapure N_2 flow. After being frozen overnight, distillates were neutralized with KOH, buffered to pH = 4.9 with 600 µL acetate buffer (4 M), then spiked with 40 µL of sodium tetraethylborate (Sigma) in KOH (Sigma) and analyzed on a MERX automated MeHg analyzer (Brooks Rand), which employs gas chromatographic (GC) separation followed by CVAFS detection. Analysis of $MeHg_T$ in MY3 samples followed a similar procedure except without the distillation process as described in (Bowman and Hammerschmidt, 2011). In brief, the melted sample aliquots were spiked with 500 µL of 9 M H_2SO_4, kept in dark at 4^{o}C for over 12 h prior to neutralization by NaOH, followed by direct ethylation and GC-CVAFS detection. The MDL for both methods was 0.1 pM, and field blanks were <0.2 pM (field blank corrections were not applied to the data). Since no seawater CRMs were available for MeHg analysis, quality control was done by spiking all the samples with 20 µL of a 5 nM n-propylmercuric chloride solution (Anachemia) and recoveries ranged from 61-127%. It should be noted that under acidic preservation conditions, dimethylmercury (DMHg) will rapidly decompose to MMHg,

and thus $MeHg_T$ data reported here represents the sum of MMHg and DMHg (Parker and Bloom, 2005; Wang et al., 2012) in unfiltered, melted bulk sea ice.

$\delta^{18}O$ analysis was done at the G.G. Hatch Isotope Laboratories, University of Ottawa, Canada. Samples were flushed with a gas mixture of 2% CO_2 in helium off-line, equilibrated at 21°C for 5 d, then analyzed using the Gasbench + DeltaPlus XP isotope ratio mass spectrometer (ThermoFinnigan). Analytical precision was ± 0.15 ‰ (standard deviation), and the $\delta^{18}O$ values were reported against the Vienna Standard Mean Ocean Water (VSMOW).

DOC was determined on a high-temperature combustion Shimadzu TOC-V_{CPN} Total Organic Carbon Analyzer, at the Institut des sciences de la mer de Rimouski (ISMER), Canada, following the procedure given in (Whitehead et al., 2000). Potassium hydrogen phthalate was used to standardize DOC measurements. In addition, samples were systematically checked against low carbon water (1 µM) and deep seawater reference water (Florida Strait at 700 m; 40.8 – 44.2 µM) every seventh sample analysis. These seawater DOC reference standards were produced by the Hansell's Consensus Reference Materials project. The recoveries ranged from 83–104 %. Concentrations of Chl *a* were measured on board the ship with a Turner Designs Model 10-AU fluorometer after 20 h of pigment extraction in 90% acetone at 4°C in the dark (Parsons et al., 1984).

Bacterial enumeration and analyses of single-cell characteristics were carried out using a FACScalibur flow cytometer (Becton Dickinson), equipped with an argon laser. Samples were processed at the lowest flow rate (12 µL min^{-1}), using 1 µm yellow green microspheres (Polysciences) solution as the internal standard. Beads concentration was controlled using Truecount Absolute counting tubes (BD biosciences). For total counts

and the enumeration of cells with high (HNA) or low (LNA) nucleic acid content, samples were stained with a 40 µL mL^{-1} of nucleic acid dye SYBR Green I for 10 min in the dark. Stained cells were then discriminated on the basis of their green fluorescence at 530 nm (FL1) and their 90^{o} light scatter signals while being excited at 488 nm. Manual gating was used to discriminate both HNA and LNA fractions. Data were analyzed using the CellQuest Pro software.

Salinity of the bulk ice was measured using a sensION5 conductivity meter (Hach). The brine volume fraction (V_b) in bulk sea ice was calculated from temperature and salinity of bulk ice following the empirical equations of (Leppäranta and Manninen, 1988), when $0 \geq T > -2\ ^{0}C$, or (Cox and Weeks, 1983), when $-2 \geq T > -22.9\ ^{0}C$, as described in (Petrich and Eicken, 2010)see SI for more details).

Data were described using nonparametric statistics as several variables (sea ice temperature, Hg_T, $MeHg_T$, and DOC) failed the test for normality ($p < 0.05$ for Shapiro-Wilk test). General statistical tests were performed in Sigmaplot v11.0 (Systat Software), while correlation and regression analyses, groupings and curve estimations were performed in SPSS® Statistics v20 (IBM).

2.3 Results

The profiles of Hg_T and $MeHg_T$ in bulk sea ice, along with temperature, salinity and other ancillary measurements, of MY ice cores from sites MY2 and MY3 are shown in Figure 2.2. A summary of the data is presented in Table 2.1. Unless otherwise specified, all the concentrations are reported as per liter of melted bulk sea ice.

2.3.1 Site MY2

The ice temperature and salinity were ~ -1°C and < 5, respectively, throughout most of the core (Figure 2.2d), indicating an advanced melt stage at the time of sampling. The reduced surface salinity and general linear increase in salinity with depth are characteristic of MY ice, resulting from flushing with snow and ice meltwater produced at the ice surface during the melt season (Eicken et al., 1995; Thomas et al., 1995; Tucker et al., 1999). The enriched $\delta^{18}O$ values in the top 30 cm of the core (Figure 2f) further suggest that the source of meltwater was more likely from the ablation of the bulk ice crystals themselves instead of from snow, which would have a much depleted $\delta^{18}O$ signal. Another interesting feature of this core is observed at depths between 210 and 280 cm, whereby $\delta^{18}O$ decreased sharply to -2.5 ‰ with a corresponding increase in salinity and temperature. This is indicative of a slush ice layer, likely related to ice rafting and/or ridging events which may have caused seawater to intrude into the core at this section (Toyota et al., 2007). The DOC concentrations were low, ranging from 15 – 110 μM, with the highest values in the mid- to bottom-sections of the core (Figure 2.2g). The Chl *a* concentrations were very low in the top 200 cm of the core (< 0.05 μg L^{-1}), but increased sharply to > 4 μg L^{-1} in the bottom 50 cm (Figure 2.2g). The DOC and Chl *a*

profiles are similar to those observed from a MY ice floe in Fram Strait (Thomas et al., 1995).

Along the 370 cm of the core, elevated Hg_T concentrations were found within the top 40 cm, which was composed of consolidated white ice, with the highest value of 9.87 ng L^{-1} occurring approximately 35 cm from the ice surface (Figure 2.2a). Within the mid-section (40 – 310 cm) of the core, Hg_T levels dropped to a mean value of 0.64 ng L^{-1}, then increased to a mean of 1.80 ng L^{-1} within the bottom 50 cm. The overall range of the Hg_T concentration (0.13 – 9.87 ng L^{-1}; median: 0.73 ng L^{-1}) was similar to that reported at Site MY1 collected from a similar region (0.22 – 4.37 ng L^{-1}, median: 0.56 ng L^{-1}) (Chaulk et al., 2011) (Table 2.1). $MeHg_T$ concentrations were below or near the MDL of 0.02 ng L^{-1} at ~30% of the depths, especially in the top 100 cm of the core (Figure 2.2b). Higher concentrations up to 0.11 ng L^{-1} were detected in a few sections in the mid- to bottom layers of the core. The ratio of $MeHg_T$ to Hg_T ranged from 0 up to 33% at a few depths in the middle section of the core. The slush ice layer at 210-280 cm had no noticeable effect on Hg_T or $MeHg_T$ concentrations.

2.3.2 Site MY3

Ice temperature (-1.5 to -0.5 ^{o}C) and salinity (<3) profiles were fairly homogeneous at site MY3, with temperature and salinity being maximum in the middle section and in bottom layer, respectively (Figure 2k). The low salinity values indicate that this ice experienced a considerable amount of snow meltwater flushing. Arctic summer sea ice melt has been shown to end around mid-August (Eicken et al., 2002; Petrich and Eicken, 2010). Hence, at the time of sampling (September 9) the MY ice at Site MY3 was likely experiencing an initial ice growth stage. $\delta^{18}O$, DOC, and Chl *a* were not

analyzed at this site. Flow cytometry results showed a gradual increase in total bacterial abundance along the ice core, ranging from 0.2×10^6 cells mL^{-1} in the top 25 cm to 0.45×10^6 cells mL^{-1} at the deepest layer. It is interesting to note that bacteria abundance assessed in this MY ice was similar to the values reported for the bottom 5 cm of FY ice (Nguyen and Maranger, 2011) and seawater (Alonso-Sáez et al., 2008) from the Amundsen Gulf. Bacteria in the top and bottom ice layers showed higher HNA content and FL1 intensity than those in the mid-section of the ice (Figure 2n).

The Hg_T concentration ranged from 0.68 – 12.20 ng L^{-1} at this site (median: 2.19 ng L^{-1}), with the highest concentration (12.20 ng L^{-1}) in the topmost 5 cm layer, decreasing sharply to < 5.01 ng L^{-1} (Figure 2.2b). Excluding the top and bottom layers, Hg_T concentrations were overall 2-3 times higher than at site MY2 (Table 1). Similarly, much higher $MeHg_T$ concentrations were measured throughout all the depths at site MY3, ranging from 0.15 to 0.53 ng L^{-1}, well above the MDL (Figure 2.2i, Table 1). The ratio of $MeHg_T$ to Hg_T ranged from 2.3% to 40.9%, with a clear enrichment in the bottom 100 cm of the ice, peaking at a depth of 195 cm below the ice-air interface (Figure 2.2j).

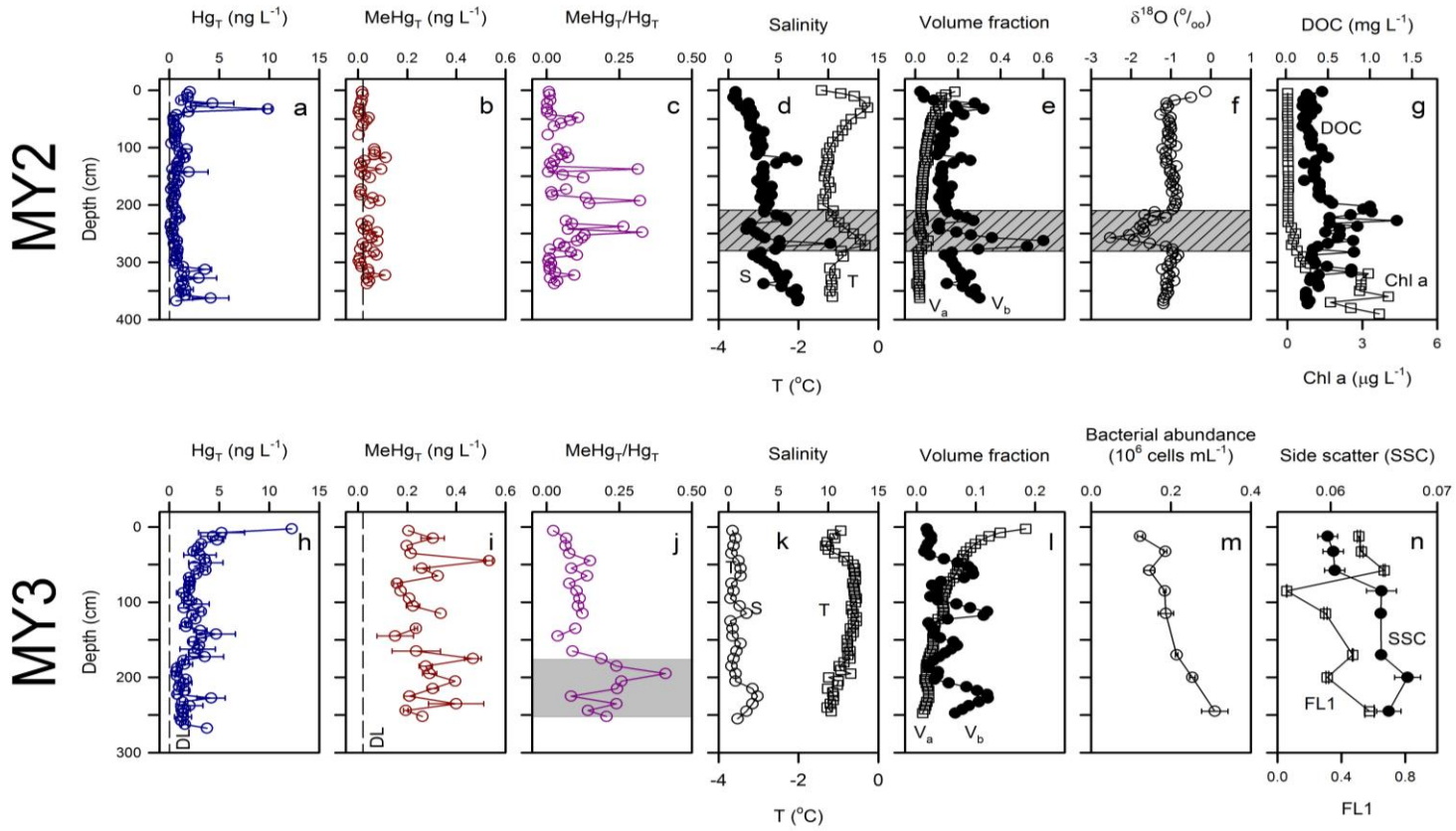

Figure 2.2: Profiles of total mercury (Hg_T), total methylated mercury ($MeHg_T$), the ratio of $MeHg_T/Hg_T$, bulk salinity (S), temperature (T), and calculated air and brine volume fractions (V_a and V_b, respectively) in multi-year ice at sites MY2 (a-g) and MY3 (h-n). Ancillary profiles of $\delta^{18}O$, dissolved organic carbon (DOC) and chlorophyll *a* (Chl *a*) are also shown for site MY2, and those of bacterial abundance, % high nucleic acid content (%HNA) and green fluorescence intensity (FL1) are shown for site MY3. Error bars in Panels a, b, h, and i represent the half range of two pseudo replicate measurements, and those in m and n are standard deviations. The hatched gray area in d, e, and f shows the depths where slush ice was present. The gray area in j shows the depths with high $MeHg_T/Hg_T$ ratios, suggesting the potential occurrence of in situ mercury methylation.

Table 2.1: Total mercury (Hg_T) and total methylated mercury ($MeHg_T$) concentrations in Arctic multiyear sea ice (N/A: no data)

Site ID	Location	Date sampled (UTC)	Surface conditions	Snow depth (cm)	Ice Thickness (cm)	Hg_T (ng L^{-1})			$MeHg_T$ (ng L^{-1})		
						Range	Median	Volume-weighted mean	Range	Median	Volume-weighted mean
MY1	72.65°N, 129.44°W	25-May-2008	Deformed surface; no melt ponds	23	350	0.22-4.37	0.56	0.81	N/A	N/A	N/A
MY2	74.50°N, 128.16°W	16-Aug-2011	Highly deformed surface; melt ponds	0 (melted into ice)	370	0.13-9.87	0.73	1.12	<0.02-0.11	0.03	0.04
MY3	74.75°N, 116.42°W	09-Sept-2013	Deformed surface; no melt ponds	~ 5	270	0.68-12.20	2.19	2.55	0.15-0.53	0.26	0.27

2.4 Discussion

2.4.1 Hg_T distribution in MY ice

Surface enrichment of Hg_T in the MY ice at sites MY2 and MY3 is in agreement with our earlier study at site MY1 collected from a similar region (Chaulk et al., 2011), as well as with what has been reported in FY ice (Chaulk et al., 2011; Cossa et al., 2011). This suggests that surface enrichment in Hg_T is a ubiquitous phenomenon in all sea ice types related to the formation and growth of sea ice. It has recently been shown that Hg_T distribution in FY ice is driven primarily by freeze rejection of seawater Hg in sea ice brine and by the dynamics of particulate matter (Chaulk et al., 2011). The same, however, may not hold true for MY ice. Different from FY ice, the evolution of MY ice through the melt season results in desalination and crystal retexturing of the frazil ice layer, and eventually the surface ice morphs into consolidated white ice with little to no brine pockets, yet particulate matter may be retained. As shown in Figure 2.2 e and l, the brine volume fractions in the surface layers of MY ice at sites MY2 and MY3 approached zero. Contrary to FY ice where brine concentration of Hg_T was found to correlate with brine salinity (Chaulk et al., 2011), such a relationship does not apply to any of the MY ice cores including MY1 (see Figure 2A.1 in Appendix 2).

Therefore, the surface peak of Hg_T cannot be accounted for by the freeze rejection of seawater; instead, particulate matter that is entrained in the ice may have played a more important role. Ice formed in the Beaufort Sea is known to entrap fine-grained particulates through scavenging of suspended sediment in the water column by the newly forming frazil ice ("suspension freezing") (Reimnitz et al., 1993b). Particulate matter tends to accumulate in the surface layer of the ice (Reimnitz et al., 1993a; Tucker et al., 1999) after several seasons of bottom freezing and surface melting (Reimnitz et al.,

1993a). Algae grown in melt ponds also add biogenic particulate matter to surface ice (Reimnitz et al., 1993a). Particulate matter in deteriorated surface ice ("old snow") can also be transported by wind to adjacent, previously clean ice floes (Reimnitz et al., 1993a). The surface layer of MY ice has been shown to contain particulate matter concentrations ranging from 0.5 to 900 mg L^{-1} in the Beaufort Gyre (Reimnitz et al., 1993a), and 0 to 2000 mg L^{-1} along a trans-Arctic Ocean transect from the Chukchi Sea to Barents Sea (Tucker et al., 1999). Unfortunately we did not collect particulate matter from our cores for Hg analysis. However, using a mean particulate matter concentration in Arctic MY ice of 250 mg L^{-1} (Tucker et al., 1999), the peak values of Hg_T in MY ice observed at sites MY2 and MY3 (~10 ng L^{-1}) can be fully accounted for if the Hg_T content in the particulate matter is ~40 ng g^{-1}, a value that agrees very well with the Hg_T content of surface sediment on the Arctic Ocean floor (34 – 116 ng g^{-1}) (Gobeil et al., 1999).

Elevated Hg_T concentrations were also observed in the bottom ice layer at both sites MY2 and MY3, though not nearly as high as the surface peak. This could be due to the presence of Hg-containing biogenic particles. The profile of Chl *a* as a function of depth at site MY2 (Figure 2.2g) revealed that autotrophic biomass (or relics of this biomass) is found within the bottom 110 cm of the ice, as concentrations of Chl *a* increased sharply at around 240 cm. Within the bottom 110 cm section of the ice, Chl *a* demonstrated a very strong, positive correlation with Hg_T ($r_s = 0.945$, $p < 0.0005$, n = 13), explaining in part the variability in bottom ice Hg_T concentrations. Marine algae take up Hg from their surroundings via absorption, adsorption and/or through metabolic activity (Burt et al., 2013a; Herrero et al., 2005; Mason et al., 1996). A recent study has

reported that the particulate-bound Hg (Hg_p) in the bottom sections of FY ice in the Beaufort Sea ranged from 4 to 22 ng g^{-1} (dw) during the spring ice algal bloom season (March-May) (Burt et al., 2013a). As the abundance of eukaryotic cells increased over the bloom, concentrations of Hg_P decreased, implying the occurrence of biodilution. Biodilution is not likely to occur to the same extent in MY ice due to much lower algal biomass when compared with the FY ice sampled in that study. The continual drainage of brine and meltwater enriched in Hg_p and subsequent sorption of Hg onto/into the small amount of algal cells or biological fluids could have contributed to the large Hg_T values in the bottom layer ice at site MY2.

2.4.2 Spatial variability of Hg_T in MY cores

It should be noted that the three MY ice cores were taken at different locations in different seasons. A Kruskal-Wallis test revealed that there was no statistical difference in Hg_T distribution between sites MY1 and MY2 ($p = 0.49$), but Hg_T concentrations at both sites were significantly lower than those at site MY3 ($p < 0.001$). The similarity in vertical profiles of Hg_T concentrations at sites MY1 and MY2, both from the eastern Beaufort Sea but in different seasons (MY1 in May 2008; MY2 in August 2011), suggests that the difference between the site in McClure Strait (MY3) and those in the Beaufort Sea (MY1 and MY2) is due to spatial variations.

To understand the higher Hg_T concentrations at site MY3, the history of the MY ice within the Beaufort Sea and McClure Strait must be reviewed. Studies of MY ice dynamics from 1968-2006 revealed that in most years there is a net export of MY ice from McClure Strait into the Beaufort Sea (Howell et al., 2008; Kwok, 2006a), and that the MY ice of McClure Strait is primarily imported through the Canadian Arctic

Archipelago (Sverdrup Basin) from the northern Queen Elizabeth Islands (QEI) region (Howell et al., 2009). While travelling through the Archipelago, floes can become land fast or grounded, which may trap sediment into the bulk sea ice matrix and lead to substantial sediment loadings (Kwok, 2006b; Pfirman et al., 1995). Seawater profiling at a site near MY3 indeed showed higher Hg_T, as well as $MeHg_T$, than other sites in the Beaufort Sea (Wang et al., 2012).

2.4.3 $MeHg_T$ distribution in MY ice

To our knowledge, this study represents the first measurements of $MeHg_T$ in MY ice (Figure 2.2b,i). While $MeHg_T$ concentrations in MY2 are generally low and often near the MDL, much higher $MeHg_T$ concentrations, up to 30 times MDL, are found in MY3 where Hg_T concentrations are also much higher overall. Indeed, at both sites, the ratio of $MeHg_T/Hg_T$ varied in a similar range (0 – 40%; Figure 2.2c,j). Of particular interest is the much higher $MeHg_T/Hg_T$ ratios in the mid- (Figure 2c) to bottom- (Figure 2.2j) section of the ice cores. This is most obvious at site MY3 where the bottom 70 cm of the core consistently had a $MeHg_T/Hg_T$ ratio above 20% (shaded layer in Figure 2.2j). In the only other study of MeHg in sea ice, albeit in Antarctic landfast FY ice, $MeHg_T$ was also found to peak in the bottom layer of the ice, though at lower concentrations (maximum 0.10 ng L^{-1}, $MeHg_T/Hg_T$ = 9.8%) (Cossa et al., 2011). The high $MeHg_T$ concentrations and the distinct depth distribution pattern of $MeHg_T/Hg_T$ in MY ice thus raise an important question on the origin of $MeHg_T$: is it transported from seawater and/or snow, or is it formed in situ within the ice?

Since the distribution pattern of $MeHg_T$ in MY ice does not follow that of Hg_T, it cannot be driven by the same process that drives the distribution of Hg_T (i.e., particle

dynamics as discussed above). Incorporation of seawater $MeHg_T$ into MY ice by freeze rejection is certainly possible, but does not appear to be sufficient to explain the high $MeHg_T$ levels observed in MY3 (see also Figure S1 in SI). Recent measurements of $MeHg_T$ in the Beaufort Sea have revealed that $MeHg_T$ in the water column peaks at a sub-surface, ~150 m below the sea surface, with or without the ice cover, and that $MeHg_T$ concentration in surface seawater is almost completely depleted due to demethylation or biological uptake (Wang et al., 2012). Similarly, while $MeHg_T$ has been measured in the Arctic snow cover (Lahoutifard et al., 2005; Larose et al., 2010; St Louis et al., 2007), percolation of snow meltwater cannot explain the presence of a MeHgT/Hg_T peak only in the mid- to bottom-layer of the MY ice. Concentrations of Hg_T in melt ponds on first-year land fast ice are as high as 14.9 ng L^{-1} (Chaulk, 2011) and the meltwater can percolate into underlying ice both vertically and horizontally as well as drain completely into the ocean surface via macroscopic flaws (Polashenski et al., 2012). However, $MeHg_T$, if present in meltwater, will photodegrade in surface waters (Monperrus et al., 2007; Seller et al., 1996), and thus is unlikely to percolate into lower ice sections through melt pond drainage process.

It is thus plausible that MeHg might be formed in situ in the mid- to bottom-layer of MY ice. Although there has been no report on known Hg methylators such as sulfate reducing bacteria and iron reducing bacteria in sea ice, anaerobic conditions have been reported in FY sea ice (Rysgaard and Glud, 2004; Rysgaard et al., 2008). There are also indications that certain aerobic bacteria might also be capable of methylating Hg (Larose et al., 2010). A recent study has shown that both the richness and diversity of the microbial community in the Arctic MY ice are higher than we previously thought

(Bowman et al., 2012). We did not attempt to identify Hg methylating bacteria in this study. However, a simple bacterial enumeration was carried out for the MY ice at site MY3. As shown in Figure 2.2 m and n, the bottom section of the ice core indeed has a much higher bacterial abundance with higher % HNA content and FL1 intensity. Although there is no consensus on the ecological and functional significance of HNA populations (Bouvier et al., 2007), the proportion of HNA content cells has been generally considered as the active fraction of the community (Lebaron et al., 2001). The higher FL1 intensity also indicates higher single-cell activity in the bottom section of the ice. The concomitant occurrence of the $MeHg_T/Hg_T$ peak and high bacterial activity in the bottom layer of MY ice suggests that in situ Hg methylation in MY ice is highly possible. Further studies are warranted to identify the presence of Hg methylators in MY ice, as well as in FY ice. If confirmed, the occurrence of Hg methylation could have major implications for Hg cycling in the Arctic Ocean.

2.4.4. Flux of Hg_T and $MeHg_T$ into the Arctic Ocean Upon Melt of MY ice

The data presented in Figure 2.2 and Table 2.1 allow us to make first-order estimates on the flux of Hg_T and $MeHg_T$ released into the Arctic Ocean system upon melting of MY ice. Note that our estimate is for the release of Hg_T through the complete melt of MY ice; we did not consider the efflux or removal of Hg_T from the ocean surface during subsequent FY ice formation and growth.

The volume of MY ice loss over a given melt season was estimated based on the Pan-Arctic Ice Ocean Modeling and Assimilation System (PIOMAS) (Schweiger et al., 2011; Zhang and Rothrock, 2003), which is a numerical model with inputs for sea ice concentrations, sea surface temperatures and other observations. The uncertainty of the

monthly averaged ice volume is estimated at ± 0.75×10^3 km^3 (Schweiger et al., 2011). Monthly mean ice volume data for September, the month during which sea ice extent is at a minimum and the icescape is assumed to be entirely composed of MY ice, are used. The difference in sea ice volume in September from one year to the next represents the net annual loss of MY ice to melt processes. This calculation yielded a mean annual loss in MY ice volume of 280 km^3 yr^{-1}. Taking the mean volume-weighted MY ice Hg_T and $MeHg_T$ concentrations of 1.48 ng L^{-1} and 0.15 ng L^{-1}, respectively, calculated as the mean of the volume-weighted mean bulk sea ice at each of the three sites (Table 2.1), this amounts to a Hg_T flux of 420 kg Hg yr^{-1} and a $MeHg_T$ flux of 42 kg Hg yr^{-1}into the Arctic Ocean upon MY ice melt. The magnitude of the Hg_T flux is in agreement with a recent estimate of an influx of ~ 48 kg yr^{-1} of Hg_p into the Arctic Ocean with the complete replacement of MY ice with FY ice in the Beaufort Sea (Burt et al., 2013a), which was based on Hg_T concentrations found within sea ice algae in the bottom 10 cm of thick FY ice. Although the Hg_T flux from MY ice melt is small compared with other Hg fluxes into the Arctic Ocean (Outridge et al., 2008), it could be an important factor in Hg biogeochemical cycles, especially with respect to MeHg. Since most of the Hg_T is particulate-bound, it tends to sink in the water column and aggregate at pycnoclines, where it may contribute to the sub-surface MeHg production in Arctic seawater (Wang et al., 2012). Furthermore, in situ methylation of Hg in MY ice, if confirmed, would represent a new MeHg source that was previously unaccounted for, and through uptake by sea ice algae and water column phytoplankton it could act as an effective pathway for MeHg bioaccumulation in the Arctic marine ecosystems.

2.5 Acknowledgement

This project was supported by funding from the ArcticNet (Network of Centers of Excellence of Canada), the Natural Sciences and Engineering Research Council of Canada, Canada Foundation for Innovation and the Northern Scientific Training Program of Indian and Northern Affairs Canada. We thank K. Warner, D. Isleifson, L. Candlish, M. Pind, J.S. Côte, M. Simard, C. Lovejoy and I. Laurion for their assistance in field sampling and laboratory analysis, and the entire crew of the CCGS Amundsen for their assistance with field logistics. The DOC Consensus Reference Materials were generously provided by D.A. Hansell and W. Chen (University of Miami, USA). We would like to dedicate this paper to the memory of our friends and colleagues Captain Marc Thibault of the Canadian Coast Guard, helicopter pilot Daniel Dubé of Transport Canada and Dr. Klaus Hochheim of the University of Manitoba, who died tragically in the McClure Strait following the crash of the CCGS Amundsen's helicopter on 9 September 2013, shortly after helping us collect the ice core at site MY3.

2.6 References

Alonso-Sáez L, Sanchez O, Gasol JM, Balague V, Pedrós-Alió C. Winter-to-summer changes in the composition and single-cell activity of near-surface Arctic prokaryotes. Environmental Microbiology 2008; 10: 2444-2454.

AMAP. AMAP Assessment 2009: Human Health in the Arctic. In: AMAP, editor, Oslo, 2009.

AMAP. AMAP Assessment 2011: Mercury in the Arctic In: AMAP, editor, Oslo, 2011.

Bouvier T, del Giorgio PA, Gasol JM. A comparative study of the cytometric characteristics of high and low-nucleic-acid bacterioplankton cells from different aquatic ecosystems. Environmental Microbiology 2007; 9: 2050-2066.

Bowman JS, Rasmussen S, Blom N, Deming JW, Rysgaard S, Sicheritz-Ponten T. Microbial community structure of Arctic multiyear sea ice and surface seawater by 454 sequencing of the 16S RNA gene. International Society for Microbial Ecology Journal. 2012; 6: 11-20.

Bowman KL, Hammerschmidt CR. Extraction of monomethylmercury from seawater for low-femtomolar determination. Limnology and Oceanography Methods 2011; 9: 121-128.

Burdige DJ, Homstead J. Fluxes of dissolved organic carbon from Chesapeake Bay sediments. Geochimica et Cosmochimica Acta 1994; 58: 3407-3424.

Burt A, Wang F, Pućko M, Mundy C-J, Gosselin M, Philippe B, et al. Mercury uptake within an ice algal community during the spring bloom in first-year Arctic sea ice. Journal of Geophysical Research: Oceans 2013; 118: doi:10.1002/jgrc.20380.

Chaulk A, Stern GA, Armstrong D, Barber DG, Wang F. Mercury distribution and transport across the ocean− sea-ice− atmosphere interface in the Arctic Ocean. Environmental Science & Technology 2011; 45: 1866-1872.

Comiso JC. Large decadal decline of the Arctic multiyear ice cover. Journal of Climate 2012; 25: 1176-1193.

Compeau G, Bartha R. Sulfate-reducing bacteria: principal methylators of mercury in anoxic estuarine sediment. Applied and Environmental Microbiology 1985; 50: 498-502.

Cossa D, Heimbürger L-E, Lannuzel D, Rintoul SR, Butler EC, Bowie AR, et al. Mercury in the Southern Ocean. Geochimica et Cosmochimica Acta 2011; 75: 4037-4052.

Cox GFN, Weeks WF. Equations for determining the gas and brine volumes in sea-ice samples. Journal of Glaciology 1983; 29: 306-316.

Eicken H, Krouse H, Kadko D, Perovich D. Tracer studies of pathways and rates of meltwater transport through Arctic summer sea ice. Journal of Geophysical Research 2002; 107: 8046.

Eicken H, Lensu M, Leppäranta M, Tucker WB, Gow AJ, Salmela O. Thickness, structure, and properties of level summer multiyear ice in the Eurasian sector of the Arctic Ocean. Journal of Geophysical Research 1995; 100(C11): 22697-22710.

Fitzgerald WF. Clean hands, dirty hands: Clair Patterson and the aquatic biogeochemistry of mercury. Clean Hands: Clair Patterson's Crusade Against Environmental Lead Contamination 1999: 119-137.

Fleming EJ, Mack EE, Green PG, Nelson DC. Mercury methylation from unexpected sources: molybdate-inhibited freshwater sediments and an iron-reducing bacterium. Applied and Environmental Microbiology 2006; 72: 457-464.
Gobeil C, Macdonald RW, Smith JN. Mercury profiles in sediments of the Arctic Ocean basins. Environmental Science & Technology 1999; 33: 4194-4198.
Herrero R, Lodeiro P, Rey-Castro C, Vilariño T, Sastre de Vicente ME. Removal of inorganic mercury from aqueous solutions by biomass of the marine macroalga *Cystoseira baccata*. Water Research 2005; 39: 3199-3210.
Howell SE, Duguay CR, Markus T. Sea ice conditions and melt season duration variability within the Canadian Arctic Archipelago: 1979-2008. Geophysical Research Letters 2009; 36: L10502
Howell SE, Tivy A, Yackel JJ, McCourt S. Multi-year sea-ice conditions in the western Canadian arctic archipelago region of the northwest passage: 1968-2006. Atmosphere Ocean 2008; 46: 229-242.
Kerin EJ, Gilmour CC, Roden E, Suzuki M, Coates J, Mason R. Mercury methylation by dissimilatory iron-reducing bacteria. Applied and Environmental Microbiology 2006; 72: 7919-7921.
Kwok R. Exchange of sea ice between the Arctic Ocean and the Canadian Arctic Archipelago. Geophysical Research Letters 2006; 33: L16501.
Lahoutifard N, Sparling M, Lean D. Total and methyl mercury patterns in Arctic snow during springtime at Resolute, Nunavut, Canada. Atmospheric Environment 2005; 39: 7597-7606.
Larose C, Dommergue A, De Angelis M, Cossa D, Averty B, Marusczak N, et al. Springtime changes in snow chemistry lead to new insights into mercury methylation in the Arctic. Geochimica et Cosmochimica Acta 2010; 74: 6263-6275.
Lebaron P, Servais P, Agogué H, Courties C, Joux F. Does the high nucleic acid content of individual bacterial cells allow us to discriminate between active cells and inactive cells in aquatic systems? Applied and Environmental Microbiology 2001; 67: 1775-1782.
Leppäranta M, Manninen T. The brine and gas content of sea ice with attention to low salinities and high temperatures. Finnish Institute of Marine Research Internal Report 1998.
Macdonald RW, Harner T, Fyfe J. Recent climate change in the Arctic and its impact on contaminant pathways and interpretation of temporal trend data. Science of the Total Environment 2005; 342: 5-86.
Maslanik J, Drobot S, Fowler C, Emery W, Barry R. On the Arctic climate paradox and the continuing role of atmospheric circulation in affecting sea ice conditions. Geophysical Research Letters 2007; 34: L03711.
Maslanik J, Stroeve J, Fowler C, Emery W. Distribution and trends in Arctic sea ice age through spring 2011. Geophysical Research Letters 2011; 38.
Mason RP, Reinfelder JR, Morel FMM. Uptake, toxicity, and trophic transfer of mercury in a coastal diatom. Environmental Science & Technology 1996; 30: 1835-1845.
Monperrus M, Tessier E, Amouroux D, Leynaert A, Huonnic P, Donard O. Mercury methylation, demethylation and reduction rates in coastal and marine surface waters of the Mediterranean Sea. Marine Chemistry 2007; 107: 49-63.

Nghiem S, Rigor I, Perovich D, Clemente-Colón P, Weatherly J, Neumann G. Rapid reduction of Arctic perennial sea ice. Geophysical Research Letters 2007; 34: L19504.
Nguyen D, Maranger R. Respiration and bacterial carbon dynamics in Arctic sea ice. Polar Biology 2011; 34: 1843-1855.
Outridge P, Macdonald R, Wang F, Stern G, Dastoor A. A mass balance inventory of mercury in the Arctic Ocean. Environmental Chemistry 2008; 5: 89-111.
Parker JL, Bloom NS. Preservation and storage techniques for low-level aqueous mercury speciation. Science of the Total Environment 2005; 337: 253-263.
Parsons TR, Maita Y, Lalli CM. Manual of chemical and biological methods for seawater analysis: Pergamon, 1984.
Petrich C, Eicken H. Growth, structure and properties of sea ice. In: Thomas DN, Dieckmann GS, eds. Sea Ice. 2nd Ed. Wiley-Blackwell, Chichester, UK, 2010, pp. 23-77.
Pfirman S, Eicken H, Bauch D, Weeks W. The potential transport of pollutants by Arctic sea ice. Science of the Total Environment 1995; 159: 129-146.
Pongratz R, Heumann KG. Production of methylated mercury, lead, and cadmium by marine bacteria as a significant natural source for atmospheric heavy metals in polar regions. Chemosphere 1999; 39: 89-102.
Reimnitz E, Barnes PW, Weber WS. Particulate matter in pack ice of the Beaufort Gyre. Journal of Glaciology 1993a; 39: 186-198.
Reimnitz E, Clayton J, Kempema E, Payne J, Weber W. Interaction of rising frazil with suspended particles: tank experiments with applications to nature. Cold Regions Science and Technology 1993b; 21: 117-135.
Rysgaard S, Glud RN. Anaerobic N 2 production in Arctic sea ice. Limnology and Oceanography 2004: 86-94.
Rysgaard S, Glud RN, Sejr MK, Blicher ME, Stahl HJ. Denitrification activity and oxygen dynamics in Arctic sea ice. Polar Biology 2008; 31: 527-537.
Seller P, Kelly C, Rudd J, MacHutchon A. Photodegradation of methylmercury in lakes. Nature 1996; 380: 694-697.
Schweiger A, Lindsay R, Zhang J, Steele M, Stern H, Kwok R. Uncertainty in modeled Arctic sea ice volume. Journal of Geophysical Research: Oceans (1978–2012) 2011; 116.
St Louis VL, Hintelmann H, Graydon JA, Kirk JL, Barker J, Dimock B, et al. Methylated mercury species in Canadian high arctic marine surface waters and snowpacks. Environmental Science & Technology 2007; 41: 6433-6441.
Stern GA, Macdonald RW, Outridge PM, Wilson S, Chételat J, Cole A, et al. How does climate change influence arctic mercury? Science of the Total Environment 2012; 414: 22-42.
Thomas DN, Lara RJ, Eicken H, Kattner G, Skoog A. Dissolved organic matter in Arctic multi-year sea ice during winter: major components and relationship to ice characteristics. Polar Biology 1995; 15: 477-483.
Thomas DN, Papadimitriou S, Michel C. Biogeochemistry of sea ice. In: Thomas DN, Dieckmann GS, eds. Sea Ice. 2nd Ed. Wiley-Blackwell, Chichester, UK, 2010, pp. 425-467.

Toyota T, Takatsuji S, Tateyama K, Naoki K, Ohshima KI. Properties of sea ice and overlying snow in the southern Sea of Okhotsk. Journal of Oceanography 2007; 63: 393-411.

Tucker III W, Perovich DK, Gow AJ, Weeks WF, Drinkwater MR. Physical properties of sea ice relevant to remote sensing. Geophysical Monograph Series. 1992, 62, pp. 9-28.

Tucker WB, Gow AJ, Meese DA, Bosworth HW, Reimnitz E. Physical characteristics of summer sea ice across the Arctic Ocean. Journal of Geophysical Research Oceans 1999; 104: 1489-1504.

USEPA. Method 1630: Methylmercury in Water by Distillation, Aqueous Ethylation, Purge and Trap, and Cold Vapour Atomic Fluorescence Spectrometry. Engineering and Analysis Division (4303), Washington, DC, 2001.

USEPA. Method 1631, Revision E: Mercury in Water by Oxidation, Purge & Trap and Cold Vapour Atomic Fluorescence Spectrometry. Office of Water 4303, 2002.

Wang F, Macdonald RW, Armstrong DA, Stern GA. Total and Methylated Mercury in the Beaufort Sea: The Role of Local and Recent Organic Remineralization. Environmental Science & Technology 2012; 46: 11821-11828.

Wang F, Macdonald RW, Stern GA, Outridge PM. When noise becomes the signal: Chemical contamination of aquatic ecosystems under a changing climate. Marine Pollution Bulletin 2010; 60: 1633-1635.

Whitehead RF, de Mora S, Demers S, Gosselin M, Monfort P, Mostajir B. Interactions of ultraviolet-B radiation, mixing, and biological activity on photobleaching of natural chromophoric dissolved organic matter: a mesocosm study. Limnology and Oceanography 2000; 45: 278-291.

Zhang J, Rothrock DA. Modeling global sea ice with a thickness and enthalpy distribution model in generalized curvilinear coordinates. Monthly Weather Review 2003; 131: 845-861.

Chapter 3: A Process-Based Investigation of Mercury Uptake and its Temporal Evolution within Experimental First-Year Sea Ice

3.0 Abstract

A mechanistic study examining the incorporation of mercury (Hg) into sea ice and the temporal evolution of its distribution within the ice column is presented. The study was conducted at the Sea-ice Environmental Research Facility (SERF), an outdoor mesocosm-scale facility at the University of Manitoba (Winnipeg, Manitoba, Canada). Particulate Hg concentrations ranged from 61 to 437 ng g^{-1} within newly formed, nilas ice (<10 cm thick), and represented on average ~73% of total Hg species, thus making it the dominant form of Hg within sea ice. The entrainment of particulate matter within frazil ice crystals during ice formation is hypothesized to be the major process of incorporation of Hg into the sea ice matrix, and the observed decrease in surficial particulate Hg concentrations over time revealed that particulate dynamics governs the distribution of Hg within the ice column rather than brine dynamics. Total Hg concentrations in experimental frost flowers (9.35-12.6 ng L^{-1}) were an order of magnitude lower than reported in Arctic samples during the atmospheric mercury depletion events, confirming the high Hg observed in Arctic frost flowers is due to scavenging of atmospheric gaseous reactive mercury. As the Arctic icescape shifts from a multiyear to a first-year sea regime, the increased overall volume of sea ice melt in the summer will increase the seasonal release of Hg into the Arctic Ocean system, while the increase in frazil ice formation at the onset of winter may remove more particulate Hg from Arctic Ocean surface waters.

3.1 Introduction

As concentrations of mercury (Hg) in some Arctic marine mammals continue to remain at toxicologically-concerning levels, the polar scientific community investigating Hg cycling has focused its attention on changes occurring within the various environmental compartments of the Arctic Ocean system (Dietz et al., 2013; Rigét et al., 2011; Stern et al., 2011; Wang et al., 2010a). The compartment that is arguably undergoing the most change is the icescape, as the sea ice environment is shifting from a multiyear (MY) to a first-year (FY) sea ice regime (Comiso, 2012; Maslanik et al., 2007b; Maslanik et al., 2011). Currently there are two published studies on Hg dynamics within sea ice, e.g., Chaulk et al. (2011) focused on the Arctic system while Cossa *et al.* (2011) concentrated on the Antarctic system.

Both of these studies reported elevated total mercury (Hg_T) concentrations, in certain cases an order of magnitude larger, in sea ice relative to the underlying seawater (Chaulk et al., 2011; Cossa et al., 2011). Another ubiquitous feature noted in ice cores from both geographical areas, regardless of the sampling season, was a surface enrichment in Hg_T concentrations. Due to its universal nature, this feature was suggested to result from ice formation and growth processes, mainly the incorporation of particulate matter and the freeze rejection of salts from the pure ice phase into dense brine inclusions within the surface ice layer (Chaulk et al., 2011; Cossa et al., 2011). Since Hg has a high affinity for particulate matter, it is hypothesized that Hg may become incorporated into the sea ice matrix through the consolidation of particulate-containing frazil ice crystals (Chaulk et al., 2011; Fitzgerald et al., 2007). Freeze rejection is another potential process of Hg incorporation into sea ice, and is defined as the expulsion of major and minor

dissolved ions out of the strict crystal lattice structure of the solid ice phase upon initial ice formation and growth, and the accumulation of these ions in brine pockets located within the interstices of ice crystals (Petrich and Eicken, 2010). To distinguish which of these processes has a stronger influence on Hg_T concentrations in ice, further review of the relationship between salinity and Hg_T concentrations in brine inclusions and measurement of particulate-bound Hg (Hg_P) in newly formed nilas sea ice (consolidated frazil ice, <1-10 cm thickness) is needed.

Since the distribution of Hg_T within FY ice mirrors that of bulk ice salinity, and a strong, statistically significant logarithmic relationship was discovered between Hg_T concentrations in brine and salinity, the distribution and transport of Hg_T within FY ice is thought to be governed mainly by brine dynamics (Chaulk et al., 2011; Cossa et al., 2011). However this logarithmic relationship with salinity was not as strong with Hg_T concentrations in bulk sea ice (Chaulk et al., 2011), therefore again suggesting the presence of particulate-bound Hg species within both the brine and pure ice phase of bulk sea ice. The transport and distribution of Hg_T within sea ice could be influenced more strongly by particulate dynamics (the movement of particulate matter in sea ice) in the ice rather than brine dynamics (the movement of liquid brine within sea ice), as suggested by recent work on Hg_T distribution in multiyear sea ice (Chapter 2, 2014). Thus the measurement of Hg_P, as well as dissolved Hg (Hg_D) and Hg_T within bulk sea ice is warranted.

The study of unique ice crystal types, including frost flowers, can provide insight into the incorporation of Hg into individual ice crystal matrices. When a large temperature gradient exists between seawater (-1.7°C) and the ambient air (< -20°C)

during calm, windless conditions over polar oceans, supersaturated water vapour condenses to form unique ice crystal formations, known as frost flowers, upon nodules (nucleation points) of newly-forming sea ice surfaces (Alvarez-Aviles et al., 2008; Andreas et al., 2002). Over the first few hours of growth, brine from the sea ice is wicked up into the frost flower through surface tension, enriching the bulk salinity of frost flowers relative to the underlying sea ice, and rapid kinetic growth from the vapour phase causes macroscopic crystal morphologies such as dendritic arms to form (Andreas et al., 2002). Due to their saline chemical composition, frost flowers may play a major role in polar tropospheric chemistry by contributing to salt aerosol and reactive bromine concentrations (Kaleschke et al., 2004; Rankin et al., 2000). Thus they are intricately linked to Hg cycling within polar systems, as reactive bromine oxidizes gaseous elemental mercury (GEM) to reactive gaseous mercury (RGM) during Atmospheric Mercury Depletion Events (AMDEs) (Brooks et al., 2006; Schroeder et al., 1998; Seigneur and Lohman, 2008). Only a handful of studies have measured Hg_T concentrations within natural frost flowers themselves, and found concentrations ranging from 45-180 ng L^{-1} (Douglas et al., 2005; Douglas et al., 2008). Young frost flowers (2 hrs old) with a low water vapour to brine ratio yielded lower Hg_T concentrations (~45 ng L^{-1}) (Douglas et al., 2008), yet as flowers grew through added water vapour condensation, Hg_T concentrations increased (150-180 ng L^{-1}, 4-8 h old) along with their water vapour to brine ratio (Douglas et al., 2005; Douglas et al., 2008). The successful growth of frost flowers at SERF (Isleifson et al., 2014) provided a rare opportunity to observe Hg dynamics within frost flowers in a different atmospheric setting.

Due to logistical constraints, only a few natural Arctic nilas ice samples have been analyzed for their Hg_T content, and the incorporation of Hg into the sea ice environment upon initial ice formation is still poorly understood. Continuous temporal monitoring of natural sea ice is challenging, as sampling moving pack ice at relatively the same location is not always possible. In order to overcome the constraints associated with natural sea ice sampling, the work presented was conducted at the Sea-ice Environmental Research Facility (SERF), an outdoor sea ice mesocosm at the University of Manitoba.

Here we present the first mechanistic study of Hg dynamics within new and growing experimental sea ice. Hg_T concentrations in various experimental sea ice types, including frost flowers and pancake ice, are reported. The first measurements of Hg_P and Hg_D within bulk sea ice are reported, and temporal monitoring campaigns for these various Hg species were conducted.

3.2 Materials and Methods

3.2.1 SERF Study Site

This study was conducted at the SERF at the University of Manitoba, Winnipeg, Canada, which upon construction in 2011 became the first dedicated, outdoor, mesocosm-scale sea ice experimental facility in Canada (Figure A3.1 in Appendices). During the onset of winter, the concrete pool, which has the dimensions of 18.3 m x 9.1 m x 2.6 m with an operating volume of ~380 m^3, is filled with experimental seawater (ESW). The ESW was formulated by dissolving large quantities of various rock salts into local groundwater to mimic the major ion composition, pH, and total alkalinity (TA) of natural seawater as closely as possible (Table A3.1, Appendices). The chemical composition also differed slightly between experiments in the same year due to snow input and manual adjustment of the water volume to avoid hydrostatic pressure build-up caused by ice growth (Hare et al., 2013b).

A total of three experiments were carried out at SERF over the winter months of 2012 and 2013. Details of each experiment, including duration, maximum and minimum air temperatures, maximum experimental sea ice (ESI) thickness and precipitation events are summarized in Table 3.1. Each experiment started from 100% open water by melting any ice left from the preceding experiment via circulating heated ethylene glycol through a hose at the bottom of the pool (Hare et al., 2013b). Different meteorological conditions created various types of sea ice over the course of these experiments (see Figure 3.1), including frost flowers, nilas ice (<10 cm thickness) and young ice (≥ 10 cm). The thickness classification of nilas and young ice is based on Petrich et al. (2010).

Table 3.1: The physical conditions at SERF during the 3 experiments performed.

Experiment	SERF 1.2	SERF 2.1	SERF 2.2
Dates of Experiment	Feb.10 – 12th, 2012	Jan.12 – 18th, 2013	Feb.18 – 20th, 2013
Air Temperature Max (ºC)	- 6.6	- 4.8	-14.1
Air Temperature Min (ºC)	- 21.9	- 23.6	- 26.6
Maximum Ice Thickness (cm)	5.0	14.2	9.5
Precipitation Events	None	Jan 14: Light snow, < 1 cm Jan 18: Snowfall, ~ 3 cm	None
Ice types Grown	Frost Flowers	Nilas ice, Young ice	Nilas ice

Figure 3.1: Various types of ESI grown at SERF and their thickness classifications

3.2.2 Sampling

ESI and ESW samples were collected for the analysis of Hg_T throughout all three experiments. During Exp. 2.2 and 2.1 (water only), samples were also taken to analyze dissolved Hg (Hg_D) and particulate Hg (Hg_P). Mercury sampling strictly followed the clean-hands – dirty-hands sampling protocols (Fitzgerald, 1999a). Prior to sampling, all the Hg sampling equipment and bottles were precleaned, tested for acceptable Hg background levels (<0.1 ng L^{-1}) in the Ultra-Clean Trace Elements Laboratory (UCTEL) at the University of Manitoba, and doubly bagged separately in new Ziploc® bags. Ultrapure Milli-Q Element water (Millipore) produced at UCTEL was used as laboratory water throughout the study.

All ESI and ESW samples were collected from the centre of the pond (to avoid pool edge effects and metal-containing instrumentation) off the side of a moveable bridge. Nilas ESI was collected using ice razorsaws (Japan) while young ice was collected using a Mark II Kovacs core barrel (i.d. = 9 cm). Frost flowers were gently scraped off of the ice surface using a pre-cleaned ceramic blade knife (Kyocera). Triplicate ice and water samples (3 separate samples) were collected for Hg_T analysis and Hg_D analyses, while one single large ice sample and water sample were collected for Hg_p analysis. All ice and ice crystal samples were placed into new Ziploc and Whirlpak bags and stored in a dedicated chest freezer at -20°C prior to processing. As soon as ESI samples were taken, grab samples of the newly-exposed surface ESW were collected for Hg analysis into new 50-mL polypropylene Falcon tubes (BD; previously tested and deemed to have low background Hg levels) (Chapter 2, 2014; Chaulk et al., 2011).

All ESI samples were processed within 48 h after collection. Young ESI cores were cut into 5 cm sections for Hg analysis and split in half to create pseudo-replicates in a -20°C cold lab at the University of Manitoba. To avoid cross-contamination, the outer 0.5-1 cm layer of the ice that came into contact with the saw and core barrel was scraped off by a pre-cleaned ceramic blade knife. Once scraped, ice samples were placed into new Ziploc® bags and melted at 21°C in UCTEL. Frost flower and pancake ice samples did not require scraping, and were melted immediately in UCTEL. Melted ice samples were then transferred into new polypropylene 50-mL Falcon tubes for analysis.

To create an ESW depth profile of Hg_T and Hg_D during Experiment 2.1, ESW samples were collected at 50 cm depth intervals into precleaned 250 mL Teflon bottles using a precleaned Teflon-lined Niskin bottle.

All melted ESI and ESW samples dedicated for Hg_D analysis were filtered using Nalgene® Rapid-Flow® sterile disposable filter units with cellulose nitrate membranes (50 mm, 0.45 µm) and the filtrate was transferred into new polypropylene 50-mL Falcon tubes for analysis. All melted ESI and ESW samples dedicated for Hg_P analysis were measured (volumes ranged from 200-100 mL) then filtered through pre-weighed PALL® hydrophilic polypropylene membrane filters (47 mm, 0.2 µm) with a blank filter attached in tandem (below) the sample filter.

Immediately after sampling, all Hg_T and Hg_D samples were spiked with 250 µL of ultrapure HCl (JT Baker) and 250 µL of BrCl (prepared from KBr and $KBrO_3$, JT Baker, in ultrapure HCl) prior to analysis. Replicate ESI and ESW samples were also taken for the analysis of salinity and major ions.

3.2.3 Analyses

All Hg_T and Hg_D samples were analyzed within 48 hr of sampling in UCTEL by cold vapour atomic fluorescence spectroscopy (CVAFS) on a Tekran 2600 Hg_T analyzer in accordance with U.S. EPA Method 1631 (USEPA, 2002). Certified reference material (CRM) BCR®-579 coastal seawater ($[Hg_T]$ = 1.85 ± 0.5 ng kg^{-1}) was employed as a quality control measure and recovery varied from 96 % to 115 %. The method detection limit (MDL) was 0.19 ng L^{-1}, and Hg_T concentrations in all field blanks (open and pour blanks) were always < 25% of sample concentrations (field blank corrections were not applied to the data). Several blanks from this study were higher than reported for previous studies conducted in this lab (Chaulk et al., 2011), and at times were as high as 1 ng L^{-1}. Since the SERF study has a process-based investigation, and the distinction between experimental and natural sea ice was continually made throughout this work, these slightly higher blank values did not affect the results and overall conclusions of this work. Note that the Hg_T data reported was unfiltered, and represents all mercury species per litre of melted ESI and ESW, while Hg_D represents dissolved and colloidal Hg species under 0.45 µm in size in these media.

Analysis of Hg_P was performed on a Teledyne Leeman Hydra II_c at the University of Manitoba. The whole filter containing the particulate sample was decomposed at 800^oC and catalyzed at 600°C, followed by cold vapour atomic absorption spectroscopy in accordance with U.S. EPA Method 7473. The MDL was 0.33 ng g^{-1}, which is based on instrumental filter blanks with new, clean combusted filters. Ongoing instrumental performance was checked using CRM NIST-2976 ($[Hg_P]$ = 61 ± 3.6 ng g^{-1}), and analytical accuracy ranged from 93-103%. Hg_P in the method filter blanks (filters set up

in tandem with sample filters) remained below 2 ng g^{-1}, which was not subtracted from the final particulate concentration.

Major ions (Cl^-, SO_4^{2-}, Br^-, Na^+, K^+, Ca^{2+}, Mg^{2+}) were analyzed by inductively coupled plasma (ICP) optical emission spectroscopy (OES) at the Manitoba Chemical Analysis Laboratory (MCAL, University of Manitoba) or by ICP-mass spectrometry (MS) at ALS Environmental (Winnipeg). Total alkalinity was measured by potentiometric titration (Geilfus et al., 2013), and pH was measured by both potentiometric and spectroscopic methods (Hare et al., 2013b). Salinity of the ESI and ESW samples was measured using a sensION5 conductivity meter (Hach), and is reported in Practical Salinity Units (PSU). Temperatures of ESI and ESW temperatures were recorded by automated type-T thermocouple arrays fixed at ~5 cm intervals along the entire depth of the pool (for Experiment 2.2, temperatures were manually measured using a Model 400 thermometer, Traceable Control Company), and ambient air temperatures were recorded by an Environment Canada meteorological station located approximately 10 km north of SERF (Environment Canada, 2014).

Data were described using nonparametric statistics as several variables (Hg_T concentrations in nilas ice, ice surface scrapings, etc) failed the test for normality ($p < 0.05$ for Shapiro-Wilk test) and no data points were excluded from statistical analyses. General statistical tests were performed in Sigmaplot v11.0 (2008 Systat Software Inc), while correlation and grouping analyses were performed in IBM® SPSS® Statistics v20 (2011). Note that adjusted significance values which apply the Bonferroni correction are reported for post-hoc pairwise comparisons (Kruskal-Wallis analysis of variance) (Zar, 1984).

3.3 Results

3.3.1 Overall ranges of Hg_T in ESW and ESI

The Hg_T concentrations in ESW and various types of ESI are summarized in Figure 3.2. Note that Hg_T concentrations in ESW varied greatly and values are over an order of magnitude higher (~2-12 ng L^{-1}) than reported values for under ice surface waters within natural polar systems (~0.2-0.6 ng L^{-1}) (Chaulk et al., 2011). This difference is a function of the Hg-laden salts and local groundwater used to prepare the ESW, as well as the added urban Hg emission sources. Initial analyses of total Hg (Hg_T) concentrations in the local groundwater revealed a mean of 3.02 ± 0.15 ng L^{-1} (n = 4), while the solution of ESW, including all dissolved rock salts, had a concentration of 11.88 ng L^{-1}. Since this study explores the mechanisms behind Hg incorporation into sea ice and distribution within the ice column without attempting to compare concentrations to natural systems, these higher ESW concentrations are not expected to affect the behaviour of Hg within the system and thus the findings of this work.

Interestingly, these high ESW concentrations did not seem to impact the concentrations of Hg being uptaken into newly forming ESI. Reported values for Hg_T concentrations in natural first-year sea ice range from 0.4-6 ng L^{-1} (Chaulk et al., 2011; Cossa et al., 2011; Douglas et al., 2008), which encompass the Hg_T medians for nearly all ESI types measured at SERF (excluding frost flowers).

The highest Hg_T concentrations were found in bulk frost flowers (median = 10.8 ng L^{-1}), while the lowest were found in nilas ESI (median = 2.3 ng L^{-1}) and the bottom 5 cm of young ESI (2012: median = 2.1 ng L^{-1}; 2013: median = 2.4 ng L^{-1}).

Non-parametric analysis of variance (Kruskal-Wallis test) demonstrated significant differences between the medians of all ice types from both 2012 and 2013 ($p <$

0.005, n = 156. Pairwise comparisons revealed that the medians of the following pairs were statistically different: Nilas ESI 2013 – Under ice ESW 2013, (adj. $p < 0.005$, n = 50); Young ESI Surface 2013 – Young ESI Bottom 2013 (adj. $p < 0.02$, n = 11); and Young ESI Surface 2013 – Under ice ESW 2013 (adj. $p < 0.05$, n = 13). This demonstrates that Hg_T concentrations within the ice, both nilas and young ice, were statistically different than the underlying water surface, and surface young ice Hg_T concentrations are statistically significantly different than bottom young ice. Overall no statistical difference was seen in the medians of separate sample mediums (Under ice ESW and Nilas ESI) from the two years of study, yet this is most likely a function of the small sampling size for 2012 data (n = 4).

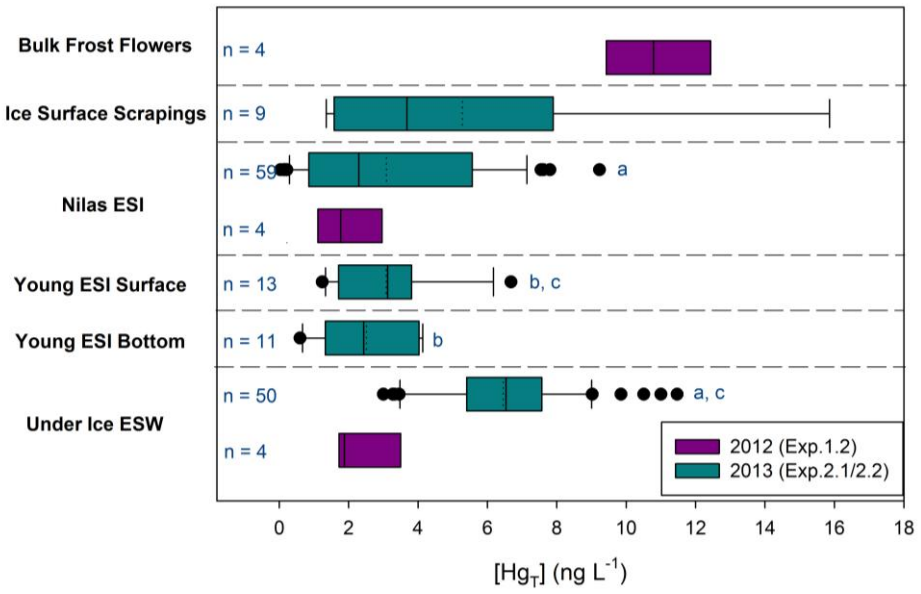

Figure 3.2: Boxplots of Hg_T concentrations in various ESI types and under ice ESW over experiments 1.2 (2012) and 2.1, 2.2 (2013). Exterior left and right whisker bars represent the 10th and 90th percentiles respectively, while left and right exterior box bars represent the 25th and 75th percentiles respectively. Interior solid and dotted lines represent the median and mean respectively for each group, and outer black dots represent outliers. Groups with matching letter designations have significantly different medians (adj. $p < 0.05$).

3.3.2 Exp 1.2: Hg_T during a Frost Flower Event

A major frost flower event occurred at the beginning of Exp. 1.2 when the ambient air temperatures dropped to -25°C. The event lasted for ~60 h, and evolved through four stages based on distinct physical ice characteristics detected by C-band polarimetric scatterometry data (Isleifson et al., 2014): initial formation, surface brine expulsion, growth, and decimation (Table 3.2). The Hg_T concentrations of bulk frost flower samples, nilas ESI and the underlying ESW are described in Figure 3.3D, along with temperature, ice thickness and salinity (A-C respectively).

Table 3.2: Evolution of the frost flower event during Exp 1.2 at SERF and associated physical characteristics (Isleifson et al., 2014).

Time (h)	Frost Flower Development Stage	Characteristics	Frost Flower Coverage
0.0	(I) Initial Formation	Thin ice skim (~1mm thick) formed across surface initially, low wind speed	sparse
3.25		Ice at 5mm thick and flowers at 5mm height, low water vapour:brine ratio	80%
4.5	(II) Surface Brine Expulsion	Surface ice temperature drop of 3°C initiated brine expulsion	95%
6.0		Surface ice salinity tripled (7.53-23.69), ice surface appeared dark and wet	95%
9.5	(III) Frost Flower Growth	Frost flowers whiter in appearance, demonstrate a bulk salinity peak at 22h (~51)	95%
30.5		By end of stage, frost flowers at 1.5 cm height, show similar salinities to ice surface (28 and 27, respectively), slightly higher water vapour:brine ratio	95%
58.0	(IV) Decimation	Decay/melt of frost flowers due to increased air temperatures, brine-wetted deformed ice crystals noted across ice surface	50%

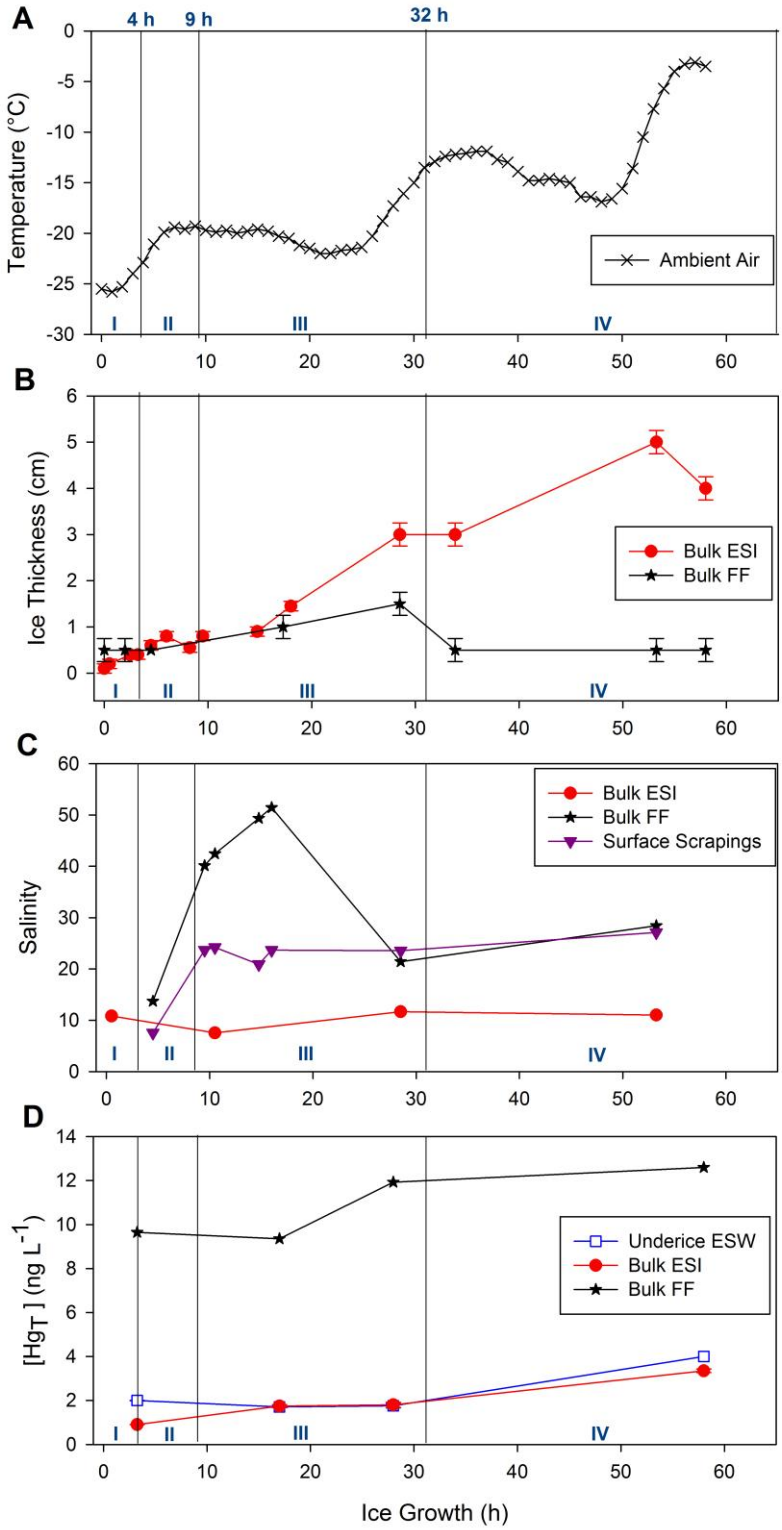

Figure 3.3: Time series of Hg_T concentrations in bulk frost flowers (FF), ESI and underlying ESW grown at SERF during experiment 1.2 (D), and associated temperature (A), thickness (B; Isleifson et al., 2014) and salinity (C) measurements.

During the surface brine expulsion phase of frost flower development (phase II), salinity of the bulk frost flowers and the ice surface tripled from 13.7 to 40.1 and from 7.5 to 23.7, respectively, leading to a low water vapour to brine ratio prior to the kinetic growth of frost flowers from the vapour phase, as the ice crystals at this point are mostly composed of brine. As frost flowers grew in height to 1.5 cm (phase III) by scavenging water vapour from the atmosphere, the water vapour to brine ratio increased and their salinity dropped to 21. During decimation (phase IV), flower heights and coverage decreased considerably to 0.5 cm and 50%, respectively.

The frost flowers, ESI, and ESW were only sampled four times during the flowering event: once in phase I, twice in phase III and once in phase IV. Based on these four samples, Hg_T concentrations in the bulk experimental frost flowers ranged from 9.4-12.6 ng L^{-1}. The low temporal sampling density prevented us from detecting any temporal trend or relation of Hg_T to frost flower physical characteristics, though there appeared to be a slight increase during Phase III. Nilas ESI concentrations during the frost flower event ranged from 0.9-3.4 ng L^{-1} (median: 1.77 ng L^{-1}), while Under ice ESW Hg_T concentrations ranged from 2-4 ng L^{-1} (median: 1.88 ng L^{-1}).

3.3.3 Exp. 2.1: Time Series of Hg_T Concentrations in Nilas & Young ESI and Underlying ESW

During Exp 2.1, Hg_T concentrations were measured concurrently in newly formed nilas ice and underlying surface waters. The temporal evolution of these Hg_T concentrations is shown in Figure 3.4D, alongside ancillary physical variables including temperature, ice thickness, and salinity for both the experimental sea ice and seawater

(Figures 3.4A-C). Note that time 0 h represents newly formed ESI, sampled just after frazil ice consolidation created a continuous ice surface.

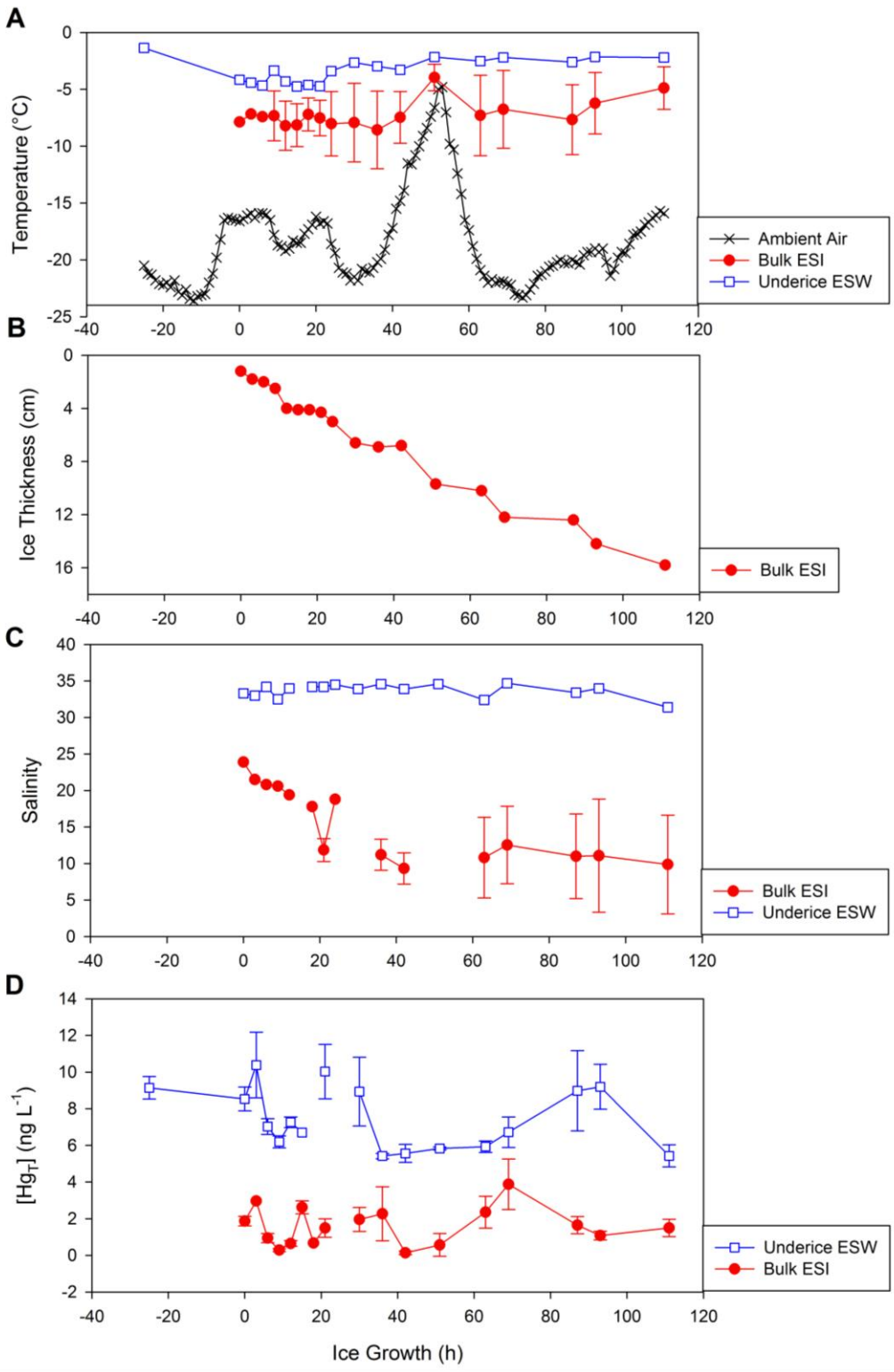

Figure 3.4: Time-series of Hg_T concentrations in nilas ESI and Under ice ESW grown at SERF during experiment 2.1 (D), along with associated temperature (A), ice thickness (B) and salinity (C) measurements.

The salinity of Under ice ESW remained fairly consistent over the course of the experiment at ~34 and ESW temperature increased from -4 to -2°C as increasing ice thickness insulated the underlying ESW (Figure 3.4A). The decrease in salinity from ~24 to 10 over time for bulk ESI is expected due to the processes of freeze rejection of major ions and brine expulsion (Petrich and Eicken, 2010), and the sea ice salinity time series reported here is very similar to a recent time series of in situ salinity of growing natural sea ice in Adventfjord, Svalbard measured via electrical impedance (Notz et al., 2005). Growing sea ice can have a sharp temperature gradient, with colder ice found at the ice-atmosphere interface and warmer ice found at the ocean-ice interface (Petrich and Eicken, 2010), which explains the large variability in mean ESI temperatures for each sampling time.

Initial ESI Hg_T concentrations, measured almost immediately after frazil ice consolidation in only 1.2 cm of thin nilas ice, were 1.87 ± 0.26 ng L^{-1}. At 3 hr into ice growth, when ice thickness reached 1.8 cm, ESI Hg_T concentrations had increased to 2.97 ng L^{-1}, then dropped to below 2 ng L^{-1} over the remainder of the experiment, with the exception of a few peaks (e.g. 3.88 ng L^{-1} at ~69 hr ice growth and 12.2 cm ice thickness). Over the entire time series, ESI Hg_T concentrations were quite variable (mean: 1.58 ± 1.02 ng L^{-1}), as were ESW Hg_T concentrations (mean: 7.49 ± 1.70 ng L^{-1}). Interestingly, the temporal trend in Hg_T ESW concentrations appears to correlate with the temporal trend demonstrated by ESI Hg_T concentrations until the ice was over 12 cm in thickness (~ 87 hr), where the trends appeared to diverge.

On Day 4 the ice had grown to 12.4 cm thick. From there on ESI cores were sectioned (2-5 cm sections) to produce vertical distribution profiles of Hg_T concentrations

within the ice matrix. Profiles of Hg_T concentrations, temperature, and salinity of young ESI taken from SERF during 87-111 hrs of experiment 2.1 are shown in Figure 3.5.

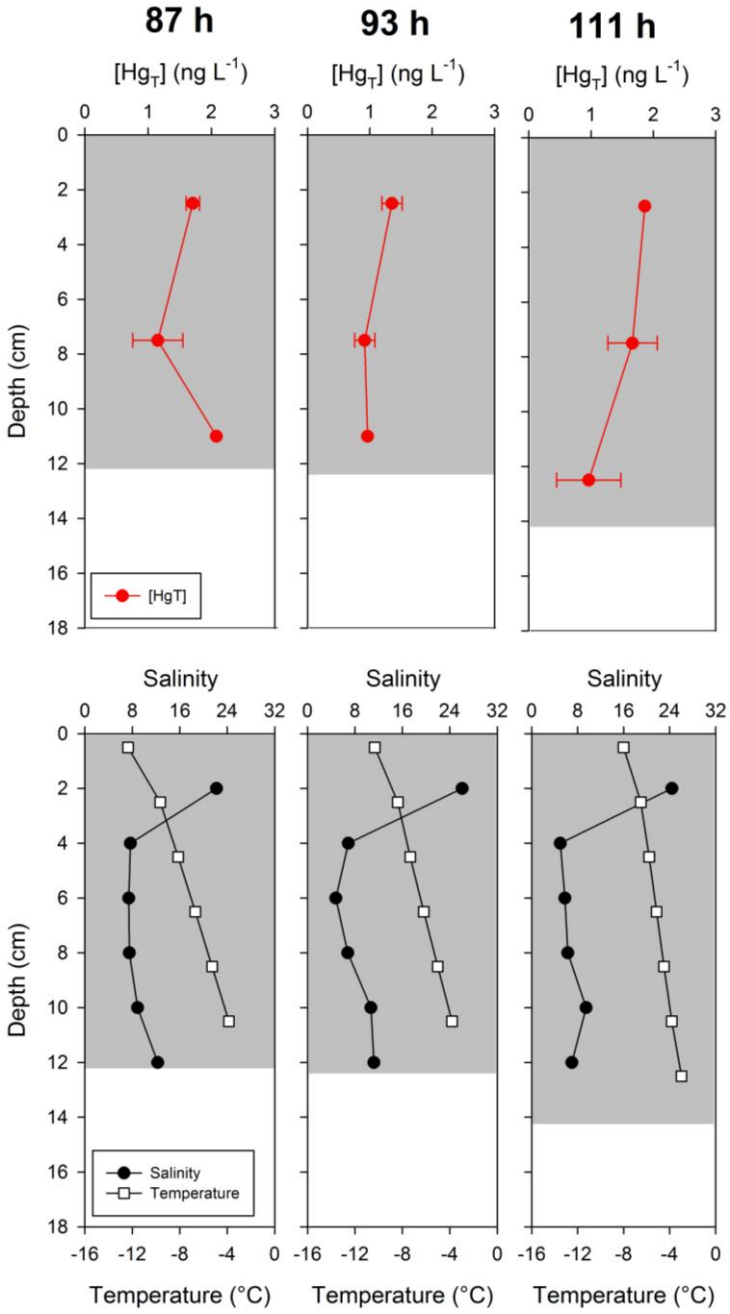

Figure 3.5:Profiles of Hg_T concentrations, temperature and salinity within ESI sampled at 87, 93 and 111 hr after ice formation in SERF during experiment 2.1 (January 2013). The gray shaded area in each profile represents ice thickness (in cm), and error bars on Hg_T measurements represent the half-range of pseudo-replicate samples.

Linearly increasing temperature gradients with depth in the ice are shown in Figure 3.5, and all salinity profiles demonstrated the characteristic C-shape expected for growing sea ice (Petrich and Eicken, 2010), with high surface salinities ranging from 22-26. Nearly all cores demonstrated surface enrichment with concentrations >1.35 ng L^{-1}, yet the core taken at 87 hr showed a peak in Hg_T concentration to 2.08 ng L^{-1} within the bottom 5 cm of ice. Interior and/or bottom ice Hg_T concentrations decreased to a minimum of 0.92 ng L^{-1} in all cores.

3.3.4: Exp. 2.2: Time-Series of Hg Speciation in Nilas ESI and Underlying ESW

During Exp 2.2, Hg_P, Hg_D and Hg_T concentrations were measured in both newly formed nilas ice and underlying surface waters alongside ancillary variables. Rather than calculating Hg_P from the difference between total and dissolved mercury species, we were able to measure Hg_P in particulate matter accumulated on filters via a direct Hg analyzer and report concentrations in ng g^{-1}. Profiles of Hg_P, Hg_D and Hg_T concentrations and corresponding ancillary variables measured in the experimental ice and underlying water matrices over the 2 day sampling event are shown in Figure 3.6 (A and B respectively).

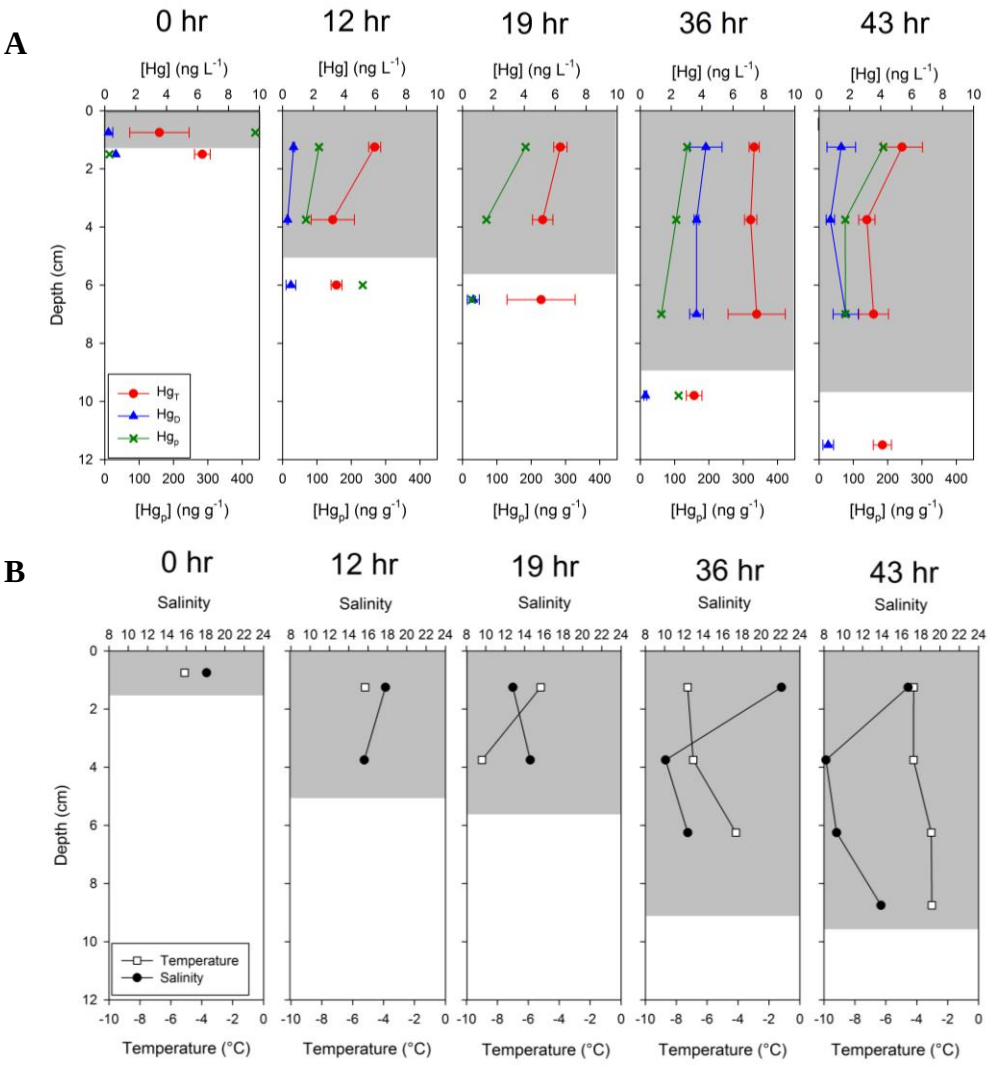

Figure 3.6: Profiles of Hg_p, Hg_D and Hg_T concentrations (A) and corresponding temperature and salinity measurements (B) in nilas ESI and underlying ESW matrices, measured during experiment 2.2 at SERF. The gray shaded area in each profile represents ice thickness (in cm), and error bars on Hg measurements represents a standard deviation of triplicate measurements performed on 3 separate ice cores for each Hg species.

Overall ESI Hg_T concentrations were nearly 4-fold higher (median = 5.83 ng L^{-1}) than reported in nilas ESI in previous SERF experiments (median = 1.41, excluded experiment 2.2 data) yet are not unreasonable. One plausible explanation for these uncharacteristically high ESI Hg_T concentrations is increased entrainment of particles

into the sea ice matrix due to quick ice formation at the start of the experiment. Ambient air temperatures dropped over 15°C on February 18th, 2013, from -5.6°C (0:00) to -21.3°C (21:00) (Environment Canada, 2014), compared to a drop of only 7°C on January 13th, 2013, the date of ice growth during experiment 2.1 at SERF. Ice formed in colder conditions contains less brine and more solid ice fraction, and the newly formed nilas ESI measured showed lower salinity values than in experiment 2.1, yet surface salinities increased over time and the salinity profile developed into the characteristic C-shape as temperatures warmed (ambient air temperatures reached -13.5°C on February 20th, 2013) (Environment Canada, 2014) and brine fractions increased. Concentrations of ESI Hg_D ranged from 0.21 to 2.49 ng L^{-1} (median = 0.67 ng L^{-1}); however ESI sampled at 36 hrs showed concentrations ranging from 3.05 to 4.95 ng L^{-1}, which may be an effect of contamination during the filtration process. All Hg_D concentrations were lower than Hg_T concentrations, and in general they demonstrated a similar vertical distribution pattern to that of Hg_T, with the ice surface showing higher concentrations than the interior region. Concentrations of Hg_P in newly formed nilas ESI were high at 438 ng g^{-1}, and were enriched within the top 2.5 cm of the ice (median = 184 ng g^{-1}) relative to the interior and bottom ice (median = 73.3 ng g^{-1}). ESI Hg_P concentrations demonstrated the most notable change over time, as surface concentrations generally decreased over time from 438 ng g^{-1} to 187 ng g^{-1}. Concentrations of Hg_T and Hg_D within the underlying ESW remained generally constant at 4.50 ± 1.21 and 0.58 ± 0.15 ng L^{-1} (mean ± standard deviation), while Hg_P ESW concentrations were extremely variable at 96.7 ± 100.8 ng g^{-1}, yet usually ESI is enriched in Hg_P relative to the underlying ESW.

3.4 Discussion

Previous studies on Hg dynamics within sea ice and ice crystals have postulated that particulate-bound Hg is present within the sea ice matrix, and may be the dominant Hg species (Chapter 2, 2014; Chaulk et al., 2011). Surface enrichment in Hg_T concentrations in both first-year and multiyear sea ice led to the hypothesis that both the incorporation of Hg-bound particulate matter and the freeze rejection processes that occur during sea ice formation and growth are responsible for this ubiquitous feature (Chaulk et al., 2011). The inverse relationship between brine volume and Hg_T concentrations within the surface of multiyear ice suggested that particulate dynamics control the vertical distribution of Hg_T within sea ice over brine dynamics (Chapter 2, 2014). These hypotheses were further tested at SERF through a variety of time series experiments, which measured various Hg species in new and growing sea ice, and are discussed below.

3.4.1 Hg Speciation in ESI: Is Hg_P the Dominant Hg Species in Sea Ice?

Prior to the direct measurement of Hg_p in sea ice, Hg_T and Hg_D concentrations at various depths within the ESW column were measured during Exp. 2.1 to get an estimate of the SERF ESW Hg_P concentrations through difference (as operationally defined), as shown in Figure A3.2 in the Appendices. The mean difference (Hg_T-Hg_D) was found to be 5.07 ± 0.32 ng L^{-1}, thus Hg_D only represented on average ~26% of Hg_T in ESW, suggesting that a substantial portion of Hg is in the particulate-bound form. Variable Hg_T concentrations in ESW again support the hypothesis that Hg_P is dominating Hg speciation in the marine system, as the discrete grab sampling methods employed would cause the amount of particulate matter to deviate considerably between samples.

In Exp. 2.2, Hg_P concentrations were measured in ESI and underice ESW, and the temporal evolution of the vertical distribution of Hg_P, Hg_T and Hg_D concentrations was measured. As hypothesized, Hg_p is present in sea ice at considerable concentrations, up to 438 ng g^{-1}, upon initial ice formation (Figure 3.6). The high ice surface Hg_p concentrations and similarity between the Hg_T and Hg_P vertical distribution profiles suggest that Hg_P is the dominant Hg species within sea ice.

This finding has major implications on Hg dynamics within sea ice and the Arctic system as a whole, as the partitioning of Hg between dissolved and solid phases influences the mobility and bioavailability of Hg species within the ice matrix, which ultimately controls the fate and biological uptake of Hg within the Arctic Ocean system (Liu, 2012). Aquatic particulate Hg content is known to be positively correlated with the organic content within particles (Coquery et al., 1995), as organic macromolecules such as polysaccharides contain reactive or ionizable surface groups such as S-, O- and N-moieties that Hg^{2+} will readily adsorb to (Liu, 2012). It is therefore hypothesized that either organic or inorganic forms of Hg(II) can be adsorbed to the cellular membranes of sea ice algae, or entrained within the associated biological substances, which will decrease their bioavailability. From an analytical standpoint, the dominance of Hg_P in sea ice may allow for particulate concentrations within ice to act as a proxy for Hg_P concentrations, although further study on the Hg content in sea ice particles is required.

3.4.2 Hg dynamics within sea ice: Are Hg concentrations controlled by freeze rejection processes or particulate distribution processes?

In both time series datasets considerable Hg concentrations were found in thin, newly formed ESI, suggesting that Hg is incorporated into the sea ice matrix upon initial frazil ice consolidation (nilas ice formation). To test the hypothesis that the freeze rejection

process is responsible for Hg_T concentrations in bulk sea ice, the relationship between brine volume, salinity and Hg_T concentrations was explored in young ice over 12 cm in length (grown during experiment 2.1). Bulk sea ice Hg_T concentrations were normalized to the brine volume fraction (V_b) and plotted against the brine salinity, as described in Chaulk et al (2011). Note that brine volume was calculated as described in Appendices A2.2; however Va, which represents the volume of air within the sea ice matrix, can be neglected in Eq (1) due to its low values in first-year sea ice (Cox and Weeks, 1983; Petrich and Eicken, 2010).

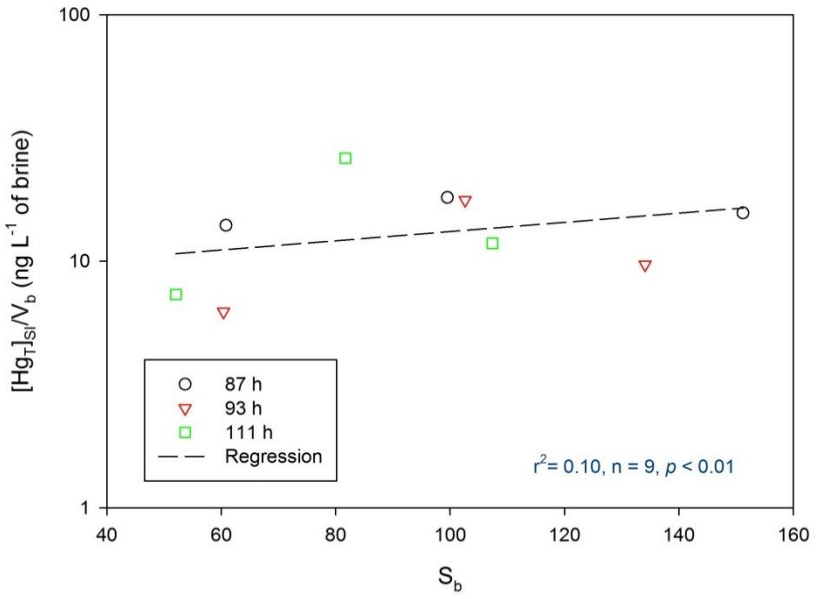

Figure 3.7: The relationship between Hg_T concentrations in experimental bulk sea ice ($[Hg_T]_{SI}$), normalized to brine volume fraction (V_b), and brine salinity (S_b).

A statistically significant linear log relationship exists between $[Hg_T]/V_b$ and S_b (r^2 = 0.10; p<0.01) in bulk experimental sea ice (Figure 3.7); however salinity only explains 10% of the variance in Hg_T concentrations in brine, even less than in the natural Arctic first-year sea ice where brine salinity explained ~39% of the variance in brine Hg_T

concentrations (Chaulk et al., 2011). Thus the process of freeze rejection alone is not sufficient to explain Hg_T concentrations within new and growing sea ice, and the presence of Hg-bound particles may have a stronger influence on these concentrations. Therefore it is assumed that the physical processes governing particle entrainment into sea ice are indirectly affecting the Hg concentrations within the ice. It is well known that sediment and suspended particulate matter becomes entrained into ice above shallow shelf regions, and can transported to various regions of the Arctic Ocean through ice motion (defined as "ice rafting" events) (Kempema et al., 1989; Nürnberg et al., 1994). However there is still considerable debate on the actual mechanism of particle entrainment within the sea ice matrix. Several possible mechanisms are listed in Appendices 3A.1, and further detailed studies on Hg_P incorporation into the sea ice matrix may indirectly address particle entrainment process.

Since Hg_P is the dominant form of Hg in sea ice, the vertical distribution of Hg_T concentrations through the ice column is expected to be governed by particle dynamics rather than brine dynamics, and the similarity between the Hg_P and Hg_T vertical distribution profiles (Figure 3.6A) support this hypothesis. The decrease in surface Hg_p concentrations over time (from 437 ng g^{-1} at 0 hr to 187 ng g^{-1} at 43 hr) and concurrent rise in some interior ice Hg_p concentrations (from 68 ng g^{-1} at 12 hr to 104 ng g^{-1} at 36 hr) in experiment 2.2 is a further example of how particle mobility within the ice dictates overall Hg_T concentrations.

The vertical mobility of particulate matter is likely enhanced by gravity drainage of brine during sea ice growth and desalination events during ice melt. This is partially demonstrated through the observed similarity in temporal trends of ESI and ESW Hg_T

concentrations, which may be caused by the release of Hg-bound particulate matter within brine expelled from the ice during formation and growth. A thin, dense brine layer (up to ~3 cm thick) builds up beneath the advancing ice-water interface to a certain extent before diffusing into the less saline water below (Petrich and Eicken, 2010). Cossa et al. (2011) hypothesized the release of Hg_T through a similar brine expulsion process during Antarctic first-year sea ice melt, suggesting this caused an increase in Hg_T concentrations in seawater directly underneath the ice. A Spearman's rank-order correlation was run to assess the relationship between ESW and ESI Hg_T concentrations (data from 87-11 hr excluded as trends diverge), and no statistically significant correlation was found, even over the first 15 hrs of ice growth where the trends between the two variables appeared to be very similar. This process of Hg-bound particulate expulsion from the ice may still be occurring, yet particulates may diffuse out of the enriched under-ice salt layer and sink, and thus would not be properly quantified. Testing this brine explusion hypothesis within a smaller, closed ice tank system where a complete mass balance of Hg_P concentrations could be established is required.

3.4.3 Hg enrichment in Frost Flowers: from seawater or from the air?

Based on Hg_T concentrations of nearly 300 samples of various ice crystal types collected in the Alaskan Arctic, Douglas et al. (2008) developed a conceptual model of mercury incorporation into snow and ice crystals. The idealized crystal structure includes: (A) a nucleus, which is hypothesized to be a sea salt aerosol or mineral particle; (B) a small crystalline mote surrounding the nucleus that underwent rapid growth; and (C) an outer crystal carapace that grew more slowly over time. Mercury is hypothesized to become incorporated into this crystal structure through 2 distinct processes: (1)

Particulates with bound Hg act as nucleation sources to initiate crystal formation, which locks Hg into the ice matrix at the nucleus of the crystal, and (2) Reactive gaseous mercury (RGM) is scavenged from the surrounding air and incorporated into the outer carapace region of the ice crystal through either absorption or adsorption processes (Douglas et al., 2008).

The concentrations of Hg_T in frost flowers grown at SERF were nearly an order of magnitude lower than natural frost flower concentrations reported near an ice lead during an AMDE in the Alaskan Arctic (45-180 ng L^{-1}) (Douglas et al., 2005; Douglas et al., 2008). During this Arctic study, frost flower Hg_T concentrations increased from 45 (2 hr old) to 180 ng L^{-1} (4-8 hr old) during flower growth as additional vapour condensed onto the crystal and water vapour to brine ratios increased (Douglas et al., 2008). This drastic increase in Hg_T concentrations during frost flower growth through vapour condensation was not seen in the experimental frost flower time series data. Therefore, the overall low Hg_T concentrations in experimental frost flowers grown at SERF and lack of any temporal trends seem to counter this model. However, upon closer inspection, these results actually strengthen its validity.

The incorporation of Hg, specifically Hg_P, into experimental ice crystals grown at SERF is assumed to be identical to the first process described by Douglas et al. (2008). Frost flowers form off of brine nodules over the surface of nilas ice, which contain particulate matter originating from the seawater and thus particles become assimilated into the frost flower crystals upon their initial formation. Therefore Hg species in frost flowers are expected to be mainly in Hg_P form. A large surface area was scraped to obtain

enough frost flower crystals for analysis, and therefore more Hg-bound particulate matter would have been taken up into the sample.

The lack of a temporal trend in frost flower Hg_T concentrations suggests that the second incorporation process described by Douglas et al. (2008), involving the scavenging of RGM from the surrounding atmosphere, is not occurring at SERF. Fundamental differences between the conditions at SERF and natural polar systems include oceanic and atmospheric Hg concentrations. Speciated atmospheric mercury measurements were taken at SERF (from ~1 m above ice surface) using a Tekran 1130/1135/2537A system, and atmospheric RGM concentrations ranged from <1-8.36 pg m^{-3}, which is lower than recorded averages for urban centres such as Detroit, MI, USA (17.7 ±28.9 pg m^{-3}) (Liu et al., 2007), and is very low compared to Arctic atmospheric levels during AMDEs. At Arctic sunrise in the spring when AMDEs begin, RGM has been measured to reach nearly 900 pg m^{-3} and exhibits a strong diurnal cycle (Lindberg et al., 2001). Douglas et al. (2008) assumed AMDEs were occurring when RGM concentrations were above background levels, or > 100 pg m^{-3}. Therefore, it is assumed that the photochemical reactions associated with AMDEs are not occurring at the SERF site and that the atmospheric RGM concentrations are too low to allow for scavenging of this species from the vapour phase during frost flower growth. Without this scavenging process, Hg_T concentrations would remain generally constant throughout frost flower development and decay, as only the initial process of Hg incorporation into frost flowers is occurring. Since the process of scavenging of atmospheric constituents during the kinetic growth phase of frost flowers is closely connected with their frost flower

concentrations, further measurement of volatile organic contaminants within frost flowers may provide information on the atmospheric levels of these contaminants, and vice versa.

3.4.4 Implications on Natural Sea Ice Dynamics

The accessibility of SERF provides the opportunity to conduct time-series experiments on newly formed and growing sea ice, and allows for a diverse range of variables to be measured, making it an extremely effective platform for process-based studies such as the one presented. It should be noted that fundamental differences exist between natural atmospheric and oceanic conditions; however, by investigating how these differences affect Hg_T concentrations in both SERF ESW and ESI, the processes affecting Hg_T concentrations within these media can be better understood. This is demonstrated well by the frost flowering event, where the absence of atmospheric RGM at SERF led to unnaturally low and consistent Hg_T concentrations in SERF frost flowers over time, and the process of Hg_T incorporation into frost flowers suggested by Douglas et al. (2008) was supported. A thorough comparison of Hg_T concentrations measured at SERF (in ESI and ESW) to those reported in the natural system is presented below.

As mentioned before, at SERF, ESW Hg_T concentrations (5.42 - 10.38 ng L^{-1}) were well over an order of magnitude higher than Arctic under-ice seawater concentrations (0.11 – 0.28 ng L^{-1}) (Chaulk et al., 2011), yet similar to Antarctic under-ice seawater concentrations, which widely range from 0.35 to 8.83 ng L^{-1} (Cossa et al., 2011). These unrealistically high ESW Hg_T concentrations at SERF stemmed from either the bulk salts used to prepare the ESW, which contained Hg_T concentrations up to 11 ng L^{-1} once dissolved and tested, or the well water used to fill the tank (~4 ng L^{-1}).

Although particulate concentrations were not measured in SERF, an estimate can be derived from the particulate weights measured on the filters during Exp.2.2, divided by the volume of water filtered through. Estimated particulate concentrations in SERF ESW range from 5.9-11.8 mg L^{-1}, while surface suspended particulate matter concentrations within the southern Beaufort Sea were found to be less than 0.5 mg L^{-1} in open water areas with bottom water depths above 50 m (Iseki et al., 1987). While particulate matter inArctic Ocean surface waters is mainly biogenic (Keith Bigg et al., 2004), the particulate matter in SERF is estimated to be mostly inorganic, and may include mineral salts that have precipitated out of the ESW solution, materials released from submerged monitoring equipment and deposited atmospheric particulates.

Initial Hg_T ESI concentrations, measured almost immediately after frazil ice consolidation in only 1.2 cm of thin nilas ice, were 1.87 ± 0.26 ng L^{-1}. This is similar to that measured in natural thin nilas ice (from 5 to > 50 mm thickness) from the Beaufort Sea, where reported concentrations ranged from 0.22-5.3 ng L^{-1} (Chaulk et al., 2011). Overall, Hg_T concentrations in nilas ice were quite variable, ranging from 0.20 to 9.20 ng L^{-1} (median: 2.12 ng L^{-1}), and are more reflective of concentrations in natural young ice (overall ice thickness > 10 cm) concentrations (~1.00 to 5.60 ng L^{-1}) rather than natural thin nilas ice (Chaulk et al., 2011; Cossa et al., 2011). Estimated ESI particulate concentrations range from ~10 to 105 mg L^{-1} (median: 25 mg L^{-1}), with the highest concentrations residing in the upper 2.5 cm of the ice. Particulate matter concentrations in Beaufort Sea first-year fast ice range from 3 to 1600 mg L^{-1} (Barnes et al., 1982), yet the sea ice sampled in Chaulk et al. (2011) is assumed to contain lower particulate concentrations due to its offshore location and increased depth of the ocean floor. The

ESW Hg_P concentrations reported in this study range from 13 to 233 ng g^{-1}, and are practical as they fall within the range reported for Hg_P in Arctic marine surface waters; 60 to 250 ng g^{-1} for the surficial waters of the Kara Sea north of Siberia (Coquery et al., 1995). In thick first-year ice cores collected from the Beaufort Sea, Hg_T concentrations for particulates collected from the bottom 10 cm of sea ice ranged from 4 to 22 ng g^{-1} (Burt et al., 2013b), which is lower than the values reported here (61 to 438 ng g^{-1} in nilas ESI), however differences in the methods used to measure the particulate Hg concentrations and the source of the particulate matter present (biogenic vs anthropogenic) may have led to the discrepancies. Even though Hg concentrations are higher in SERF relative to the natural system due to high particulate concentrations, this mesocosm-based investigation allowed for a thorough review of how the processes governing particulate dynamics within sea ice affect Hg concentrations. As the Arctic icescape shifts from a multiyear to a first-year sea regime where a larger overall volume of sea ice is melting every spring, this would provide an increasing seasonal source of Hg_P to the Arctic Ocean system over time. This Hg-bound particulate matter, speculated to be mainly organic in composition, may aggregate at pycnoclines within the water column, and the remineralization of this associated particulate matter would release Hg(II), allowing it to become bioavailable for methylation by microbial communities present (Stern et al., 2012b). Although the absolute values of Hg_T measured in the SERF system differ from those reported for natural polar systems, the insight into the biogeochemical processes controlling Hg uptake and dynamics within newly formed sea ice gained from this mesocosm-based study has furthered our understanding on how Hg cycling within the Arctic Ocean system will respond to a rapidly changing icescape.

3.5 References

Alvarez-Aviles L, Simpson WR, Douglas TA, Sturm M, Perovich D, Domine F. Frost flower chemical composition during growth and its implications for aerosol production and bromine activation. Journal of Geophysical Research: Atmospheres (1984–2012) 2008; 113.

Andreas EL, Guest PS, Persson POG, Fairall CW, Horst TW, Moritz RE, et al. Near-surface water vapor over polar sea ice is always near ice saturation. Journal of Geophysical Research: Oceans (1978–2012) 2002; 107.

Barnes PW, Reimnitz E, Fox D. Ice rafting of fine-grained sediment, a sorting and transport mechanism, Beaufort Sea, Alaska. Journal of Sedimentary Research 1982; 52: 493-502.

Brooks SB, Saiz-Lopez A, Skov H, Lindberg SE, Plane JM, Goodsite ME. The mass balance of mercury in the springtime arctic environment. Geophysical Research Letters 2006; 33: L13812.

Burt A, Wang F, Pućko M, Mundy CJ, Gosselin M, Philippe B, et al. Mercury uptake within an ice algal community during the spring bloom in first-year Arctic sea ice. Journal of Geophysical Research: Oceans 2013; 118: 4746-4754.

Chapter 2. Total and Methylated Mercury in Arctic Multiyear Sea Ice. In: Beattie S, editor. Mercury Dynamics in Natural and Experimental Sea Ice, 2014.

Chaulk A, Stern GA, Armstrong D, Barber DG, Wang F. Mercury distribution and transport across the ocean− sea-ice− atmosphere interface in the Arctic Ocean. Environmental Science & Technology 2011; 45: 1866-1872.

Comiso JC. Large decadal decline of the Arctic multiyear ice cover. Journal of Climate 2012; 25: 1176-1193.

Coquery M, Cossa D, Martin J. The distribution of dissolved and particulate mercury in three Siberian estuaries and adjacent Arctic coastal waters. Water, Air, and Soil Pollution 1995; 80: 653-664.

Cossa D, Heimbürger L-E, Lannuzel D, Rintoul SR, Butler EC, Bowie AR, et al. Mercury in the southern ocean. Geochimica et Cosmochimica Acta 2011; 75: 4037-4052.

Cox GF, Weeks WF. Equations for determining the gas and brine volumes in sea ice samples: US Army Corps of Engineers, Cold Regions Research & Engineering Laboratory, 1982.

Dietz R, Sonne C, Basu N, Braune B, O'Hara T, Letcher RJ, et al. What are the toxicological effects of mercury in Arctic biota? Science of the Total Environment 2013; 443: 775-790.

Douglas T, Sturm M, Simpson W, Brooks S, Lindberg S, Perovich D. Elevated mercury measured in snow and frost flowers near Arctic sea ice leads. Geophysical Research Letters 2005; 32: L04502.

Douglas TA, Sturm M, Simpson WR, Blum JD, Alvarez-Aviles L, Keeler GJ, et al. Influence of snow and ice crystal formation and accumulation on mercury deposition to the Arctic. Environmental Science & Technology 2008; 42: 1542-1551.

Environment Canada. Historical Climate Data, 2014. http://weather.gc.ca/canada.

Fitzgerald WF. Clean hands, dirty hands: Clair Patterson and the aquatic biogeochemistry of mercury. Clean Hands, Clair Patterson's Crusade Against Environmental Lead Contamination 1999: 119-137.
Fitzgerald WF, Lamborg CH, Hammerschmidt CR. Marine biogeochemical cycling of mercury. Chemical Reviews-Columbus 2007; 107: 641-662.
Geilfus NX, Galley R, Cooper M, Halden N, Hare A, Wang F, et al. Gypsum crystals observed in experimental and natural sea ice. Geophysical Research Letters 2013; 40: 6362-6367.
Hare A, Wang F, Barber D, Geilfus N-X, Galley R, Rysgaard S. pH evolution in sea ice grown at an outdoor experimental facility. Marine Chemistry 2013; 154: 46-54
Iseki K, MacDonald RW, Carmack E. Distribution of particulate matter in the south-eastern Beaufort Sea in late summer. Proc. NIPR Symposium on Polar Biology 1 1987, pp. 35-46.
Isleifson D, Galley RJ, Barber DG, Landy JC, Komarov AS, Shafai L. A study on the C-band polarimetric scattering and physical characteristics of frost flowers on experimental sea ice. IEEE Transactions on Geoscience and Remote Sensing 2014. 52: 3
Kaleschke L, Richter A, Burrows J, Afe O, Heygster G, Notholt J, et al. Frost flowers on sea ice as a source of sea salt and their influence on tropospheric halogen chemistry. Geophysical Research Letters 2004; 31.
Keith Bigg E, Leck C, Tranvik L. Particulates of the surface microlayer of open water in the central Arctic Ocean in summer. Marine chemistry 2004; 91: 131-141.
Kempema E, Reimnitz E, Barnes PW. Sea ice sediment entrainment and rafting in the Arctic. Journal of Sedimentary Research 1989; 59.
Lindberg S, Brooks S, Lin C, Scott K, Meyers T, Chambers L, et al. Formation of reactive gaseous mercury in the Arctic: evidence of oxidation of Hg to gas-phase Hg-II compounds after Arctic sunrise. Water, Air and Soil Pollution: Focus 2001; 1: 295-302.
Liu B, Keeler GJ, Dvonch JT, Barres JA, Lynam MM, Marsik FJ, et al. Temporal variability of mercury speciation in urban air. Atmospheric Environment 2007; 41: 1911-1923.
Liu G, Li Y, Cai Y. Adsorption of mercury on solids in the aquatic environment. In: G. Liu, Y. Cai, N. O'Driscoll, eds. Environmental Chemistry and Toxicology of Mercury, 1st Ed, John Wiley & Sons, Inc 2012, pp. 367-387.
Maslanik J, Fowler C, Stroeve J, Drobot S, Zwally J, Yi D, et al. A younger, thinner Arctic ice cover: Increased potential for rapid, extensive sea-ice loss. Geophysical Research Letters 2007; 34: L24501.
Maslanik J, Stroeve J, Fowler C, Emery W. Distribution and trends in Arctic sea ice age through spring 2011. Geophysical Research Letters 2011; 38.
Notz D, Wettlaufer JS, Worster MG. A non-destructive method for measuring the salinity and solid fraction of growing sea ice in situ. Journal of Glaciology 2005; 51: 159-166.
Nürnberg D, Wollenburg I, Dethleff D, Eicken H, Kassens H, Letzig T, et al. Sediments in Arctic sea ice: Implications for entrainment, transport and release. Marine Geology 1994; 119: 185-214.

Petrich C, Eicken H. Growth, structure and properties of sea ice. In: Thomas, DN, Dieckmann, GS, eds. Sea Ice. 2nd Ed. Wiley Blackwell, Chichester, UK 2010, 23-77.
Rankin A, Auld V, Wolff E. Frost flowers as a source of fractionated sea salt aerosol in the polar regions. Geophysical Research Letters 2000; 27: 3469-3472.
Rigét F, Braune B, Bignert A, Wilson S, Aars J, Born E, et al. Temporal trends of Hg in Arctic biota, an update. Science of the Total Environment 2011; 409: 3520-3526.
Schroeder W, Anlauf K, Barrie L, Lu J, Steffen A, Schneeberger D, et al. Arctic springtime depletion of mercury. Nature 1998; 394: 331-332.
Seigneur C, Lohman K. Effect of bromine chemistry on the atmospheric mercury cycle. Journal of Geophysical Research 2008; 113: D23309.
Stern GA, Macdonald RW, Outridge PM, Wilson S, Chételat J, Cole A, et al. How does climate change influence arctic mercury? Science of the Total Environment 2011; 414: 22-42.
USEPA. Method 1631: Mercury in Water by Oxidation, Purge & Trap, and Cold Vapour Atomuc Fluorescence Spectrometry. Office of Water 4303, 2002.
Wang F, Macdonald RW, Armstrong DA, Stern GA. Total and methylated mercury in the Beaufort Sea: the role of local and recent organic remineralization. Environmental Science & Technology 2012; 46: 11821-11828.
Wang F, Macdonald RW, Stern GA, Outridge PM. When noise becomes the signal: Chemical contamination of aquatic ecosystems under a changing climate. Marine Pollution Bulletin 2010; 60: 1633-1635.
Zar JH. Biostatistical analysis. 2nd. Ed. Prentice Hall. USA 1984.

Chapter 4: Conclusions and Future Directions

4.1 Conclusions

Mercury is one of the primary contaminants of concern in the Arctic marine ecosystem. Evidence is mounting that the cycling of mercury in the Arctic Ocean is increasingly influenced by changes in biogeochemical processes induced by climate change. As the Arctic Ocean icescape shifts from a multiyear (MY) to a first-year (FY) ice regime, the implications of this on Hg cycling within the Arctic Ocean system must be addressed. As discussed in Chapter 1, the overall objective of this thesis research was to investigate Hg dynamics within these sea ice matrices by addressing the following specific research questions:

1) What are the mechanisms behind Hg incorporation and vertical distribution within MY and FY ice?

3) What is the speciation of Hg within FY and MY ice?

To address these questions, both field and mesocosm-scale studies were carried out as described in Chapters 2 and 3, respectively. Chapter 2 represented the first comprehensive study on mercury dynamics in MY ice. Two Arctic MY ice cores were collected from the southeastern Beaufort Sea (August 16th, 2011) and McClure Strait (September 9th, 2013), and analyzed for Hg_T and $MeHg_T$, as well as ancillary variables. To strengthen the arguments, relevant data (Hg_T, temperature, and salinity) from a MYI core taken from the eastern Beaufort Sea (May 25th. 2008) and reported previously in Chaulk et al. (2011) were also presented. Concentrations of Hg_T for all three MYI sites ranged from 0.13-12.2 ng L^{-1}, with the highest levels occurring in the top 30 cm of the ice surface. Since the calculated brine volume approached 0 within the surface layers and no

relationship was found between brine salinity and Hg_T concentrations, these high surface Hg_T levels are thought to be due to accumulated particulate matter, which Hg has a high affinity for. Particulate matter was not quantified in this study; however, based on the mean particulate matter concentration in Arctic MY ice, the surface enrichment in Hg can be readily explained if the Hg_T content of sea ice particulate matter is ~ 40 ng g^{-1}, which is in good agreement with Arctic Ocean floor surface sediment Hg_p concentrations reported for the Arctic Ocean (~36-116 ng g^{-1}) (Gobeil et al., 1999). Though not as high as in the surface ice layer, elevated Hg_T concentrations were also found within the bottom MY ice layers, and demonstrated a strong, positive correlation with Chl *a* concentrations within the ice, suggesting that Hg is associated with biogenic matter near the ocean-ice interface. The particulate-driven distribution of Hg in MY ice can also explain the regional differences in Hg in MY ice between the Beaufort Sea and McClure Strait.

Concentrations of $MeHg_T$ in MYI ice ranged from below the MDL (<0.02 ng L^{-1}) to 0.53 ng L^{-1}, and to our knowledge are the first reported concentrations of $MeHg_T$ in Arctic sea ice. The MY ice core from McClure strait showed considerably higher concentrations than Beaufort Sea MY ice (up to 30 times higher), however since Hg_T concentrations were also higher in this ice, the ratio of $MeHg_T/Hg_T$ varied within a similar range (0-40%). Since $MeHg_T$ concentrations are depleted in Arctic Ocean surface seawater, and the percolation of snow meltwater containing $MeHg_T$ does not account for the higher $MeHg_T$ levels at the ocean-ice interface, it leaves *in situ* methylation as the only plausible source for the observed $MeHg_T$ in sea ice. If confirmed, this hypothesis would have major implications on Hg cycling within the Arctic Ocean system. Thus, further measurements of $MeHg_T$ concentrations and taxonomic identification of the

bacterial assemblages present within both MY and FY ice are required. With this expanded dataset, the fluxes of Hg_T and $MeHg_T$ into the Arctic Ocean upon MY ice melt were calculated to be 420 and 42 kg yr^{-1} respectively, revealing an important seasonal source of Hg into the Arctic Ocean marine ecosystem.

Since surface enrichment in Hg_T concentrations within sea ice is a ubiquitous phenomenon and Hg_T concentrations correlate with autotrophic biomass within the bottom of MY ice, previous work has hypothesized that the processes involved in the incorporation of Hg_T into the sea ice matrix include Hg-bound particulate uptake, and particulate dynamics control the vertical distribution of Hg_T (Chapter 2, 2014; Chaulk et al., 2011). To further examine the role of particulate matter in Hg dynamics within sea ice, several time-series experiments on newly-formed and growing experimental sea ice were carried out at the Sea-ice environmental Research Facility (SERF) at the University of Manitoba during the winter months of 2012 and 2013, which are presented in Chapter 3. Throughout the study, the concentrations of Hg_T, Hg_D and Hg_P, were measured in a variety of experimental sea ice (ESI) types, including frost flowers as well as in the underlying experimental seawater (ESW). Overall, the highest Hg_T concentrations were found in bulk frost flowers (median = 10.8 ng L^{-1}), while the lowest were found in nilas ESI (2.3 ng L^{-1}) and the bottom 5 cm of young ESI (2012: 2.1 ng L^{-1}; 2013: 2.4 ng L^{-1}). Concentrations of Hg_P in bulk ESI ranged from 61 to 438 ng g^{-1}, and represented ~73% of Hg_T concentrations, thus Hg_P is the dominant Hg species in sea ice. Since the highest Hg_P concentrations were measured in new nilas ice, particulate matter is thought to become entrained within the ice upon initial sea ice formation, as hypothesized. To investigate whether freeze rejection has a greater influence on Hg_T concentrations in sea

ice over particle entrainment, the relationship between brine volume, salinity and Hg_T concentrations was explored in young ice, as performed by Chaulk et al (2011). A weak relationship existed between Hg_T concentrations in bulk sea ice (normalized to brine volume fraction) and brine salinity, thus freeze rejection does not influence Hg_T concentrations in new sea ice as much as particle entrainment processes. Alongside the similarity in vertical distributions of Hg_P and Hg_T concentrations within the ice column, temporal monitoring of Hg_p concentrations revealed a decrease in surface levels over time and a concurrent increase in some interior ice Hg_p concentrations, suggesting that particulate dynamics play a more dominant role than brine dynamics in the transport and vertical distribution of Hg within the FY ice column. A unique frost flowering event occurred at SERF during February 2012, which allowed for the temporal monitoring of Hg_T within frost flowers as well as the underlying ESI and ESW matrices. Interestingly, frost flower Hg_T concentrations were over a magnitude lower than reported in the Arctic (Douglas et al., 2005; Douglas et al., 2008), and showed little change over time even as their water vapour to brine ratio increased. Speciated atmospheric Hg measurements conducted at SERF showed little RGM was present at the SERF site, and thus the Hg within SERF frost flowers is thought to originate solely from the formation of ice crystals around Hg-bound particles as the scavenging of atmospheric RGM with kinetic crystal growth did not occur. This finding confirms the idealized model of Hg incorporation in ice crystals by Douglas et al. (2008), and suggests that chemical concentrations in frost flowers may be representative of volatile atmospheric contaminants.

As concentrations of Hg within Arctic biota and human populations continue to rise while global anthropogenic emissions stabilize, the scientific community has called

for further investigation into within-system processes that may be releasing $MeHg_T$ into the Arctic marine ecosystem (Kirk et al., 2012; Sonke et al., 2013; Stern et al., 2012b). In response, this work presents the first measurements of $MeHg_T$ within Arctic sea ice, and identifies melting MY ice as a potential seasonal source of $MeHg_T$ into the Arctic Ocean system. By adding to the current dataset on Hg concentrations in MY ice, flux estimates for the release of Hg_T and $MeHg_T$ into the Arctic Ocean upon MY ice melt were calculated, and can now strengthen current models and mass balance budgets of Hg in the Arctic marine system (Fisher et al., 2012; Outridge et al., 2008). The investigation of Hg dynamics within new and growing ESI at SERF was the first mechanistic study of its kind, and deepened our understanding of the processes controlling Hg incorporation into sea ice as well as transport and vertical distribution of Hg through the ice column. Through this review of the small-scale processes controlling sea ice chemistry, the physical and chemical mechanisms governing sea ice formation and growth can be further speculated on.

4.2 Research Limitations

4.2.1 Sampling Limitations

An inherent limitation with the MY sea ice work presented in chapter 2 is the lack of a large sample size. Due to the extreme challenges in logistical preparation and field circumstances out of the researchers' control, only two separate MY ice floes were able to be sampled, and only 1 sampling event per scientific cruise was able to be completed. Inclusion of the MY ice core collected by Chaulk et al. (2011) strengthens this dataset to a certain extent, yet there is still a dire need for more MY sea ice Hg analysis, particularly to improve the flux estimates presented. The presence of $MeHg_T$ within MYI suggests that *in situ* methylation of Hg is occurring, yet no conclusive statement could be drawn from this small sampling size, for which more MY samples are needed. Since there was a significant difference in Hg_T and $MeHg_T$ concentrations from the southeastern Beaufort Sea and McClure Strait, the spatial and temporal (seasonal) coverage of these datasets need to be improved on to better explain this variability.

An important sea ice parameter that was not analyzed in this study is microstructure. Sea ice brine volume can be estimated from the temperature and salinity profiles and can allude to meltwater percolation, yet microstructure analysis can provide insight on the spacing of brine inclusions, channels, and growth conditions when the ice formed (Petrich and Eicken, 2010). The age and history of the MY ice can then be better estimated, and potential rafting events or seawater influxes can be more positively identified (Chaulk et al., 2011; Pfirman et al., 1990). The collection of microstructure data, or at least high-resolution photographs of the cores sampled, is suggested for future work on MY ice and FY ice.

4.2.2 Analysis Limitations

Thanks to the pioneering work of Chaulk et al. (2011), the processing of sea ice cores for Hg_T analysis was effective, and low Hg_T concentrations were measured in ice. To further improve upon the processing methods, a ceramic or plastic (metal-free) vice could be installed to the cold room counter to make the handling and scraping of ice sections more manageable.

Unlike the Hg_T analysis, the standard protocols for $MeHg_T$ analysis are less defined and numerous regional and international laboratories employ their own modifications to improve the sensitivity of the analysis. The $MeHg_T$ analysis employed for MY1 ice samples followed in UCTEL is EPA Method 1630; Methyl mercury in water by distillation, aqueous ethylation, purge and trap, and CVAFS (1998). This method was effectively used on seawater samples from the Beaufort Sea, and the data was recently published (Wang et al., 2012). A recent modification on this method was suggested by Flett Research Ltd (Winnipeg, Canada), whereby samples are spiked with 250 µL of a 20% (wt/v) KCl / 0.2% L-cysteine solution. This solution acts as a matrix modifier, ensuring that volatile methylated Hg species are not lost during the distillation process by strongly binding to them. This modification was added to the $MeHg_T$ analysis method used in UCTEL; however the analysis was not as effective on sea ice as it had been on seawater, which may be due to the lower salinities of sea ice samples.

Since there are no certified reference standards for $MeHg_T$ in seawater, each sample was spiked with 10 µL of a 1 ng mL^{-1} n-propylmercuric chloride (ERA) solution and recoveries ranged from 61 – 127%. This recovery range is considerably larger than that reported by Wang et al. in 2012 (88-112%). This was most probably due to the

ethylation procedure or the distillation procedure. Numerous issues with the distillation process have been revealed in literature, including the importance of timing the distillation procedure to ensure consistent distillate volumes for each batch of samples analyzed and the decomposition of $MeHg_T$ compounds near the end of the distillation process (Horvat et al., 1993). An updated method (Bowman and Hammerschmidt, 2011) that removed the distillation procedure and replaced it with a 12-hr acidification step, followed by a pH neutralization, was employed to analyze for $MeHg_T$ in the MY2 ice sample from McClure Strait (2013). The recoveries improved slightly, to 65-121%, with this method, but can be improved by increasing the sample size up to 500 mL (from 50 mL) (Bowman and Hammerschmidt, 2011).

By taking advantage of the distinct isotopic composition of snowmelt and seawater, $\delta^{18}O$ was measured in an attempt to date the MY ice. However the $\delta^{18}O$ profile did not reveal any peaks within the ice interior, which would represent annual snowmelt and allow for an ice age approximation. Care must be taken when interpreting sea ice age from isotopic composition, as a study conducted by Eicken *et al.* (2002) that attempted to trace the percolation of meteoric meltwater throughout sea ice using stable isotope measurements concluded that MY ice is too superimposed to use these measurements as proper tracers (Eicken et al., 2002). This study specifically points out that the identification of meteoric meltwater (strongly negative $\delta^{18}O$ values) is particularly unsuccessful in the late melt stage, as the meltwater signal has dissipated within the ice column over time. The transient tracer ^{7}Be, which is a radioactive nuclide ($t_{1/2}$ = 53.3 d) that is deposited through precipitation, was suggested as an alternative to stable isotope tracers for MYI as its activity is concentrated in the upper snow layers and weakens down

through the snow – sea-ice – seawater continuum. Tracing meltwater with ^{7}Be is important when investigating Hg distribution within the ice column, as meltwater percolation and pooling has been concluded to strongly influence particulate dynamics and thus associated Hg_p within sea ice.

4.3 Future Direction

4.3.1 Particulate Measurements Required

It has been concluded that the dominant form of Hg within sea ice is particulate-bound Hg (Hg_p). Future work on Hg within sea ice should analyze the concentrations of particulate matter within the surface ice layer, as well as Hg_p concentrations, to further investigate the possibility of particulate matter concentrations acting as a proxy for Hg_T concentrations in sea ice. The spatial variability demonstrated in MY ice Hg concentrations is thought to be a function of the location where the ice floes formed and initial particle/sediment entrainment occurred. This could be verified by characterizing the chemical composition of the particulate matter present, which when matched with bottom sediments can positively identify the ice formation location. Particulate elemental composition can be qualitatively assessed using a scanning electron microscope coupled to an X-ray diffraction probe (Poulain et al., 2007). This technique cannot assess the organic content of the particles, yet it can be inferred if a low signal strength of elemental signatures is found (Leck and Bigg, 2005). An alternative to organic particulate identification would be to test the solubility of isolated particulate matter in organic vapours by observing if the particles spread once exposed to organic vapours such as decane and cyclohexane, as employed in the characterization of biogenic material from the Arctic Ocean surface microlayer (Leck and Bigg, 2005).

4.3.2 SERF Studies

As mentioned, the spatial and temporal monitoring of Hg_T and $MeHg_T$ concentrations in all Arctic ice types is warranted, yet will be an extremely tedious and costly task. As highlighted in Chapter 3, SERF provides a unique opportunity to monitor

sea ice biogeochemistry over time in an effective and controlled manner. There are a multitude of benefits to conducting mechanistic and biogeochemical sea ice studies such as the one presented at SERF. The close proximity of the SERF mesocosm to the clean lab at the University of Manitoba was extremely beneficial, and allowed for rigorous temporal sampling campaign to be undertaken. Field sampling was well controlled and thus contamination was minimized, and triplicate samples for each media were able to be taken (i.e 3 ice cores, 3 water samples), allowing for true standard deviations to be reported. Unique ice types formed under various atmospheric conditions at SERF, allowing for opportunistic sampling of pancake ice and frost flowers. The ability to conduct effective, high calibre experiments at SERF attracts local, national and international scientists from a variety of disciplines, creating an engaging and multidisciplinary environment at the research facility. Numerous studies investigating the biogeochemical and physical characteristics of sea ice have been conducted at SERF and successfully published (Geilfus et al., 2013; Hare et al., 2013a; Isleifson et al., 2014), thus SERF provides the unique opportunity to conduct controlled experiments on new and growing sea ice.

The ability to control and measure all parts of the aquatic system in SERF allows for small microcosm experiments investigating the actual speciation reactions that occur within sea ice and seawater media to be conducted. Since the seven stable mercury isotopes in the environment tend to fractionate when subjected to various physical processes, isotopic mercury fractionation is a powerful tool used to elucidate the biogeochemical transformation occurring within the environment (Bergquist and Blum, 2009). Mass-dependent fractionation occurs through biotic and abiotic reactions, thus

would be useful in elucidating the mechanisms involved in incorporating Hg-bound particulates into sea ice, while mass-independent fractionation occurs through UV self-shielding, and could identify photochemical reactions occurring in the seawater surface (Bergquist and Blum, 2009). Recently the chemical reactions controlling Hg speciation in Arctic snowpacks were investigated using mass-independent fractionation analyses, and photochemical reactions were found to release a significant portion of Hg back into the atmosphere (Sherman et al., 2010).

Since the experimental nature of SERF excludes the influence of natural biota on Hg dynamics within sea ice, it would be very interesting to measure $MeHg_T$ within SERF ESI to see if *in situ* methylation is occurring. The investigation of *in situ* methylation within sea ice could be taken further if $MeHg_T$ is detected (above detection limit), and a thorough investigation on the bacterial assemblages present and their Hg methylation potential could be explored. Again the experimental setting may add a great deal of insight into the methylation potential in sea ice, as it did for the incorporation of Hg into frost flowers in the absence of RGM.

4.3.3 Diffusive Gradient Thin Films

The demand for continuous contaminant monitoring systems in waterways has led to the development of unique, *in situ* monitoring tools for $MeHg_T$, such as Diffusive Gradient Thin Films (DGTs). Once deployed in the water, labile dissolved $MeHg_T$ diffuses through a gel and accumulates on an ion-exchange resin. After a certain deployment time, $MeHg_T$ is extracted and eluted off of the DGTs in the lab, and can then be ethylated and analyzed through whichever instrumentation is present (Dommergue et al., 2009). In the past these samplers have been deployed in freshwater systems in the

south, and recently they were used to determine $MeHg_T$ mobility during the melt of the Arctic snowpack (Clarisse et al., 2009; Clarisse and Hintelmann, 2006; Dommergue et al., 2009). These samplers require contact with water at all times, so can not be frozen into ice to monitor $MeHg_T$ transport within sea ice, yet could be installed beneath the growing ice surface in SERF to catch the brine expulsion phenomenon. Extensive laboratory and field calibration experiments (performed at SERF) would need to be completed to determine if the gels could withstand the cold temperatures and saline nature of the Arctic Ocean system.

4.3.4 Mer-lux Biosensor

A recently defined form of environmentally-relevant Hg is BioHg, which represents all Hg species that are able to cross biological membranes (Larose et al., 2011; Scott, 2001). Several molecular tools, including whole cell and protein-based Hg biosensors, have been developed. A recent study performed by Larose *et al.* (2011) that investigated BioHg cycling within the Arctic snowpack employed the mer-lux biosensor, which is a highly specific and sensitive genetically-engineered bacteria reporter for Hg (Omura et al., 2004). Optimal condition and control experiments revealed that this luminescent biosensor responded in a linear manner to Hg^{2+} in the 0.5-50 ng L^{-1} range, which covers Hg levels determined in the Arctic snowpack (in the absence of AMDEs) and sea ice. This biosensor could be used in tandem with $MeHg_T$ analysis to determine to concentrations of bioavailable inorganic and organic Hg species within the sea ice environment. Larose *et al.* (2011) simulated the potential inorganic speciation of Hg in snow using a commercial chemical equilibrium program (Visual MINTEG v2.61), which estimated from the input parameters that Hg speciation is largely driven by high chloride

and bromide concentrations, and thus a large portion of $HgCl_2$ complexes may exist in the snow. Previous laboratory studies using the mer-lux bioreporter found these inorganic complexes to be bioavailable, thus researchers hypothesized to detect a high fraction of BioHg within snow. Yet this was not the case, and large fractions of Hg_p within snow, which is not bioavailable, were suggested to be the cause of this discrepancy between the modelled speciation and the field experiments (Larose et al., 2011). Therefore by employing the mer-lux biosensor on sea ice samples, the lack of BioHg detected can roughly indirectly indicate the fraction of Hg_p present.

4.4 References

Bergquist BA, Blum JD. The odds and evens of mercury isotopes: applications of mass-dependent and mass-independent isotope fractionation. Elements 2009; 5: 353-357.

Bowman KL, Hammerschmidt CR. Extraction of monomethylmercury from seawater for low-femtomolar determination. Limnol. Oceanogr. Methods 2011; 9: 121-128.

Chapter 2. Total and Methylated Mercury in Arctic Multiyear Sea Ice. In: Beattie S, editor. Mercury Dynamics in Natural and Experimental Sea Ice, 2014.

Chaulk A, Stern GA, Armstrong D, Barber DG, Wang F. Mercury distribution and transport across the ocean− sea-ice− atmosphere interface in the Arctic Ocean. Environmental Science & Technology 2011; 45: 1866-1872.

Clarisse O, Foucher D, Hintelmann H. Methylmercury speciation in the dissolved phase of a stratified lake using the diffusive gradient in thin film technique. Environmental Pollution 2009; 157: 987-993.

Clarisse O, Hintelmann H. Measurements of dissolved methylmercury in natural waters using diffusive gradients in thin film (DGT). Journal of Environmental Monitoring 2006; 8: 1242-1247.

Dommergue Al, Larose C, Faïn X, Clarisse O, Foucher D, Hintelmann H, et al. Deposition of mercury species in the Ny-Ålesund area (79 N) and their transfer during snowmelt. Environmental Science & Technology 2009; 44: 901-907.

Douglas T, Sturm M, Simpson W, Brooks S, Lindberg S, Perovich D. Elevated mercury measured in snow and frost flowers near Arctic sea ice leads. Geophysical Research Letters 2005; 32.

Douglas TA, Sturm M, Simpson WR, Blum JD, Alvarez-Aviles L, Keeler GJ, et al. Influence of snow and ice crystal formation and accumulation on mercury deposition to the Arctic. Environmental Science & Technology 2008; 42: 1542-1551.

Eicken H, Krouse H, Kadko D, Perovich D. Tracer studies of pathways and rates of meltwater transport through Arctic summer sea ice. Journal of Geophysical Research 2002; 107: 8046.

Fisher JA, Jacob DJ, Soerensen AL, Amos HM, Steffen A, Sunderland EM. Riverine source of Arctic Ocean mercury inferred from atmospheric observations. Nature Geoscience 2012; 5: 499-504.

Geilfus NX, Galley R, Cooper M, Halden N, Hare A, Wang F, et al. Gypsum crystals observed in experimental and natural sea ice. Geophysical Research Letters 2013; 40: 6362-6367.

Gobeil C, Macdonald RW, Smith JN. Mercury profiles in sediments of the Arctic Ocean basins. Environmental Science & Technology 1999; 33: 4194-4198

Hare A, Wang F, Barber D, Geilfus N-X, Galley R, Rysgaard S. pH evolution in sea ice grown at an outdoor experimental facility. Marine Chemistry 2013; 154: 46-54.

Horvat M, Liang L, Bloom NS. Comparison of distillation with other current isolation methods for the determination of methyl mercury compounds in low level environmental samples: Part II. Water. Analytica Chimica Acta 1993; 282: 153-168.

Isleifson D, Galley RJ, Barber DG, Landy JC, Komarov AS, Shafai L. A study on the C-band polarimetric scattering and physical characteristics of frost flowers on experimental sea ice. IEEE Transactions on Geoscience and Remote Sensing 2014; 52(3): 1787-1798.

Kirk JL, Lehnherr I, Andersson M, Braune BM, Chan L, Dastoor AP, et al. Mercury in Arctic marine ecosystems: Sources, pathways and exposure. Environmental Research 2012; 119: 64-87.

Larose C, Dommergue Al, Marusczak N, Coves J, Ferrari CP, Schneider D. Bioavailable mercury cycling in polar snowpacks. Environmental Science & Technology 2011; 45: 2150-2156.

Leck C, Bigg EK. Biogenic particles in the surface microlayer and overlaying atmosphere in the central Arctic Ocean during summer. Tellus B 2005; 57: 305-316.

Omura T, Kiyono M, Pan-Hou H. Development of a specific and sensitive bacteria sensor for detection of mercury at picomolar levels in environment. Journal of Health Science 2004; 50: 379-383.

Outridge P, Macdonald R, Wang F, Stern G, Dastoor A. A mass balance inventory of mercury in the Arctic Ocean. Environmental Chemistry 2008; 5: 89-111.

Petrich C, Eicken H. Growth, structure and properties of sea ice. In: Thomas, DN, Dieckmann GS, eds. Sea Ice. 2nd Ed. Wiley Blackwell, Chichester, UK, 2010, pp. 23-77.

Pfirman S, Lange M, Wollenburg I, Schlosser P. Sea ice characteristics and the role of sediment inclusions in deep-sea deposition: Arctic—Antarctic comparisons. Geological history of the polar oceans: Arctic versus Antarctic. Springer, 1990, pp. 187-211.

Poulain AJ, Garcia E, Amyot M, Campbell PG, Ariya PA. Mercury distribution, partitioning and speciation in coastal vs. inland High Arctic snow. Geochimica et Cosmochimica Acta 2007; 71: 3419-3431.

Scott KJ. Bioavailable mercury in arctic snow determined by a light-emitting mer-lux bioreporter. Arctic 2001; 54: 92-95.

Sherman LS, Blum JD, Johnson KP, Keeler GJ, Barres JA, Douglas TA. Mass-independent fractionation of mercury isotopes in Arctic snow driven by sunlight. Nature Geoscience 2010; 3: 173-177.

Sonke JE, Heimbürger L-E, Dommergue A. Mercury biogeochemistry: Paradigm shifts, outstanding issues and research needs. Comptes Rendus Geoscience 2013; 345: 213-224.

Stern GA, Macdonald RW, Outridge PM, Wilson S, Chételat J, Cole A, et al. How does climate change influence arctic mercury? Science of the Total Environment 2012; 414: 22-42.

Wang F, Macdonald RW, Armstrong DA, Stern GA. Total and methylated mercury in the Beaufort Sea: the role of local and recent organic remineralization. Environmental Science & Technology 2012; 46: 11821-11828.

Appendix 1: Mercury Analyses Employed

In order to investigate the speciation of Hg in sea ice, several different Hg analyses were employed throughout this work. The concentrations of Hg_T and $MeHg_T$ were measured in natural Arctic multiyear sea ice (Chapter 2), while Hg_T, Hg_D and Hg_P were measured in experimental sea ice and seawater (Chapter 3). Each of the analyses followed standard protocols, which are briefly described below.

A1.1 Total and Dissolved Mercury Analysis

This analysis follows EPA method 1631, Revision E: Mercury in Water by Oxidation, Purge & Trap and Cold Vapour Atomic Fluorescence Spectrometry, and was performed on a 2600 Tekran® Series 2600 instrument system (USEPA, 2002). Shortly after collection, samples to be analyzed for Hg_D were filtered through 0.45 µm sterilized filter prior to preservation. All seawater and melted sea ice samples were then preserved with 12N ultrapure hydrochloric acid (HCl) within 4 hours after their collection/melt and stored in a 4°C fridge for a maximum of 36 h. Prior to analysis, bromine chloride (BrCl) was added to all samples as a further preservation agent and to oxidize all Hg species present to Hg(II). After oxidation, hydroxylamine hydrochloride (HH; $NH_2OH{\cdot}HCl$) was added to samples to destroy free halogens and neutralize the low pH. On the automated Tekran system, stannous chloride ($SnCl_2$) was added to samples to reduce all Hg(II) to Hg^0 and reduced samples were then passed through a vapour/liquid phase separator to remove Hg^0 from the aqueous solution. Gaseous Hg^0 was amalgamated onto a primary gold trap, thermally desorbed and carried via an inert gas stream (argon) to a second analytical gold trap, where it undergoes an additional collection and thermal desorption cycle. The carrier gas then transports the Hg^0 to the sample cell of the atomic fluorescent

spectrophotometer, where Hg atoms are excited. Upon their relaxation, these Hg atoms emit photons at a characteristic wavelength, which were detected and quantified.

A1.2 Methylmercury Analysis

This analysis follows EPA Method 1630: Methylmercury in Water by Distillation, Aqueous Ethylation, Purge & Trap and Cold Vapour Atomic Fluorescence Spectrometry (USEPA, 2001), and employed MERX automated $MeHg_T$ analyzer. Prior to analysis, 50 mL sample aliquots were transferred into dedicated fluoropolymer distillation vessels. The slightly saline melted sea ice samples were preserved with 2 mL L^{-1} of 9 M H_2SO_4 solution to avoid distillation interferences resulting from excess chloride. Samples were also spiked with 2 mL L^{-1} of KCl/L-cysteine solution, which acts as a matrix modifier. Approximately 40 mL of each sample was distilled for 2 hours at 125°C under UHP N_2 flow into receiving vessels using the automated Brooks Rand distillation system. After distillation, the sample was frozen overnight in a dedicated chest freezer (-21°C) and thawed out ~12 hrs later. Once thawed, distillates were transferred into amber glass vials. The low pH of the samples was adjusted to ~4.9 by the addition of an acetate buffer and an n-propyl recovery standard is added. Finally, all the organic Hg species in the samples were ethylated by the addition of sodium tetraethyl borate ($NaBEt_4$) to methylethyl mercury ($CH_3CH_3CH_2Hg$). Samples were placed onto the MERX automated $MeHg_T$ analyzer, where methylethyl Hg is separated from the sample through purging with UHP N_2 onto a graphitic carbon trap (Carbotrap®). This trapped organic Hg is thermally desorbed from the Carbotrap® into an Ar gas stream that carries it initially through a pyrolytic decomposition column that converts all organic Hg species to elemental Hg vapour (Hg^0) and then into the sample cell of the CVAFS for detection.

A1.3 Particulate-Bound Mercury Analysis

This analysis follows EPA Method 7473: Mercury in Solids and Solutions by Thermal Decomposition, Amalgamation and Atomic Absorption Spectrophotometry (USEPA, 2007). Melted experimental sea ice and experimental seawater samples were filtered through pre-weighed hydrophilic polypropylene membrane filters (47 mm, 0.2 μm) to collect the particulate matter. These filters were then air-dried for ~48 hrs within a laminar flow cabinet in an ultra-clean trace elements laboratory (UCTEL). Filters were re-weighed to ensure complete dryness and obtain a mass of particulate matter. Each filter was rolled up using clean techniques, placed into a tared quartz sample boat and weighed. These sample boats were placed into the Hydra II C Direct Mercury Analyzer (Teledyne Leeman Labs). Within the analyzer, the sample is first dried then thermally decomposed at ~300°C within the controlled decomposition furnace. The decomposition products are then carried by UHP O_2 flow to the catalytic furnace, where at ~600°C all Hg species present are oxidized to Hg^0 vapour, while all halogens and nitrogen/sulfur oxides are trapped. All residual decomposition products are then flushed to the gold-plated amalgamator, which selectively traps the Hg^0 vapour. The amalgamator is then heated, releasing the collected Hg^0 vapour, which flows within the O_2 into the sample cell of a single wavelength atomic absorption spectrophotometer. The total Hg concentration in the sample was then derived from the measurement of the absorbance peak at 253.7 nm. Note that this concentration represents the amount of Hg within the filter as well, therefore blank filter subtraction must be incorporated into the calculation of Hg_P.

A1.4 References

USEPA. Method 1630: Methylmercury in Water by Distillation, Aqueous Ethylation, Purge and Trap, and Cold Vapour Atomic Fluorescence Spectrometry. Engineering and Analysis Division (4303), Washington, DC, 2001.

USEPA. Method 1631, Revision E: Mercury in Water by Oxidation, Purge & Trap and Cold Vapour Atomic Fluorescence Spectrometry. Office of Water 4303, 2002.

USEPA. Method 7473: Mercury in Solids and Solutions by Thermal Decomposition, Amalgamation and Atomic Absorption Spectrophotometry, 2007.

Appendix 2: Chapter 2

A2.1 Study Area

The marginal Beaufort Sea, located west of the Canadian Arctic Archipelago, is comprised of water masses originating from the Pacific (0-200 m) and Atlantic (below 200 m) oceans and seasonally influenced by freshwater input from the Mackenzie River (Carmack and Macdonald, 2002b). Local sea ice types include offshore pack ice, consisting of mobile first-year and multiyear floes, and landfast ice formed within the coastal margins over the continental shelves (Barber and Hanesiak, 2004a). Due to a winter surface high-pressure system over the Beaufort Sea, its pack ice rotates in the anticyclonic gyre and eventually gets exported into the transpolar drift and through the Fram Strait (Barber and Hanesiak, 2004a; Kwok et al., 2009). The incorporation of pack ice into the gyre leads to large annual variability in areal ice coverage and deformed or rotten ice regimes (Barber et al., 2009; Barber and Hanesiak, 2004a). Located above Banks Island, McClure Strait connects the Beaufort Sea to Viscount Melville Sound and receives mainly pacific water masses from the Beaufort Sea once they have circulated through the gyre (Nguyen and Maranger, 2011). From 1981-2010, the median ice concentration, expressed as percentage aerial coverage, off the western coast of Banks Island in the Beaufort Sea (where sampling sites MY1 and MY2 are located) is 7-10/10 in August, and in the McClure Strait (MY3) is 4-6/10 in September (Canadian Ice Service; http://ec.gc.ca/glaces-ice). The Beaufort Sea receives an influx of nutrients and sediments from both an oceanic (Arctic Ocean) and riverine source (Mackenzie River), and is particularly productive along the Canadian shelf region (southeastern Beaufort Sea) (Carmack and Macdonald, 2002a). Due to river inflow and ice growth, oceanographic conditions in the Beaufort Sea demonstrate extreme annual and interannual variations.

A2.2 Estimate of Hg_T and $MeHg_T$ in sea ice brine

The concentrations of Hg_T and $MeHg_T$ in brine was estimated from the following equation:

$$C_b = C_{si}/V_b$$

where C_b and C_{si} are the concentrations of Hg_T or $MeHg_T$ in brine and bulk sea ice, respectively, and V_b is the brine volume fraction.

The calculation of V_b followed the general approach described in:(Petrich and Eicken, 2010)

$$V_b = (1 - V_a)\frac{(\rho_i(T)/1000)S_{si}}{F_1(T) - (\rho_i(T)/1000)S_{si}F_2(T)} \qquad (1)$$

where V_a is the air volume fraction, S_{si} is the bulk ice salinity, $\rho_i(T)$ is the density (kg m^{-3}) of pure ice at temperature T (^oC):

$$\rho_i(T) = 917 - 0.1403T \qquad (2)$$

$F_1(T)$ and $F_2(T)$ are empirical polynomial functions of temperature:

$$F_i(T) = a_i + b_iT + c_iT^2 + d_iT^3 \qquad (3)$$

When $0 \geq T > -2\ ^oC$, the coefficients a_i, b_i, c_i, and d_i used are from (Leppäranta and Manninen, 1988). When $-2 \geq T \geq -22.9\ ^oC$, those from (Cox and Weeks, 1983) are used.

As V_a can be substantial in multi-year ice (Timco and Frederking, 1996), it cannot be neglected in Eq (1) when calculating V_b. V_a is calculated from the following (Cox and Weeks, 1983):

$$V_a = 1 - \frac{\rho_{si}}{\rho_i} + \rho_{si}S_{si}\frac{F_2(T)}{F_1(T)} \qquad (3)$$

where ρ_{si} (kg m^{-3}) is the bulk ice density. Since ρ_{si} was not measured in this study, we estimated it from an empirical equation derived from 14 multi-year Arctic ice cores taken in the summer (Eicken et al., 1995):

$$\rho_{si} = 0.03568 \ln(z) + 0.88177 \quad (2)$$

where z (m) is the depth.

The brine salinity, S_b, is estimated using the following equation (Petrich and Eicken, 2010):

$$S_b = \left(1 - \frac{54.11}{T}\right)^{-1} \times 1000 \quad (4)$$

A2.3 Relationship between brine Hg_T and $MeHg_T$ concentrations and brine salinity

In Arctic FY sea ice, brine concentration of Hg_T has been shown to correlate with brine salinity (Chaulk et al., 2011) suggesting that freeze rejection of seawater Hg in brine is an important process of enriching Hg in sea ice brine. To test whether this applies to MY ice, we plotted the MY ice brine concentration of Hg_T and $MeHg_T$, estimated as $[Hg_T]/V_b$ and $[MeHg_T]/V_b$, respectively, as a function of brine salinity S_b. As shown in Figure S1, there was no statistically significant correlation ($p > 0.05$) between them, suggesting freeze rejection is not an important process of concentrating seawater Hg_T or $MeHg_T$ into MY ice brine.

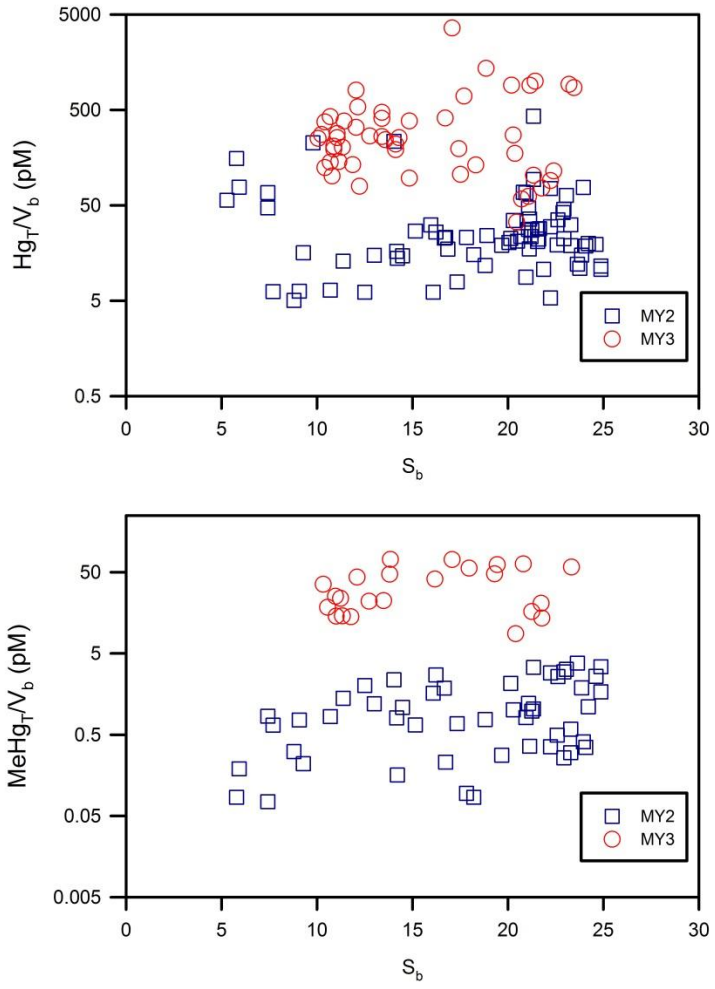

Figure A2.1: Brine Hg_T and $MeHg_T$ concentrations vs. brine salinity in MY ice

Figure A2.2: Photo of multiyear sea ice sampling event at MY2 (southeastern Beaufort Sea) on August 16th, 2013, Note the abundance of melt ponds.

A2.4 References

Barber DG, Galley R, Asplin MG, De Abreu R, Warner KA, Pucko M, et al. Perennial pack ice in the southern Beaufort Sea was not as it appeared in the summer of 2009. Geophysical Research Letters 2009; 36: L24501.

Barber DG, Hanesiak JM. Meteorological forcing of sea ice concentrations in the southern Beaufort Sea over the period 1979 to 2000. Journal of Geophysical Research 2004; 109: C06014.

Carmack EC, Macdonald RW. Oceanography of the Canadian Shelf of the Beaufort Sea: A setting for marine life. Arctic 2002; 55: 29-45.

Chaulk A, Stern GA, Armstrong D, Barber DG, Wang F. Mercury distribution and transport across the ocean− sea-ice− atmosphere interface in the Arctic Ocean. Environmental Science & Technology 2011; 45: 1866-1872.

Cox GFN, Weeks WF. Equations for determining the gas and brine volumes in sea-ice samples. Journal of Glaciology 1983; 29: 306-316.

Eicken H, Lensu M, Leppäranta M, Tucker WB, Gow AJ, Salmela O. Thickness, structure, and properties of level summer multiyear ice in the Eurasian sector of the Arctic Ocean. Journal of Geophysical Research 1995; 100(C11): 22697-22710.

Kwok R, Cunningham G, Wensnahan M, Rigor I, Zwally H, Yi D. Thinning and volume loss of the Arctic Ocean sea ice cover: 2003–2008. Journal of Geophysical Research: Oceans (1978–2012) 2009; 114.

Leppäranta M, Manninen T. The brine and gas content of sea ice with attention to low salinities and high temperatures. 1988.
Nguyen AT, Menemenlis D, Kwok R. Arctic ice-ocean simulation with optimized model parameters: Approach and assessment. Journal of Geophysical Research: Oceans (1978–2012) 2011; 116.
Petrich C, Eicken H. Growth, structure and properties of sea ice. In: Thomas DN, Dieckmann GS, editors. Sea Ice. 2nd Ed. Wiley-Blackwell, Chichester, UK, 2010, pp. 23-77.
Timco GW, Frederking RMW. A review of sea ice density. Cold Regions Science & Technology 1996; 24: 1-6.

Appendix 3: Chapter 3

Figure A3.1: Photo of the SERF site at the University of Manitoba, taken in January 2013. The experimental sea ice was approximately 7 cm thick at this time.

Table A3.1: Concentrations and percentages of major ions within reference experimental seawater and all four SERF experiments conducted.

		[Major Ions] in mg/L, (% of Total [Ions])			
	Experiment	*Standard Seawater*[a]	SERF 1.1	SERF 1.2	SERF 2.1, 2.2
	Dates of Experiment	*N/A*	Dec. 23, 2011 - Jan. 20, 2012	Feb. 10 – 21, 2012	2.1: Jan.13 - 25, 2013 2.2: Feb.18 - 20, 2013
Cations	Ca^{2+}	392 (1.18%)	349 (1.02%)	278 (1.12%)	460 (1.42%)
	K^{+}	366 (1.11%)	382 (1.12%)	356 (1.43%)	636 (1.96%)
	Mg^{2+}	1226 (3.70%)	1170 (3.42%)	442 (1.77%)	383 (1.18%)
	Na^{+}	10188 (30.77%)	10600 (31.01%)	7969 (32.03%)	10800 (33.24%)
Anions	Cl^{-}	18315 (*55.31%)*	19200 (56.17%)	14500 (58.28%)	18200 (56.01%)
	SO_4^{2-}	2566 (*7.75%)*	2480 (7.26%)	1320 (5.31%)	1940 (5.97%)
	Br^{-}	62 (*0.19%)*	N/A	16.4 (0.07%)	73.8 (0.23%)
	Conductivity (mS/cm)	53.00	49.50	42.70	50.20
	Salinity	35.00	32.30	28.00	32.90
	pH	7.5-8.4	8.45	8.37	7.94
	Alkalinity (mM)	2.2	2.06$\pm$ 0.19	1.80 $\pm$ 0.20	2.51 $\pm$ 0.01

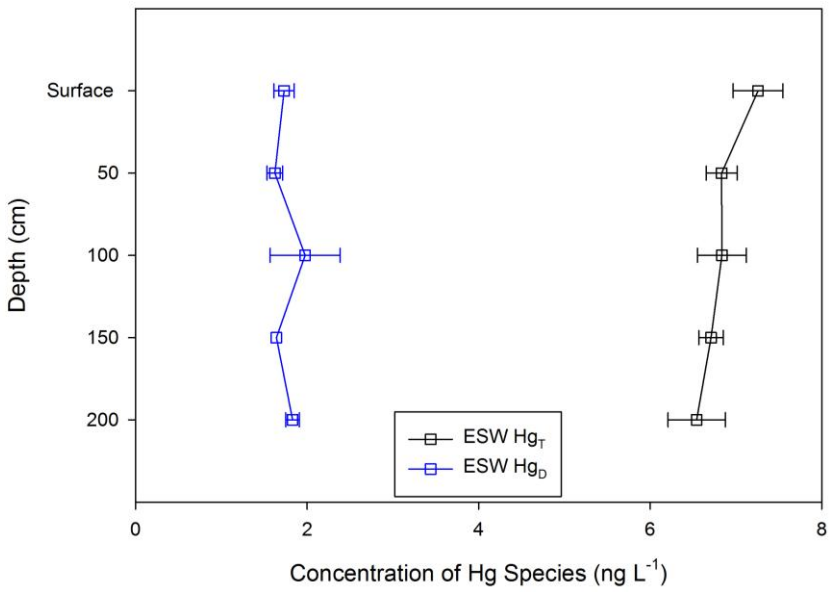

Figure A3.2: Profiles of Hg_T and Hg_D concentrations in SERF ESW taken during experiment 2.1 at 12 hr (January 14th, 2013).

3A.1 Possible mechanisms of particle entrainment within newly formed sea ice

Possible mechanisms of particle entrainment within newly forming sea ice include: 1) Individual particles acting as nucleation points or "seeding nuclei" for solid frazil ice crystals to form around in supercooled waters (heterogeneous nucleation); 2) The scavenging of particles from seawater onto the ice crystal lattice during frazil ice growth; and 3) The "harvesting" of particles into the frazil ice layer through the ascent of this layer in the water column (Gosink and Osterkamp, 1983; Kempema et al., 1993; Reimnitz et al., 1993b; Smedsrud, 2001; Weeks and Ackley, 1986). These crystals eventually rise to the ocean surface and consolidate, forming frazil ice (Thomas et al., 2010).

3A.2 References

Gosink TA, Pearson JG, Kelley JJ. Gas movement through sea ice. Nature 1976; 263: 41-42.

Kempema E, Reimnitz E, Clayton Jr J, Payne J. Interactions of frazil and anchor ice with sedimentary particles in a flume. Cold Regions Science and Technology 1993; 21: 137-149.

Reimnitz E, Clayton J, Kempema E, Payne J, Weber W. Interaction of rising frazil with suspended particles: tank experiments with applications to nature. Cold Regions Science and Technology 1993b; 21: 117-135.

Smedsrud LH. Frazil-ice entrainment of sediment: large-tank laboratory experiments. Journal of Glaciology 2001; 47: 461-471.

Thomas DN, Papadimitriou S, Michel C. Biogeochemistry of sea ice. Sea ice, 2010, pp. 425-467.

Weeks WF, Ackley SF. The growth, structure and properties of sea ice. The geophysics of sea ice. 146, 1986, pp. 9-164.